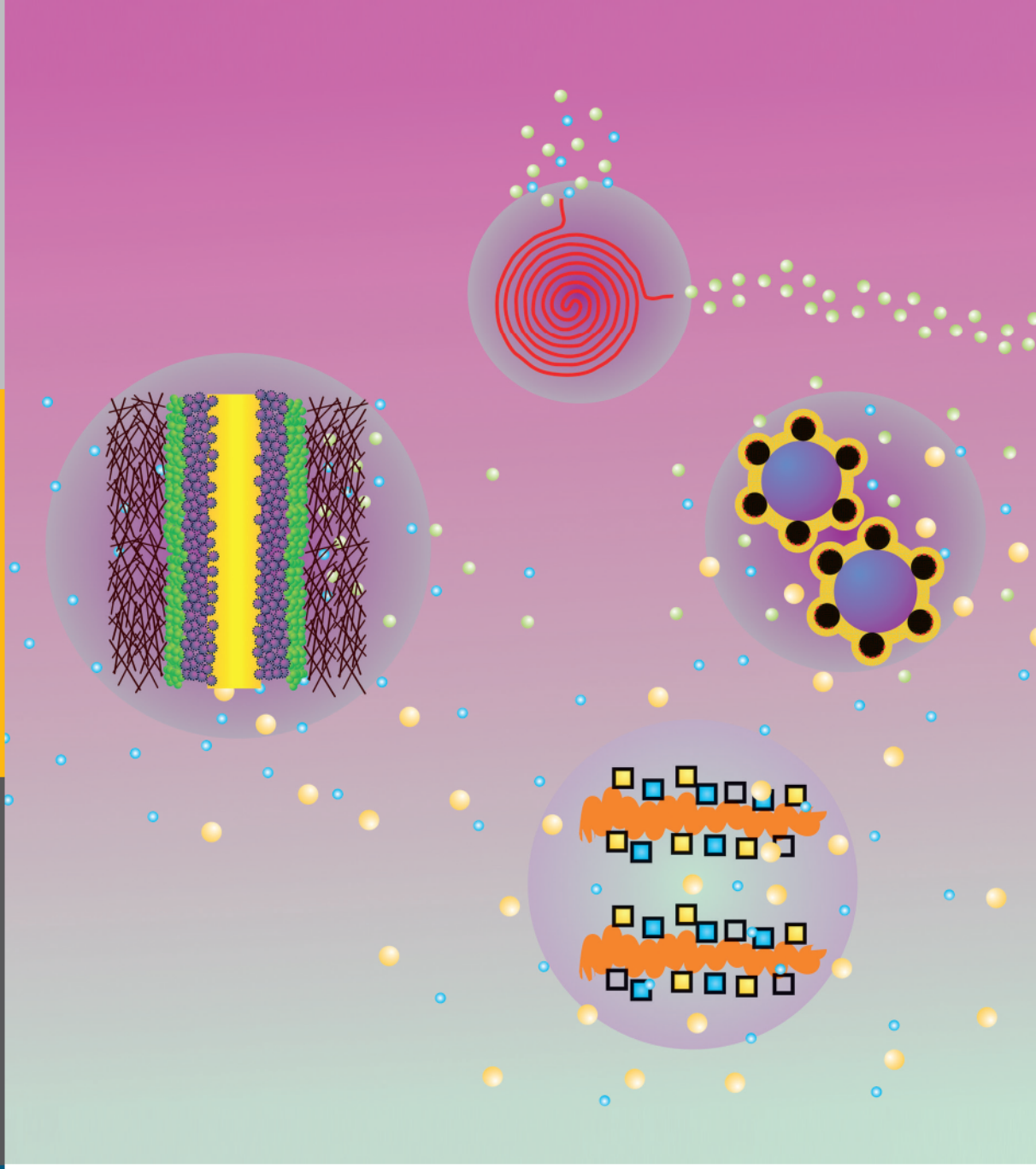

Interaction of Phosphoric Acid with Cell Components in High Temperature Polymer Electrolyte Fuel Cells

Fang Liu

JÜLICH
FORSCHUNGSZENTRUM

Member of the Helmholtz Association

Schriften des Forschungszentrums Jülich
Reihe Energie & Umwelt / Energy & Environment Band / Volume 219

Forschungszentrum Jülich GmbH
Institute of Energy and Climate Research
Electrochemical Process Engineering (IEK-3)

Interaction of Phosphoric Acid with Cell Components in High Temperature Polymer Electrolyte Fuel Cells

Fang Liu

Schriften des Forschungszentrums Jülich
Reihe Energie & Umwelt / Energy & Environment Band / Volume 219

ISSN 1866-1793 ISBN 978-3-89336-972-0

Bibliographic information published by the Deutsche Nationalbibliothek.
The Deutsche Nationalbibliothek lists this publication in the Deutsche Nationalbibliografie; detailed bibliographic data are available in the Internet at http://dnb.d-nb.de.

Publisher and Distributor: Forschungszentrum Jülich GmbH
Zentralbibliothek
52425 Jülich
Tel: +49 2461 61-5368
Fax: +49 2461 61-6103
Email: zb-publikation@fz-juelich.de
www.fz-juelich.de/zb

Cover Design: Grafische Medien, Forschungszentrum Jülich GmbH

Printer: Grafische Medien, Forschungszentrum Jülich GmbH

Schriften des Forschungszentrums Jülich
Reihe Energie & Umwelt / Energy & Environment, Band / Volume 219

D 82 (Diss., RWTH Aachen University, 2014)

ISSN 1866-1793
ISBN 978-3-89336-972-0

Interaction of Phosphoric Acid with Cell Components in High Temperature Polymer Electrolyte Fuel Cells

by Fang LIU

Abstract

A high-temperature polymer electrolyte fuel cell (HT-PEFC) is an efficient and clean energy converting device. The protonic conductivity of the electrodes and the polybenzimidazole-type membrane is assured by phosphoric acid. The electrochemical reactions in HT-PEFCs of hydrogen and oxygen to water take place in the electrodes of the membrane electrode assembly (MEA) which are partly soaked with phosphoric acid. The performance of a HT-PEFC depends mainly on the interactions between all cell components as well as on the amount, the concentration and distribution of phosphoric acid inside these components. Whereas, the concentration and distribution is a function of current density and water vapour distribution in the MEA.

The reaction between phosphoric acid and poly[2,5-benzimidazole] (ABPBI) membrane was investigated with the focus on kinetics and thermodynamics. The maximum acid doping levels were estimated experimentally at different doping times, doping temperatures and concentrations of the phosphoric acid bath. Afterwards, the reaction mechanisms were examined. The studies involved the amount and type of the coordinating sites of the polymer, the activation energy, the rate-limiting step, the equilibrium constant and the dissociation constant.

In the MEA, the phosphoric acid is uneven distributed in the ABPBI membrane and the catalyst layers of gas diffusion electrode (GDE). This distribution changes with total acid uptake and the GDE structure. When the cells are operated under constant current, equilibrium between water production and water removal in the electrodes is established. The water removal is associated with the transport properties of the MEA components and the flow field geometry of the cell. As a result, the phosphoric acid concentration is influenced in the catalyst layer. In addition, the oxygen distribution in the catalyst layer is sensitive to the structure of GDEs, the flow properties of the flow field, the concentration and distribution of phosphoric acid in the catalyst layer.

A series of experiments revealed that the optimum cell performance was achieved at high phosphoric acid doping level, thick cathode catalyst layer with the high Pt loading and a medium anode thickness with about half the Pt loading compared to the cathode. It was further demonstrated that a spiral flow field which allows gas cross over between adjacent flow channels resulted in better cell performances and lifetime compared to a conventional serpentine flow field.

Interaktion der Phosphorsäure mit der Membran-Elektroden-Einheit in Hochtemperatur-Polymerelektrolyt-Brennstoffzellen

von Fang LIU

Kurzfassung

Eine Hochtemperatur-Polymerelektrolyt-Brennstoffzelle (HT-PEFC) ist ein effizienter und umweltfreundlicher Energiewandler. Die Phosphorsäure gewährleistet die Protonenleitfähigkeit der Elektroden und der Membran. Die elektrochemischen Reaktionen in HT-PEFC von Wasserstoff und Sauerstoff zu Wasser erfolgen in den Elektroden der Membran-Elektroden-Einheit (membrane-electrodeassembly, MEA), die teilweise mit Phosphorsäure getränkt ist. Die Leistung der HT-PEFC hängt hauptsächlich von der Menge, der Konzentration und Verteilung von Phosphorsäure in der Membran und der MEA ab. Die Konzentration und Verteilung der Phosphorsäure ist dabei eine Funktion der Stromdichte und der Wasserverteilung in der MEA.

Mit dem Fokus auf Kinetik und Thermodynamik wurde die Reaktion zwischen der Phosphorsäure und der Poly-[2,5]-benzimidazol (ABPBI) Membran untersucht. Die maximalen Säuredotierungen wurden experimentell bei verschiedenen Dotierungszeiten, Dotierungstemperaturen und Konzentrationen des Phosphorsäurebads ermittelt. Anschließend wurden die Reaktionsmechanismen untersucht. Die Studien ergaben die Menge und Art der Koordinationsstellen des Polymers, die Aktivierungsenergie, den geschwindigkeitsbestimmenden Reaktionsschritt, sowie die Gleichgewichtskonstantenund die Dissoziationskonstanten.

In der MEA ist die Phosphorsäure in der Membran und der Katalysatorschichten der Gasdiffusionselektroden (GDE) ungleichmäßig verteilt. Diese Verteilung ändert sich mit der gesamten Säureaufnahme und der GDE-Struktur. Werden die Zellen unter einem konstanten Strom betrieben, ergibt sich ein Gleichgewicht zwischen Wasserproduktion und Wasserentfernung in den Elektroden. Die Wasserentfernungist stark abhängig von den Transporteigenschaften der MEA-Komponenten und der Strömungsfeldgeometrie der Zelle. Als Ergebnis wird die Phosphorsäurekonzentration in der Katalysatorschicht beeinflusst. Darüber hinaus ist die Sauerstoffverteilung in der Katalysatorschicht empfindlich gegenüber der Struktur der GDE, den Eigenschaften des Strömungsfeldes, der Konzentration und Verteilung der Phosphorsäure in der Katalysatorschicht. Aus den Untersuchungsergebnissen geht hervor, dassfolgende Parameter zu einer verbesserten Leistung führen: höheres Phosphorsäure-Dotierungs-niveau, dickere Kathoden-Katalysatorschicht mit erhöhter Platinbeladung der Anode. Weiterhin scheint die Kombination von mittlerer Anode-Dicke mit halber Platin-Beladung im Vergleich zur Kathode ein Optimum darzustellen. Es wurde ferner gezeigt, dass einschneckenförmiges Strömungsfeld, das eine Überquerung des Reaktionsgases zwischen benachbarten Strömungskanälen ermöglicht, eine bessere Zellleistung und besseren Lebensdauer im Vergleich zu einem herkömmlichen serpentinenförmigen Strömungsfeld zur Folge hat.

Contents

1 Introduction and Goal of Work

HT-PEFC[1]s are receiving increasing attention as electrochemical energy converters. Hydrogen is consumed and electricity and heat are converted during the electrochemical process.

Hydrogen is oxidized into protons at the anode of a HT-PEFC and protons are transferred from the anode to the cathode through the membrane. Phosphoric acid doped ABPBI[2] is one of the most widely used proton-conductive polymer membrane in HT-PEFCs. The proton reacts with oxygen at the cathode and generates water as product. The anode and cathode are composed of a catalyst layer and a GDL[3]. The catalyst layer is the place where the electrochemical reactions take place. The anode, cathode and membrane are assembled to a MEA[4], which is the heart of the HT-PEFC. The proton conductivity of the membrane and the catalyst layers at the anode and cathode rely on phosphoric acid. The HT-PEFC consists of solid (electrodes and ABPBI membrane), liquid (phosphoric acid solution) and gas (hydrogen, oxygen and water vapor) phases. The performance of the HT-PEFC depends on these phases and their interactions. The present study focuses on the effects of the acid and gas distribution in the MEA on the performance of HT-PEFC.

1.1 Acid in ABPBI membrane

The proton conductivity of ABPBI depends on the content and composition of phosphoric acid, which is associated with the reaction between acid and membrane. Since the kinetic of ABPBI doping in the phosphoric acid solution is still unknown, it is interesting to investigate the reaction, the reaction rate and the rate-determining step of the doping process. In addition to room temperature measurements, the dynamic study will be carried out at higher temperatures to estimate the activation energy. Moreover, the isotherm of doping ABPBI membrane is also performed at different temperatures to examine the amount and type of the coordinating sites, the equilibrium and dissociated constant. Based on these estimations, the mechanism of acid introduction into the MEA can be determined The acid content in the membrane will also be estimated during the cell operation.

[1] high-temperature polymer electrolyte fuel cell
[2] poly[2,5-benzimidazole]
[3] gas diffusion layer
[4] membrane electrode assembly

1.2 Acid distribution in catalyst layer

In the electrodes the electrochemical reactions take place at the three phase boundary, phosphoric acid being the proton conducting phase. The distribution of phosphoric acid in the catalyst layer varies with the total acid uptake of the MEA and the structure of GDE[5]s. In addition, the proton conductivity of phosphoric acid is sensitive to the acid concentration. This concentration is modified by the water retention in the MEA. The determination of the acid distribution and concentration will be examined within different MEAs, in which the acid uptake, the catalyst loading and the thickness of the catalyst layer are modified.

1.3 Gas distribution in catalyst layer

The electrochemical reaction depends on the supply of the reactants and the removal of the products. The transport of gaseous reactants (oxygen) and products (water) is influenced by the presence of the GDL, the MPL[6] and the geometry of the flow field. In addition, the gaseous reactants have to be transport through the acid film which covers the surface of the active site in the catalyst layer. The oxygen diffusion through this film is controlled by the distribution and concentration of the phosphoric acid in the catalyst layer. The acid concentration varies with the water vapor partial pressure over the acid solution. The effects of the gas distribution on the performance of the HT-PEFC will be evaluated with a customized flow field design.

1.4 Outline

- Chapter 2 presents the actual status of the research found in the literature.
- Chapter 3 gives the detail information of the experimental work.
- Chapter 4 and Chapter 5 present the experiments on the reactions between phosphoric acid and the ABPBI membrane.
- Chapter 6, Chapter 7 and Chapter 8 describe the study on the effect of the electrode structure and the component content of MEA on the performance of HT-PEFCs.
- Chapter 9 discusses the influence of different flow field designs on performance
- Chapter 10 gives a comprehensive discussion of all results
- Chapter 11 is the conclusion

[5] gas diffusion electrode
[6] micro-porous layer

2 Theory and Literature Overview

HT-PEFC is an energy converter, in which the chemical energy of fuel is converted into electricity directly [1, p.7].

2.1 General overview

The basic reactions in HT-PEFC can be described as HOR[1] at the anode (Eqn. 2.1) and ORR[2] at the cathode (Eqn. 2.2) [2; 3]. HT-PEFCs are typically operated in a temperature range from 120 °C to 200 °C [4, p.3-8; 5;6;7]. The water production is mainly in the gaseous phase.

$$H_2 \rightleftharpoons 2\,H^+ + 2\,e^- \tag{2.1}$$

$$\tfrac{1}{2}\,O_2 + 2\,H^+ + 2\,e^- \rightleftharpoons H_2O \tag{2.2}$$

The heart of a HT-PEFC is the MEA, which contains the following basic components, as illustrated in Fig. 2.1a:

- Proton conductive membrane. It transfers protons from the anode to the cathode [5].
- Catalyst layer. It is the place where the electrochemical reactions take place. The catalyst layer is a mixed conductor of protons and electrons [7].
- Gas diffusion layer (with or without a microporous layer). The layer provides a pathway for the gaseous reactants and products arriving at and departing from the catalyst layer [8, p.1]. It also serves at heat and electronic conducting layer, and mechanically supports the catalyst layer [1, p.93; 8, p.1].

The combination of a catalyst layer and a gas diffusion layer forms a GDE. Two GDEs together with the membrane form the MEA.

In addition to a MEA, each single cell contains a pair of graphite flow field plates and stainless steel endplates. The flow field plates provide electronic and thermal conductivity and have to be temperature stable up to 200 °C [3]. The flow field plates are machined with a series of channels

[1] hydrogen oxidation reaction
[2] oxygen reduction reaction

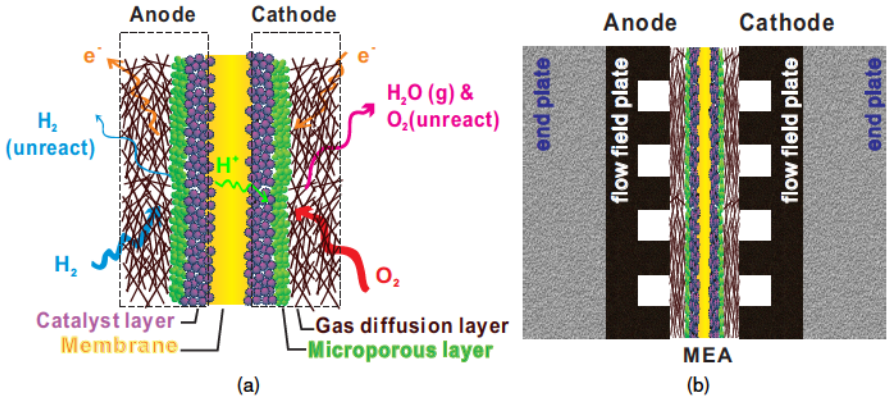

Figure 2.1: Schematic representation of (a) a MEA and (b) a HT-PEFC (single cell).

to provide the pathways for gas flow from inlet to outlet [9]. The endplates are necessary for the compression of the cells and stacks. The overall structure of the HT-PEFC is illustrated as Fig. 2.1b.

2.2 Membrane with phosphoric acid

The membrane of HT-PEFCs is usually PBI[3] [10; 11] or ABPBI [12–14]. The chemical structures of the repeating units are shown in Fig. 2.2 for both polymers.

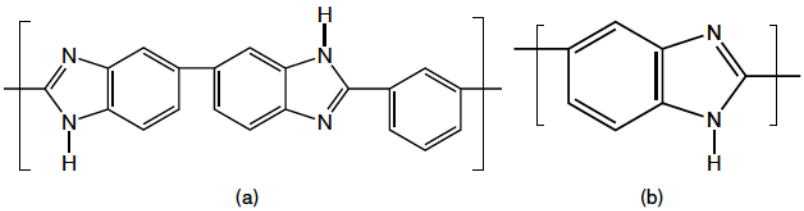

Figure 2.2: Structure of repeat unit of (a) PBI and (b) ABPBI.

The proton conductivity of the HT-PEFC is provided by phosphoric acid in the membrane and in the GDE [15–17]. The performance of the HT-PEFC is sensitive to the amount of phosphoric acid in these components [10; 18], while independent of the way to introduce the acid into the MEA [19]. Depending on the properties of the membrane, several different ways can be chosen to introduce phosphoric acid into MEA:

- doping the membrane in an acid bath [10; 12; 20];
- immersing the catalyst-coated membrane in an acid bath [21];

[3] poly[2,2'-(m-phenylene)-2,5'-bibenzimidazole]

- dropping the acid solution onto the GDE [11; 22];
- combination of two or several techniques as mentioned above [21].

Therefore, the first step is to understand the reactions between membrane and phosphoric acid.

2.2.1 Kinetic study

To the best of knowledge, there is only one publication on the kinetic study of doping PBI membranes in a bath of phosphoric acid [23]. It was found that the uptake of H_3PO_4 and H_2O at room temperature increased significantly at the beginning of the doping process, and then slowly approaching equilibrium. The kinetic of the doping process was found to follow the first-order reaction rate law. The rate constant decreases as the concentration of the acid bath is raised, since the increased viscosity of acid solution slows down the kinetic doping process [24]. However, the authors [23] did not continue to study the reaction mechanism, for example the activation energy [25, pp.807-809], the reaction steps [25, pp. 809-810] or the rate-limiting step [26].

If the doping process is considered as a process of phosphoric acid adsorbed by the PBI chains [27], the rate-limiting step can be distinguished by the intraparticle diffusion model [28]. The method is widely used to analyze the adsorption process [26; 29–32]. The theoretical treatments of the intraparticle diffusion involve the complicated mathematical calculations [28; 33] based on the diffusion equations [34, p.11]. The differential solutions of the diffusion equations give the adsorbate uptake as a function of the squared root of the adsorption time [28], the so-called intraparticle plot. Over the whole investigation period, the plot presents three common forms [35]:

i : the intraparticle plot can be identified as three portions [31; 36]. The initial portion describes the adsorbate transported from the bulk of solution through the boundary layer. The external adsorption occurs in this step, which can also be defined as the boundary layer diffusion. The middle portion refers to the adsorbate transports within the free space in the adsorbent. It is a gradual adsorption stage in which the intraparticle diffusion dominates. The final stage is the equilibrium adsorption which is limited thermodynamically.

ii : the intraparticle plot is a straight line, which passes through the origin [26; 37]. It indicates the process controlled by the boundary layer diffusion.

iii : the plot contains a positive intercept instead of passing through the origin [29; 30; 32; 35]. The positive intercept reveals that a rapid external adsorption occurs within a short period of time.

2.2.2 Thermodynamic study

In addition to the kinetic study, the chemical equilibrium of the doping process was investigated. At room temperature, it was found that the equilibrium uptakes of H_2O and H_3PO_4 in the PBI

membrane increase as the concentration of the acid bath is raised [38; 39]. The acid concentration in the doped PBI is higher than that of the acid solution as long as the concentration of the acid bath which is used for doping is below 14.8 molL^{-1} [23; 38]. The concentrating effect is associated with the acid-base interaction between H_3PO_4 and PBI chains [38]. This concentrating effect helps to maintain the acid in the membrane during the long time operation of a HT-PEFC.

Diaz *et al.* [39] investigated the H_2O adsorption of the PBI and ABPBI membranes with multilayer BET isotherms. They found that the water uptake of PBI fits to the type-II isotherm [40]. The process is a strong physical adsorption with high adsorption energy. In contrast, the adsorption of water by ABPBI chains follows the type-III isotherm [40]. It is a weaker physical adsorption with lower adsorption energy.

The isotherm of H_3PO_4 uptake adsorbed onto the PBI chains at room temperature was studied by the Scatchard method [27], which is a variant of the Langmuir isotherm [40; 25, p.917-918]. The Scatchard method [41; 42] has been widely used in the field of biochemistry [43] and aquatic chemistry [44] to investigate the association of small ligands with macromolecules. Below a brief description of the Scatchard method applied to the process of doping PBI by phosphoric acid [27] is given.

The doping of PBI with phosphoric acid from an aqueous solution occurs through the coordinating sites of the polymer. The membrane contains a large number of coordinating sites per molecule. Considering the interaction between polymer molecules and coordinating sites as well as the polymer macrostructure, the authors [27] supposed that the formed complexes are very different for different reactive sites, although they might be chemically homogeneous. It is assumed that there are *i* types of coordinating sites for H_3PO_4 per PBI repeat unit. $[L_i]_T$ is the total concentration of the *i*th site, which is the molar ratio of *i*th site to the repeat unit. If the volume of acid solution is much larger than what could be absorbed in the membrane, the concentration of the acid solution, C_0, can be considered as constant during the doping process. If the water uptake has no influence on the formed complexes of PBI-H_3PO_4, the concentration of the free coordinating site is:

$$[L_i]_F = [L_i]_T \quad [L_i]_B \tag{2.3}$$

$[L_i]_F$	mol mol^{-1}	concentration of free *i*th site
$[L_i]_T$	mol mol^{-1}	total concentration of *i*th site
$[L_i]_B$	mol mol^{-1}	concentration of occupied *i*th site

If supposing a 1 : 1 stoichiometric coordination of H_3PO_4 to active sites, the thermodynamic equilibrium constant is given by Eqn. 2.4. The value of K_i describes the affinity of coordination [25, pp.202-203].

$$K_i = \frac{[L_i]_B}{C_0 \times [L_i]_F} \tag{2.4}$$

Therefore, the probability of occupation of the *i*th type coordinating site, $\bar{\theta}_i$, can be expressed as:

$$\bar{\theta}_i = \frac{[L_i]_B}{[L_i]_T} = \frac{[L_i]_B}{[L_i]_F + [L_i]_B} = \frac{K_i \times C_0}{1 + K_i \times C_0} \tag{2.5}$$

If $\bar{\theta}_i$ is considered as the coverage of H_3PO_4 at the solid surface of PBI, the equation corresponds to a Langmuir isotherm [40; 25, p.917-918]. The total degree of occupation is calculated as:

$$\bar{\theta}_T = \frac{[L]_B}{[L]_T} = \frac{\sum_{i=1}^{i} [L_i]_B}{\sum_{i=1}^{i} [L_i]_T} \tag{2.6}$$

In practice, the total concentration of occupied coordinating sites, $[L]_B$, is the acid doping level defined as the molar ratio of the doped H_3PO_4 to the PBI repeat unit. And the total concentration of coordinating site, $[L]_T$, is the maximum H_3PO_4 uptake.

If there is only one type of the coordinating sites in ABPBI, $i = 1$,

$$\bar{\theta}_T = \frac{[L]_B}{[L]_T} = \frac{K \times C_0}{1 + K \times C_0} \tag{2.7}$$

After rearranging,

$$\frac{[L]_B}{C_0} = K \times [L]_T \quad K \times [L]_B \tag{2.8}$$

The plot of $\frac{[L]_B}{C_0}$ against $[L]_B$ will be a straight line. The slope of the line gives the value of K, and the x-intercept serves $[L]_T$.

If there are two types of the coordinating sites, $i = 2$,

$$\bar{\theta}_T = \frac{[L]_B}{[L]_T} = \frac{[L_1]_B + [L_2]_B}{[L_1]_T + [L_2]_T} = \frac{K_1 \times C_0 \times [L_1]_T}{1 + K_1 \times C_0} + \frac{K_2 \times C_0 \times [L_2]_T}{1 + K_2 \times C_0} \sum [L_1]_T + [L_2]_T \sum \tag{2.9}$$

After rearranging,

$$\frac{[L]_B}{C_0} = \frac{[L_1]_B + [L_2]_B}{C_0} = (K_1 \times [L_1]_T \quad K_1 \times [L_1]_B) + (K_2 \times [L_2]_T \quad K_2 \times [L_2]_B) \tag{2.10}$$

The plot of $\frac{[L]_B}{C_0} \approx [L]_B$ is no longer linear. The plot can be identified as two linear portions if K_1 and K_2 are very different [27]. K_1, $[L_1]_T$, K_2 and $[L_2]_T$ are determined.

As estimated in [27], there are two types of coordinating sites in PBI: one with high affinity and the maximum doping level of 1 H_3PO_4 molecule per imidazole group; and another one with lower affinity and 3.3 H_3PO_4 molecules per imidazole group in maximum. The coordination occurs first at the site with high affinity via hydrogen bond of -N-H$\times\times$O-P(OH)$_3$ per imidazole ring. When the acid uptake reaches the maximum ($[L_1]_T$), the reaction with lower affinity starts between protonated PBI with H_3PO_4. The additional acid can be bound on imidazole ring directly via the hydrogen bond or indirectly via bonding among H_3PO_4 molecules.

2.3 Gas diffusion electrode

Fig. 2.1a shows that the GDE for anode and cathode can be divided into two parts, a GDL and a catalyst layer. The GDL is made of a matrix of carbon fibres [8, p.519]. In some case, there is another layer, a MPL on top of the GDL [6]. The MPL consists of carbon particles mixed with melted PTFE[4] [45]. The catalyst layer is made of carbon powder supported nanoscale particles of catalytic active metal with a polymeric binder, usually PTFE [46]. Platinum is the most common metal used in HT-PEFC [3; 47].

2.3.1 Gas diffusion layer

There is a great amount of studies on the GDL for fuel cells operated at temperatures lower than 100 °C, PEFC[5] [48–51] and DMFC[6] [52; 53]. One of the big challenges on the GDL development is to manage the water transport and distribution in the MEA for these low temperature fuel cells [4, pp.3-4,3-5; 8, 19]. Since the liquid water is expected to be absent when operating the cell at temperatures higher than 100 °C, the demand on the water management is reduced for the GDL in HT-PEFC [6].

Only a few publications focus on the investigation of the GDL for HT-PEFCs. A commercial GDL, carbon fibre paper purchased from Toray (TGP-H-120), was hydrophobized and deposited with a MPL [45; 54–56]. During the deposition of the MPL, part of the carbon slurry will penetrate the macroporous matrix of the carbon fibres [57]. After drying and heating, the macropores of the carbon fibre matrix are partly blocked. This reduces the gas permeability of the GDL [51]. In addition to an increased mass transfer resistance, an increase of the electronic resistance due to the insulator nature of PTFE [58, pp. 29-30] was found.

Since the catalyst layer has a similar porous structure as the MPL, the catalyst slurry will penetrate the carbon fibre matrix during the deposition if no MPL is present [58, p. 27]. The presence of MPL improves the adhesion between catalyst layer and GDL [45]. There also exists a different opinion that, there is an interfacial gap occurring at the interface between catalyst layer and MPL [59]. The interfacial gap would not only cause an increase in the electronic contact resistance but also generate a disruption on the heat transfer. The situation would be worse if the GDL is unevenly compressed. However, in practice, they are difficult to be determined experimentally.

Lobato *et al.* [45; 55] investigated the effects of the cathodic MPL on the cell performance with the anode including a MPL, and vice versa. It was found out that the presence of a MPL either at the cathode or at the anode is beneficial to the performance of HT-PEFCs.

[4] polytetrafluoroethylene
[5] polymer electrolyte fuel cell
[6] direct methanol fuel cell

2.3.2 Catalyst layer with phosphoric acid

Since the kinetic of the ORR is several orders of magnitudes slower than the HOR [1, p.38; 60, p.92], the performance of a HT-PEFC mainly depends on the cathode reaction. The following discussion focuses on the cathode side. The reaction at the cathode (Eqn. 2.2) involves the transport of electrons, protons, and reactants/products. For a HT-PEFC, the proton conductivities of the anode and cathode are served by phosphoric acid [20; 61].

Therefore, only the catalyst surfaces with contact of the acid solution are electrochemically active, [60, p.237] provided that they are part of a percolating electrical network. The active sites are referred to as the three-phase boundary, as illustrated in Fig. 2.3. The area of the three-phase boundary is normally examined by CV[7] [62, p.444] measurements. The calculations are based on the hydrogen adsorption/desorption on the platinum surface, which presents a characteristic peak in the CV curves [60, p.981-982].

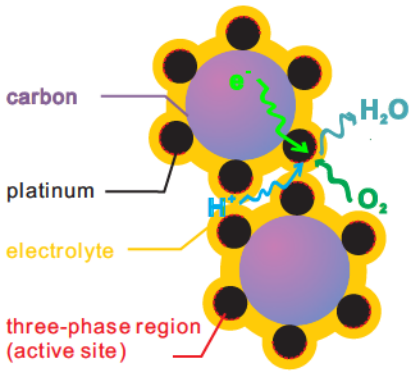

Figure 2.3: Schematic illustration of the ideal three-phase boundary for the cathode catalyst.

As illustrated in Fig. 2.3, the area of active site depends on the acid distribution in the catalyst layer. In addition to the acid content, the distribution of phosphoric acid in the catalyst layer is also determined by the structure of the catalyst layer. The pore size distribution in the catalyst layer has been measured by Lobato *et al.* [47]. It was found that the majority set of the pores ranges from 50 to 120 nm with an overall porosity of around 60 %, depending on the content of the catalyst and binder in the catalyst. These pores are recognized as the meso-pores. Moreover, the catalyst layer is divided into blocks by a great amount of macro-cracks, which are caused during the deposition of the catalyst layer [22; 59; 63]. For a catalyst layer consisting of PTFE as binder, the meso-pores and the macro-cracks can be considered as hydrophobic capillaries [60, pp.893-898; 64], as illustrated in Fig. 2.4. Due to the hydrophobic nature the acid in the catalyst layer will fill the macro-cracks first and afterwards the meso-pores of the catalyst blocks.

The proton transport via the acid solution is also determined by the properties of phosphoric acid. Korte and Chin [65; 66] revealed that the proton conductivity increases with the concentration until

[7] cyclic voltammetry

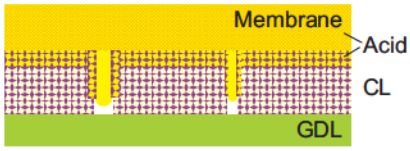

Figure 2.4: Schematic illustration of the acid distribution in the catalyst layer.

a maximum and then decreases with further increasing concentration, as shown in Fig. 2.5. The maximum proton conductivity can be found in an acid concentration range of 30 – 35 wt.(P_2O_5)% at room temperature. The maximum conductivity shifts to higher concentrations when the temperature is raised. At 160 °C, only the right-side of the peak has been reported with the highest proton conductivity in the concentration range of 62 – 65 wt.(P_2O_5)%.

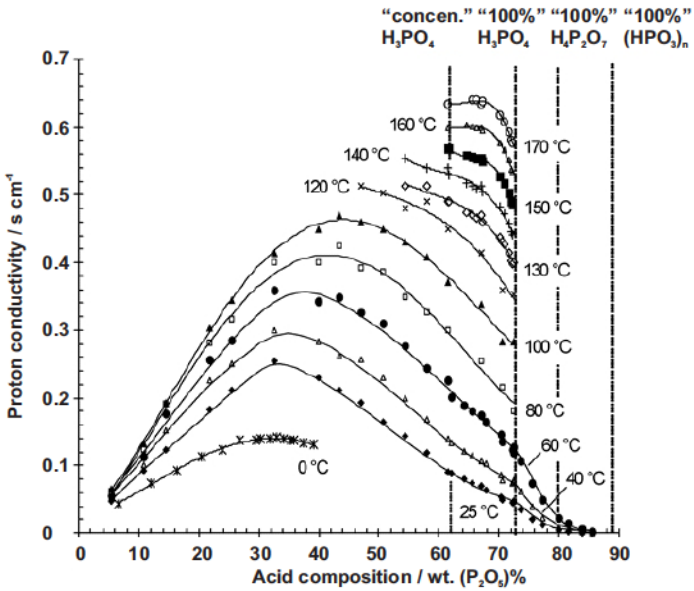

Figure 2.5: Proton conductivity as a function of phosphoric acid composition, redrawn from [65, Fig.12.7].

The concentration of phosphoric acid is a function of the temperature and the water vapor concentration above the surface, see in Fig. 2.6. The acid concentration increases/decreases as the water partial pressure is reduced/raised [65]. This effect is also relevant in the MEA. The equilibrium between electrochemical water production and transport of the vapor through the GDL into the channel influences the concentration and therefore the conductivity of the phosphoric acid inside the MEA.

It is assumed that the phosphoric acid covers the surface of the catalyst particles. As a result the gas molecules have to pass through a liquid film of phosphoric acid to arrive at the catalyst surface

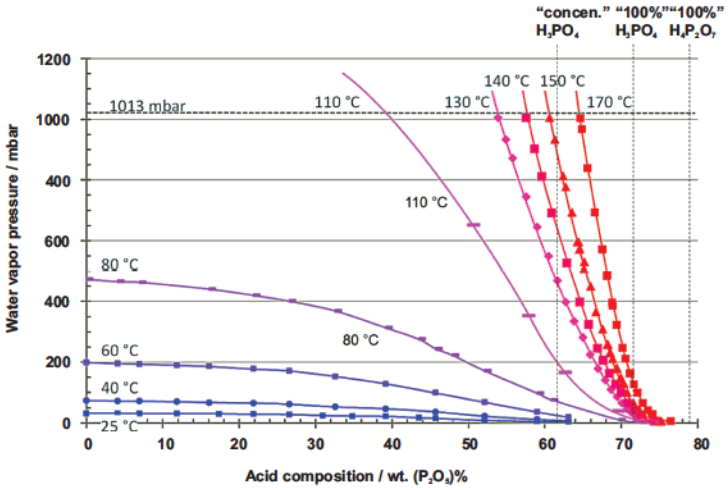

Figure 2.6: Water vapor pressure as a function of phosphoric acid composition, redrawn from [65, Fig.12.2].

Fig. 2.3. The rate of O_2 transport through the acid is believed to be one of the key issues in ORR kinetics [67]. It is promoted by the thinner film of acid solution covered on the Pt surface [68] and the lower acid concentration [69].

In brief, proton, water and oxygen (and hydrogen on the anode side) transport take place in the phosphoric acid solution. Consequently the phosphoric acid has a strong impact on the MEA operational behavior. On one hand, the improved acid content increases the active area and the proton conductivity of the catalyst layer [20; 61; 70]. However, the excess phosphoric acid will block the pathway of O_2 to reach the catalyst surface [10; 68; 71]. The optimum volume fraction of phosphoric acid in the cathodic catalyst layer was estimated to be between 0.3 and 0.55 according to a simulation study [71]. On the other hand, the increased water retention reduces the acid concentration [65], which modifies the O_2 transport [69] and proton conductivity [65].

2.3.3 Degradation of catalyst layer

Durability of the MEA is another major issue for the HT-PEFCs [6]. One reason for the performance losses is the reduction of the active area of the cathodic catalyst [72]. This causes a slow, steady and irreversible performance loss [73, p.204]. The reduced active area is attributed to the growth of crystal grains and particle agglomeration of the catalyst [74; 75], as illustrated in Fig. A8. A theoretical evaluation [76] has revealed that, the performance loss caused by the reduced active area is one order of magnitude lower compared to the experimental determination. If the acid loss in the catalyst layer is also involved in the theoretical evaluation, the calculated performance loss agrees well with the experimental results. However, it has already been confirmed that the evaporation of phosphoric acid during the cell operation is less than 1 wt.-% per 1000 h [72; 77; 78]. Therefore, the acid evaporation has no significant influence on the lifetime of HT-PEFC [73, p.204].

The loss of the acid in the catalyst layer is attributed to the modified distribution of phosphoric acid in the electrode. For a HT-PEFC without external humidification, the distribution of phosphoric acid influences not only the active area but also the proton conductivity of the electrode, as well as the gaseous reactant supply [67]. This fits to the estimation in [77] that the overall degradation was -6 µV h^{-1} at 200 mA cm^{-2}, 55 % of degradation was attributed to the mass transfer limitation, 30 % to the hindered ORR kinetics, and 15 % to a reduction of proton conductivity. This means the combination of the acid loss and the reduced catalyst surface area in the catalyst layer dominates the durability of HT-PEFC under constant load [76; 79].

2.4 Flow field geometry

The performance of the HT-PEFC is determined significantly by the distribution of oxygen and water vapor in the MEA [80–82]. From the viewpoint of the cell design, the gas distribution is strongly controlled by the geometry of the flow field, which provides the pathways for gases. Manso *et al.* [9] summarized the effect of flow field geometries on the performance of a PEFC. As the designs for PEFCs are also suitable for HT-PEFCs [82], the conventional flow field geometries reviewed in [9] have been widely used on the HT-PEFCs, mainly parallel [47; 54; 83], serpentine [12; 22; 61] and interdigitated [81; 84] geometries.

In addition, some new geometries for PEFC flow fields have also been mentioned in [9], including a round spiral flow field [85–89]. In 2004, a spiral-type flow field with interdigitated channels was designed by Cha *et al.* [85]. Since the channels connected to an inlet (inlet channel) and to an outlet (outlet channel) are discontinuous (interdigitated flow field), it forces the gas flow through the GDE under the ribs of the flow channel. A similar effect was described in PEFCs with interdigitated [90; 91], serpentine [92–94] and other spiral flow fields [89], as well as in some HT-PEFCs [81; 82]. The effect is referred to as flow crossover [89; 93], cross-leakage [92] or by-pass [94] between two adjacent flow channels.

The contact between the flow field plate and the GDE is illustrated in Fig. 2.7. Two regions can be identified in the GDE. One region is located under the flow channel and the other under the ribs of the flow field plates. The presence of the flow crossover reduces the pressure drop between the inlet and outlet of a PEFC [95; 96]. The gas flows are forced into the GDE by means of convection [81; 89]. The mass transport of oxygen is improved especially for the region under the ribs [91–93; 97]. For PEFCs, the liquid water enrichment in the region beneath the ribs has been visualized by the *in-situ* characterization [98]. In the presence of flow crossover, the water removal from the region under the ribs is improved by the flow convection [86; 89].

In addition to the discontinuous inlet and outlet channels [85], the flow crossover of the spiral flow field can also be modified by varying the amount of flow channels [87] and the width ratio of the inlet and outlet channels [89] for PEFC. However, there are several disadvantages for these modifications.

Both simulations and experiments confirmed that a suitable flow crossover between adjacent channels is beneficial to the performance and durability of PEFC [86; 93; 97] and HT-PEFC

Figure 2.7: Schematic illustration of electrode regions under the channels and ribs of the flow field plate.

[81; 82; 99; 100].

2.5 Statistical analysis

In this work, the experimental results were analyzed with different statistical tools.

2.5.1 Distribution of experimental data

The experimental results are presented as the mean value along with the associated standard deviation. The mean value ($\bar{x}$) is defined as the average of the collected data (Eqn. 2.11) [101, p.1]. The standard deviation (σ) is calculated by Eqn. 2.12 [101, p.34].

$$\bar{x} = \frac{1}{n}\sum x_i \tag{2.11}$$

$$\sigma = \frac{1}{n\ 1}\sqrt{(x_i\ \bar{x})^2} \tag{2.12}$$

where x_i and n denote a random sample and the sample quantity. The standard deviation is employed and it is calculated with a series of experimental results, which are obtained at least with three repeated measurements for a minimum accuracy. In the illustrated diagrams, the standard deviations are visually presented as error bars. More information about the standard deviation and the underlying statistics can be found in [102, p.25], [103, p.108], [104, p.97].

Histograms are also used to describe the distribution of repeated results [101, pp.14-25]. The collected data are sorted graphically by classes. The type of classes is a range of measured values. The classes are displayed as columns, whereas the height of the column corresponds to the count of the experimental data in the class. Frequency distribution of the collected data can be visualized easily in that way.

Based on the Histograms, the median can be calculated graphically. The median is the point that separates the higher half of a sample from the lower half [101, p.34]. If the sample is close to symmetric distribution, the mean and median are close to each other [101, p.35].

2.5.2 Design of experiment

The optimization of the MEA can be performed using a statistical design of experiments and experimental design evaluation. The statistical design of experiments is a systematic and efficient methodology for planning experiments so that the results obtained can be evaluated to yield objective and valid conclusions [105, p.10; 106, p.109;107, pp.26,37].

In a statistical design of experiments, the experimental conditions and the results are referred to as influence factors and targets. The principle underlying DOE (design of experiment) is that the impact of all factors can be simultaneously investigated with a limited amount of experimental effort, while only one factor is varied in a single series of experiments designed by a classical plan [107, p.26]. The systematically distributed experimental points describe the plan in the form of a design matrix. According to this matrix, a series of experiments are carried out to yield corresponding results, which can be also illustrated in a form of matrix [107, p.26].

After the experimental procedure, the statistical analysis is carried out by using the regression analysis, where the target is quantitatively described with the effecting factors. This analysis therefore estimates the dependence of the target value on the factors in the entire range studied beyond the pre-defined points. The common regression polynomials fit to the experimental data given with a linear or quadratic form [107, pp.26,37].

- A linear model with two factors without interaction:

$$y = c_0 + c_1 x_1 + c_2 x_2 \tag{2.13}$$

- A linear model with three factors including interactions:

$$y = c_0 + c_1 x_1 + c_2 x_2 + c_3 x_3 + c_4 x_1 x_2 + c_5 x_1 x_3 + c_6 x_2 x_3 \tag{2.14}$$

- A quadratic model, with interactions for three factors, normally describes a cube:

$$y = c_0 + c_1 x_1 + c_2 x_1^2 + c_3 x_2 + c_4 x_2^2 + c_5 x_3 + c_6 x_3^2 + c_7 x_1 x_2 + c_8 x_1 x_3 + c_9 x_2 x_3 \tag{2.15}$$

3 Doping Membrane, Cell Assembly and Characterization

The present chapter gives detailed information on the experiments related to the doping of the membrane, the cell assembly and the characterizations of the components. The cells assembled in this way are considered as the standard cell in the whole thesis, and will be used for comparison if cells were assembled in a different way. The reproducibility of the standard cells was studied statistically.

3.1 Doping the membrane

ABPBI membranes with cross-linked structure were supplied by FuMA-Tech GmbH, St. Ingbert, Germany, with a thickness of 45 $\otimes$ 5 µm. The membranes were cut into pieces in a dimension of 1 cm $\pm$ 10 cm. The samples were heated at 150 °C for 0.5 h to evaporate the water and solvent adsorbed in the membranes which remained in the sample after manufacturing and storage.

3.1.1 Doping ABPBI with varied temperature

The dried ABPBI samples were immersed in an acid bath, as illustrated in Fig. 3.1. The entire system was open to air during the doping process. The acid used here was phosphoric acid with a concentration of 85 wt.-%. The temperature of the phosphoric acid bath was varied in the range of 25 °C to 130 °C.

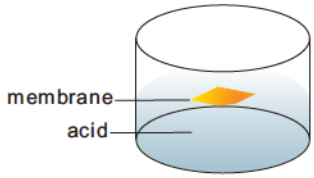

Figure 3.1: Schematic illustration of doping membrane in an open acid bath.

3.1.2 Doping ABPBI with varied concentration

The dry ABPBI samples were immersed in a phosphoric acid bath with pre-defined concentrations from 0 to 14.8 mol L^{-1}. The concentration and density of the acid solutions are listed in Tab. A1. The temperature of the acid bath was set at room temperature or 70 °C.

At room temperature, the samples were doped for one year in order to approach the equilibrium. This long term doping process took place in a closed glass flask to avoid the change of the acid concentration [27]. At 70 °C, the samples were doped in an open system for 15 h to approach the equilibrium. The system involved a reflux device to minimize the concentration change of phosphoric acid during doping. The experiments were repeated three times.

3.1.3 Doping level of ABPBI

The weight of the membrane increased after doping in the acid solutions. The weight gain can be used to calculate the acid doping level by Eqn. 3.1. The details are listed in Tab. 3.1.

$$Q_A = \frac{W_{Md} \quad W_M}{W_M} \pm 100\,\% = \frac{W_{PA}}{W_M} \pm 100\,\% = \frac{x_A \times A}{n \times M} \pm 100\,\% \tag{3.1}$$

Q_A	wt.-%	doping level of phosphoric acid of the doped membrane
W_M	g	weight of membrane before doping
W_{Md}	g	weight of membrane after doping
W_{PA}	g	weight of phosphoric acid in doped membrane
x_A	mol	number of mole phosphoric acid in doped membrane
n	mol	number of mole polymer repeat unit in membrane
A	g mol^{-1}	molar mass of phosphoric acid, 98 g mol^{-1}
M	g mol^{-1}	molar mass of repeat unit of ABPBI, 116 g mol^{-1} as structure shown in Fig. 2.2b

Table 3.1: Physical quantitative characterization of the doped membranes.

	Direct weight	Vacuum heating
Articles	dry membrane	doped membrane
Information	weight gain after doping	weight loss after vacuum heating
Calculated result / wt.-%	$W(ABPBI)$, $W(H_3PO_4 + H_2O)$	$W(H_2O)$

In order to separate the contribution of H_3PO_4 and H_2O, the content in the doped membrane was investigated quantitatively. A vacuum heating was carried out as described in [22; 27]. The doped membranes were heated in a vacuum oven as soon as they were taken out of the acid bath. The working pressure in the vacuum oven is lower than 10 mbar. The temperature inside the oven was set as 105 °C to evaporate the water until a constant mass was reached, normally after 5 h. The mass loss during the vacuum heating is associated with the loss of H_2O in the doped membrane.

Therefore, the uptake of H_2O can be distinguished from the H_3PO_4 uptake, as listed in Tab. 3.1. Considering the results obtained from the weight without further treatment, the content of H_3PO_4 in the doped membrane was observed. Due to the fact that in the literature no data of the behavior of phosphoric acid under very low pressure is available the results have to be treated carefully. Considering the heating process under atmospheric pressure, the evaporation of loosely bound water in doped ABPBI completes at 100 °C, and the elimination of water during the dehydration starts at 117 °C [108]. Therefore, part of water still remained in the doped membrane due to the equilibrium of the phosphoric acid dehydration and hydration [109]. In calculation, the weight of water in the membrane was taken as the weight of H_3PO_4. The doping level of H_3PO_4/H_2O uptake will be higher/lower than the real value. The influence is obvious when the total doping level is at the low level. The same problem should have also occurred in [27; 38].

The content of the components in the doped membrane can also be characterized using chemical analysis, for instance, combustion elemental analysis and IC[1] [110, pp.159-160]. The principles of two techniques are described briefly in Appendix A2.2. Both characterization methods were performed in Central Institute for Engineering, Electronics and Analytics (ZEA-3), Forschungszentrum Jülich GmbH.

The doped membrane was cut into pieces and burned in the elemental analyzer (CHN Modus, VarioELcube, Elementary). The element detection was performed with a thermal conductivity detector. The content of carbon in the sample was obtained, which was used to calculate the weight ratio of ABPBI in the doped membrane, as listed in Tab. 3.2. The specified error is less than 0.4 wt.-% in absolute. Tab. 3.2 shows that the content of H_3PO_4 in the doped membrane can be characterized by means of IC technique. The IC characterization was performed by Dionex ICS-3000 (AS14 column) with the eluent of 1 mmol sodium bicarbonate and 8 mmol sodium carbonate. The analytical error is $\otimes$ 5 % in relative.

Table 3.2: Chemical quantitative characterization of the doped membranes.

	Combustion elemental analysis	Ion chromatography
Articles	doped membrane	doped membrane
Information	weight ratio of carbon	weight ratio of PO_4^{3-}
Calculated result / wt.-%	$W(ABPBI)$, $W(H_3PO_4 + H_2O)$	$W(H_3PO_4)$

It should be noted that the experimental errors mentioned above do not contain the errors caused during the sample preparation for the elemental characterization. The handling of the samples results in further errors. The doped membrane samples were cut into small pieces. When the samples were taken out of the acid bath, the phosphoric acid adsorbed water from the air and a liquid layer was gathered on the sample's surface resulting in a high uncertainty of the experimental results. This brings a great experimental error to the quantitative results, significantly for the samples with higher doping levels, as shown in Fig. A3 and Fig. A4.

The vacuum heating is used to determine the samples with the high doping level, and the chemical

[1] ion chromatography

characterization for the samples with the lower doping level.

3.2 MEA and cell assembly

3.2.1 Electrode preparation

The GDEs were prepared by means of the doctor blade technique [22], as illustrated in Fig. 3.2. The GDL is composed of non-woven carbon fibres with a microporous layer (Freudenberg FCCT KG, H2315-CX165). The catalyst slurry consists of platinum catalyst powder (20 wt.-%, HisPec Johnson Matthey), PTFE dispersion (60 wt.-%, Dyneon), water and alcohols. The slurries were dispersed with an ultrasonic horn and coated on the GDL by a blade. Afterwards, the GDEs were dried in the fume hood overnight and heated in the oven at 60 °C for 30 min.

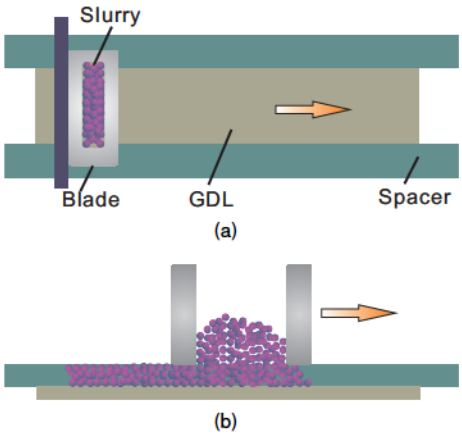

Figure 3.2: Schematic representation of the catalyst layer deposition: (a) top- and (b) side-view.

The dried catalyst layer contains 12 wt.-% of Pt, 48 wt.-% of carbon powder and 40 wt.-% of PTFE. The platinum loading per cm^2 was calculated based on the weight difference of the sample before and after deposition. The thickness increment is attributed to the thickness of the catalyst layer. The thickness of the GDL and GDE were measured by the instrument of Extramess 2000 (Mahr GmbH) under a force of 1 N.

As illustrated in Fig. 3.2, the thickness of the catalyst layer can be easily modified by the thicknesses of the spacers. When the spacer with a thickness of 1.0 mm was chosen, the thickness and the platinum loading of the catalyst layer on a GDL with MPL were achieved as $119 \otimes 9\,\mu m$ and $0.94 \otimes 0.05\,mg\,cm^{-2}$.

3.2.2 Introducing acid into the MEA

Phosphoric acid doped ABPBI membrane was used as proton conductive membrane in the HT-PEFCs. ABPBI membranes were supplied by FuMA-Tech GmbH, St. Ingbert, Germany, with a thickness of 45 $\otimes$ 5 µm. Before doping, the membrane samples were heated to 150 °C to evaporate the water and remaining solvent absorbed in the membranes. Subsequently, the samples were immersed in the acid bath to introduce acid into the membrane [99], as illustrated in Fig. 3.1. For the standard MEA, the phosphoric acid with a concentration of 85 wt.-% was used as the acid bath. The temperature of the acid bath was set to 110 °C. After a doping time of 15 h, the saturation of acid in the membrane was achieved. This resulted in an acid uptake of 15 $\otimes$ 1 mg cm^{-2}.

If the required acid uptake in the MEA was higher than the adsorbed amount of acid in the membrane, the additional acid solution was introduced directly onto the GDE [22; 111–113]. A solution of 85 wt.-% phosphoric acid and ethanol was prepared, with a volume ratio of 4:1. A predefined volume of the solution was dropped in terms of a chess pattern over the whole electrode.

3.2.3 Cell assembly

The MEA contains a phosphoric acid-doped ABPBI membrane, two GDEs and gaskets made of PFA[2] or PTFE polymer [22; 111], as shown in Fig. 3.3a. The MEAs were assembled inside the cell without a proceeding hot-pressing step. During the assembly, the MEAs were compressed to 75 % of their initial thickness. The active area of the MEA was 14.44 cm^2.

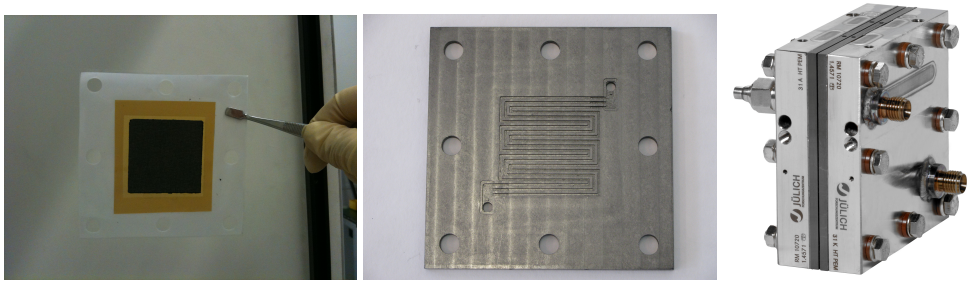

(a) (b) (c)

Figure 3.3: (a) Photograph of an assembled MEA. Black sheet: GDE; orange sheet: ABPBI membrane; white sheet: gaskets.
(b) Photograph of a flow field plate with a serpentine geometry.
(c) Photograph of an assembled HT-PEFC (single cell).

Graphite composite flow field plates with serpentine gas channels were used [99; 100; 114] see Fig. 3.3b. The width and depth of channel have the same dimension of 1.0 mm, as well as the width of land. The metallic endplates were heated in order to adjust the operating temperature. The assembled cell is shown in Fig. 3.3c.

[2] perfluoroalkoxy

3.3 Physical characterization

3.3.1 Catalyst loading gradient of the catalyst layer

The catalyst layer of the GDE was deposited with a fixed speed of the doctor blade technique. After drying, the GDE was cut into pieces to analyze the catalyst loading gradient along the coating direction, as illustrated in Fig. 3.4. The thickness of the catalyst layer and the platinum loading of each piece can be plotted against the position. The experiments were repeated three times.

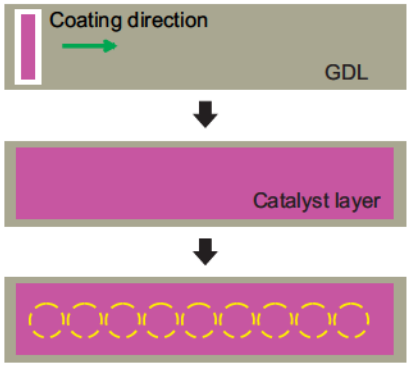

Figure 3.4: Schematic representation of the analysis of the catalyst loading gradient.

3.3.2 Air permeability of GDL and GDE

The air permeabilities of GDLs and GDEs were characterized by the Gurley Number [8, 15], which denotes the time required by 100 ml air to pass through the porous material under examination. The GDL and GDE samples with a size of 5 cm $\pm$ 5 cm were mounted into the instrument. The pre-defined volume of air flowed through the sample from the back side to the top side. The top side is recognized as the side with the catalyst layer for the GDE samples or with the MPL for the GDL samples. The time interval was recorded automatically to mark the start and the end of the air permeation. A series of experiments was carried out with a Gurley air permeabilimeter (Gurley Precision Instruments, model No. 4118N, USA) according to the standard method ISO 5636-5 (2003) [115]. The timing was recorded by the Genuine Gurley ™4320 Automatic Digital Timer.

The experiments were repeated seven times for each sample. The mean value was used to calculate the Gurley number and the air permeability by Eqn. 3.2 and Eqn. 3.3 [115].

$$t_{Gurley} = t_{mess} \times \frac{1}{4} \times \frac{1}{10} \times \frac{100}{V} \tag{3.2}$$

$$P = \frac{127}{t_{Gurley}} \tag{3.3}$$

t_{Gurley}	(Pa s) µm	Gurley number
t_{mess}	s	the recorded time in the experiment for air permeating through the sample
V	ml	the volume of air used in the experiment for air permeating through the sample
P	µm $(Pa\,s)^{-1}$	air permeability of the sample

3.3.3 Pressure difference between inlet and outlet of cell

The assembled cells were fixed into the test rig and fed by N_2 with a pre-defined flow rate of 200 ml min^{-1}. The outlet of the cell was open to ambient pressure and no back pressure was applied. The pressure difference between the inlet and outlet was measured by a manometer of PCE - P01 (PCE Instruments UK Ltd.).

Pressure drop experiments were performed with cells containing MEAs and with cells without MEAs in order to determine the influence of the GDL on the pressure drop. In the latter case the cells were assembled with a low-permeable film of PFA with a thickness of 300 µm instead on a MEA. The influence of the porous electrode on the pressure drop of the cell was evaluated by the pressure ratio of the cell assembled with PFA to the one with MEA, $\Omega P_{PFA} : \Omega P_{MEA}$.

3.4 Electrochemical characterization

3.4.1 Break-in process

The cells were fixed into the test-rig. H_2 was fed to the anode and air to the cathode. The dew point of H_2 and air were -50 °C and -58 °C, respectively as listed in Tab. 3.3. In the following this gases are considered of being dry. The cells were heated up to 160 °C under atmospheric pressure and OCV[3]. Current was drawn after 1 h and was increased up to 200 mA cm^{-2} with steps of 50 mA cm^{-2}. Each step was held for 5 min. Afterwards, the current density was kept constant for 70 h. The flow rate during the break-in process was performed with a stoichiometry of $\lambda_{H_2/air}$ = 2/2 at 200 mA cm^{-2}. The break-in procedure is illustrated in Fig. 3.5.

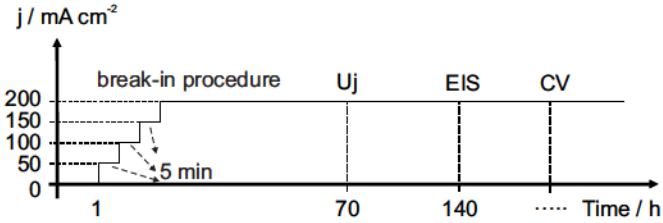

Figure 3.5: Diagram of break-in procedure and following electrochemical characterizations.

[3]open circuit voltage

Table 3.3: Water content in fed gases.

	Dew point / °C	p_{H_2O} / mbar
air *	-58	0.025
H_2 †	-50	0.064
N_2 †	-50	0.064

* *The gases are dried in local laboratory'*
† *The gases are purchased from company of Air Liquide.*

3.4.2 Polarization curve

At the end of the break-in process, the load was switched off. The cell was operated at OCV. After 5 min, the current was switched on. The current density was increased in steps of 25 mA cm^{-2}. Each value was held for 1 min. The current was increased until a voltage level of 0.3 V was reached, and then decreased to OCV with the same step size. The scans were repeated twice. The forward part of the second scan was chosen to characterize the performance of different cells.

The flow rate was set to a stoichiometry of $\lambda_{H_2/air}$ = 2/2. In the case of a current density below 200 mA cm^{-2} and OCV, the flow rate was kept identical to the one at 200 mA cm^{-2}. In addition, the polarization curves were also recorded at different stoichiometries, for example 1.2 and 6 at the cathode.

3.4.3 Electrochemical impedance spectroscopy

To quantify resistances of HT-PEFC, EIS[4] measurement was carried out with an IM 6 unit of Zahner Elektrik. The cells were operated under pre-defined current densities and stoichiometries. The excitation voltage for the impedance measurement was chosen to be 5 mV in a frequency range of 100 kHz – 100 mHz. The obtained Nyquist plots were fitted with an equivalent circuit considering the classical transition line model as shown in Fig. 3.6 [67; 70; 116; 117].

L	Henry	cable inductance
R_o	m cm^2	ohmic resistance
R_p	m cm^2	proton resistance
R_{ct}	m cm^2	charge transfer resistance (kinetic resistance)
CPE_{ct}	Farad cm^{-2}	constant phase element of ORR kinetic
R_m	m cm^2	mass transport resistance
CPE_m	Farad cm^{-2}	constant phase element of mass transport

The sum of resistances is referred to as the total resistance by Eqn. 3.4.

$$R_{total} = R_o + \frac{1}{3}R_p + R_{ct} + R_m \tag{3.4}$$

[4] electrochemical impedance spectroscopy

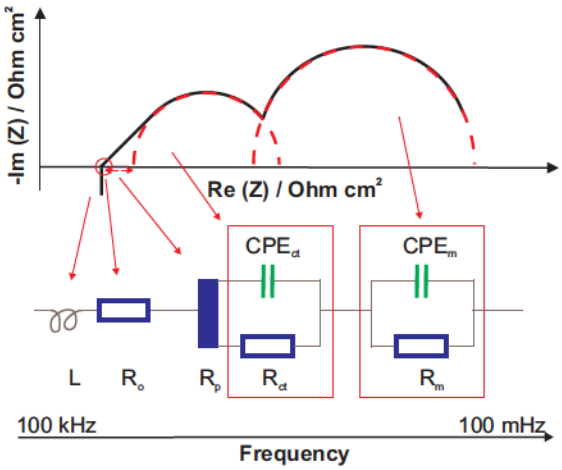

Figure 3.6: Equivalent circuit with classical transmission line model for the typical Nyquist plot of HT-PEFC.

3.4.4 Durability experiment

Durability experiment up to 1000 h was performed for some cells under a constant load and stoichiometry. These measurements were only interrupted during the recording of polarization curves every 70 h and EIS every 500 h.

3.4.5 Cyclic voltammetry

CV[5] was also performed to evaluate active area of the cathode [18; 60, p.389]. CV scans over the applied potential range might injure the cells. Therefore, the CV measurements were carried out at the end of the operation. An IM 6 unit from Zahner Elektrik was used for these measurements. The experiments were performed in the following way. The current load was switched off. The anode was fed with a H_2 flow of 4.6 ml $min^{-1}cm^{-2}$. The anode served as a counter and pseudo-reference electrode. The cathode was fed with a N_2 flow of 6.9 ml $min^{-1}cm^{-2}$ in order to remove the remaining oxygen. The O_2 free cathode was considered as the working electrode and the sense. The cathode flow was switched off before the CV recording. The plots of CV were recorded in a voltage range of 50 – 505 mV with a scan rate of 20 mV s^{-1}. The typical CV curve is illustrated in Fig. 3.7.

The scan was repeated until a stable CV was achieved. Usually 10 cycles were needed. The last scan was chosen to calculate ECSA[6] by Eqn. 3.5 [60, p.515]. ECSA in unit of $m^2\,g^{-1}$ can be considered as the cathodic catalyst efficiency [60, p.983]. When the catalyst loading of the cathode was varied, the absolute area of the electrochemical surface area needs to be considered [46], as

[5] cyclic voltammogram
[6] electrochemical surface area

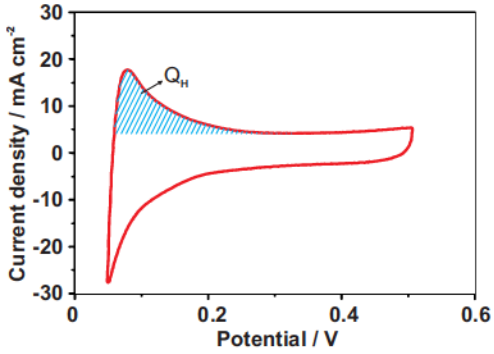

Figure 3.7: Typical curve of cyclic voltammogram.

defined by Eqn. 3.6. Comparing Eqn. 3.6 and Eqn. 3.5, $A_{act.}$ is the product of ECSA, the cathodic catalyst loading and the active area of MEA.

$$ECSA = \frac{Q_H}{\upsilon \times \ \times L} \tag{3.5}$$

$$A_{act.} = \frac{Q_H \times A}{\upsilon \times} \tag{3.6}$$

$ECSA$	$cm^2\ g^{-1}$	electrochemical active area of the cathode catalyst
Q_H	$V\ mA\ cm^{-2}$	absolute area of the hydrogen desorption peak
υ	$20\ mV\ s^{-1}$	scan rate of CV cycle
$\frac{Q_H}{\upsilon}$	$\mu C\ cm^{-2}$	charge density of the hydrogen desorption on Pt surface
	$\mu C\ cm^{-2}$	charge needed to desorb a monolayer of protons on Pt surface, which was taken as $210\ \mu C\ cm^{-2}$ [60, p.515]
L	$mg\ cm^{-2}$	platinum loading of the cathode
$A_{act.}$	cm^2	active surface area of cathode catalyst
A	cm^2	active area of MEA

3.4.6 Water collection

During the cell operation, the produced water was collected at the outlet of the cells. The temperature of the outlet gas condensation was 7 °C. In this case the total water collection is more than 95 % of the water production according to Faraday's law [1, p.21]. The rest of water was remained in the exhaust gas. The mass ratio of water collected at the anode to the total water collection is referred to as the water anode ratio:

$$w = \frac{m_{An.}}{m_{An.} + m_{Ca.}} \pm 100\,\% = \frac{m_{An.}}{m_{Total}} \pm 100\,\% \tag{3.7}$$

w	%	water anode ratio
$m_{An.}$	g	mass of water collected at anode outlet
$m_{Ca.}$	g	mass of water collected at cathode outlet
m_{Total}	g	mass of total water collection

3.5 Morphology and structure characterization

3.5.1 Microscopy

The surface and the cross-section morphologies of the GDL and GDE were detected by a microscope of Zeiss Axio Imager.M1m with a camera of Axio Cam MRc. The images were analyzed with the software of Axio Vision. The cross-sections of the samples were polished before the images were taken by a set of instruments, Struers Tegra Pol-21, Tegra Force-5 and Tegra doser-5.

3.5.2 Grain size of platinum

XRD[7] was employed to characterize the grain sizes of platinum in catalyst [72; 73; 77]. The catalysts were scraped from the GDEs. New and aged electrodes were examined for comparison. In addition, the initial catalyst powder was also tested as reference.

The powders of the samples were filled in a sample holder, carefully smoothed and adjusted against a knife edge. The XRD characterization were performed on STOE θ/θ- Diffractometer using Cu- Kα- radiation (λ = 1.5418 Å): a voltage of 40 kV, a current of 35 mA, an angle region (2θ) of 15-90 °, a step ($\Omega 2\theta$) of 0.04 ° and a duration per step of 4 s. The quality phase analysis was completed with Crystallographica Search/Match and ICDD (International Centre of Diffraction Data) PDF4+ (Powder Diffraction File), using version Set 61 (2011). The quantitative phase analysis was achieved with Rietveld program SiroQuant ®Version 3. The crystallite sizes were determined by the reflections (111), (200) and (200).

The XRD characterization and analysis were carried out by the company of RÖNTGENLABOR-Dr. Ermrich, Reinheim, Germany.

3.6 Statistical study

The data obtained from the experiments were evaluated with the software OriginPro 8.5.1 (OriginLab Corporation), for mean, standard deviation of mean, median and Histograms. A DOE (design of experiment) software program, STATGRAPHICS Centurion XVI from the commercial company StatPoint Technologies, Inc., was employed to evaluate the experiments with three variables. The fitted results were expressed in three-dimensional graphics cubes.

[7] X-ray diffraction

3.7 Reproducibility of HT-PEFCs (single cells)

The cells assembled as described in Section 3.2 are considered as the standard cells in the whole work. The reproducibility of the MEA preparation and the cell assembly was verified with polarization curves. Fig. 3.8 shows polarization curves of the 10 standard cells recorded after the break-in process, as mentioned in Section 3.4. The voltages at 0.2 A cm^{-2} and the slopes in the voltage range of 0.3 $\approx$ 0.6 V were collected and analyzed statistically. The obtained results are listed in Tab. 3.4, and Histograms for two parameters are plotted in Fig. 3.9.

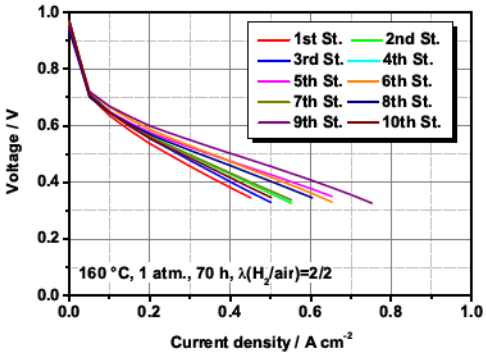

Figure 3.8: Polarization curves of standard cells with $\lambda_{H_2/air}$ = 2/2. The curves were recorded at 160 °C after a break-in process of 70 h.

Table 3.4: Statistical analysis of the standard cells performance.

	Voltage at 0.2 A cm^{-2} / V	Slope (0.3 $\approx$ 0.6 V) / cm^2
Mean	0.564	-0.632
Standard deviation of mean	0.016	0.107
Median	0.563	-0.644

- *The original data obtained from Fig. 3.8.*
- *The count of the samples is 10.*

For the voltage at 0.2 A cm^{-2}, as listed in Tab. 3.4, the differences between mean and median are one order of the magnitude smaller than the standard deviation, so that the mean and median can be considered as the same. It means the voltage at 0.2 A cm^{-2} is symmetrically distributed [101, p.35]. The amount of the cells in different voltage ranges are shown in Fig. 3.9a. The majority class of the voltage is located in the range from 0.55 V to 0.57 V. Considering the mean voltage of 0.564 V, the reference cells in the following chapters were taken as the ones with the voltage in the range of 0.55 $\approx$ 0.57 V at 0.2 A cm^{-2}.

In contrast, the standard deviation of the polarization curve slope (0.3 $\approx$ 0.6 V) is six times larger than that of the voltage at 0.2 A cm^{-2}. Fig. 3.9b shows the slope scattered in a wider range

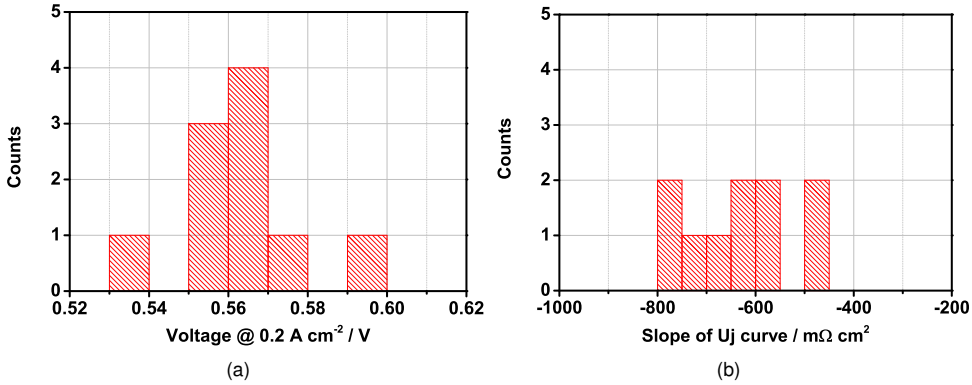

Figure 3.9: Histograms: (a) voltage at 0.2 A cm^{-2} and (b) slope in the range of 0.3 $\approx$ 0.6 V. The data were obtained from Fig. 3.8. In total, data from 10 cells were involved.

without obvious majority. In other words, the polarization curve slope is more influenced by the uncertainty in comparison to the voltage at 0.2 A cm^{-2}. The uncertainty includes the variation of the initial material quality, for example the ABPBI membranes, and the process during the cell preparation and assembly.

4 Determination of Acid Doping Level I

The content of phosphoric acid in the ABPBI membrane is one of the critical issues for the performance of the HT-PEFCs. It is important to understand the mechanism of the reaction between phosphoric acid and ABPBI polymers. As the first step, the kinetics of the doping process was investigated experimentally in the present work. The doping procedure was carried out at different temperatures.

Part of this work has been published as abstract and oral presentation at the 3rd Carisma International Conference, Copenhagen, September 2012; as well as an abstract and poster presentation in the conference of GDCh Electrochemistry 2012, München, September 2012.

4.1 Doping level of ABPBI membrane

The ABPBI membrane samples were immersed in a bath of 85 wt.-% phosphoric acid, as shown in Fig. 3.1. The temperature of the phosphoric acid bath was varied in the range from 25 °C to 130 °C. The acid doping level is defined as the weight ratio of the doped membrane to the dry membrane according to Eqn. 3.1. The calculated results are plotted in Fig. 4.1.

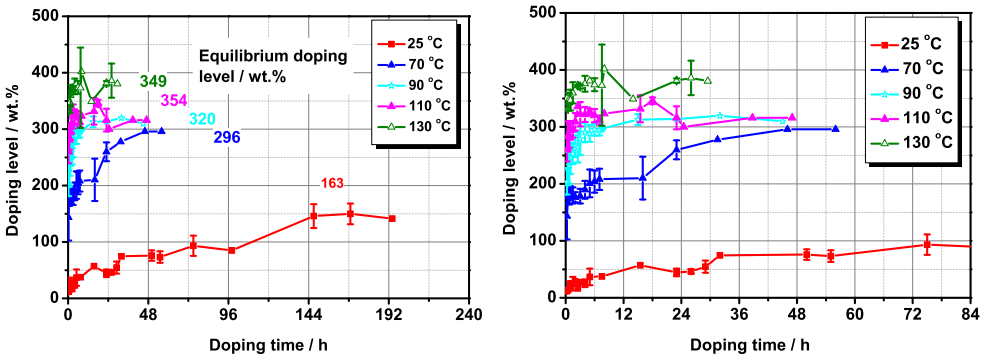

Figure 4.1: Doping level of ABPBI membranes at different temperatures of the acid bath in the open system. (b) is a magnification of (a) in the time range of 0 – 84 h. The acid was 85 wt.-% phosphoric acid. The error bars are standard deviation in absolute values.

The doping level increased significantly in the first two hours. The increase in doping level slowed down after 6 h until the constant value was obtained. Fig. 4.1 shows that less time was required to approach the steady state at higher temperature. In the experiment, the highest constant doping level was assumed as the equilibrium doping level, which is noted in Fig. 4.1a for the different doping temperatures. The value of the equilibrium doping level increased with the doping temperature. This means the enhanced temperature is advantageous for the doping reaction. Therefore, the doping process can be considered as an endothermic reaction [25, p.29]. The increased equilibrium doping level obtained at higher temperature is associated with the enhanced concentration of the acid solution due to the water evaporation from the acid bath during the experiment [108]. The effect of the acid concentration on the equilibrium doping level will be discussed in Chapter 5. In addition, the mobilities of ABPBI polymer chains could be promoted at higher temperature [118, pp.569-572], which provides more volume space for acid diffusion into the membrane.

Fig. 4.1 shows that the deviation of the doping level is $\otimes$ 25 wt.-% (10 % in relative), which is independent of the experimental temperature and doping time. There is no direct relationship between the doping level and the thickness and the area weight of the initial membrane (Fig. A1). The variation can be related to the uneven macro-structure of the membrane caused during the casting process [118, pp.569-572]. This leads to large variations in the results of the measured dimensions as a function of doping time (Fig. A2). The dimension variation can also be plotted as a function of the doping level. Fig. 4.2 shows that both area and thickness of ABPBI samples increase proportionally with the doping level. The volume of the membrane was expanded by 10-200 % in a range of the doping level from 10 wt.-% to 400 wt.-%. The swelling effect was also observed for PBI membranes [119]. From another viewpoint, the expanded volume can be considered as the volume of phosphoric acid in the doped membrane. The volume fraction of acid in the doped membrane can be calculated based on the data in Fig. 4.2. It increases up to 60 vol.-% when the doping level is 400 wt.-%.

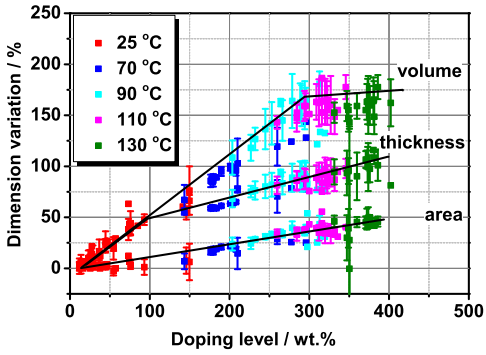

Figure 4.2: Dimension variation of doped ABPBI as a function of acid doping level. The values of doping level were obtained from Fig. 4.1, and the data of dimension variation from Fig. A2. The error bars are standard deviation in absolute values.

4.2 Reaction rate law

4.2.1 Available sites

Fig. 4.1 shows that the weight of the ABPBI samples rises after doping in the bath of phosphoric acid. The weight gain is associated with the acid diffusion into the matrix of ABPBI polymer chains. The doping process can be considered as an adsorption of phosphoric acid by the polymer chains. In a doped membrane, each acid molecule stays at a specific volume close to the polymer chain. The specific volume is defined as available site, L, [27]. Each polymer repeat unit contains a small amount of available sites. The amount is constant at a certain temperature for the polymer. The reaction between acid and membrane chains is the process of the acid molecules "occupying" the available sites. The reaction can be illustrated as shown in Fig. 4.3.

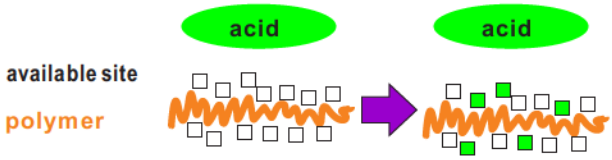

Figure 4.3: Schematic image of acid occupying available sites of polymer chains.

The reaction can be expressed as the chemical equation:

	L	+	acid	⇌	L×acid
$t = 0$	$[L]_T$		C_0		0
$t = t$	$[L]_F$		C_t		$[L]_B$
$t = t_e$	$[L]_F$		C_e		$[L]_e$

t	h	doping time
t_e	h	time required to reach the equilibrium
C_0, C_t, C_e	wt.-%	acid concentration at initial, t and t_e
$[L]_T$	%	concentration of total available site
$[L]_B$	%	concentration of occupied available site
$[L]_e$	%	concentration of occupied available site at equilibrium
$[L]_F$	%	concentration of free available site, $[L]_F = [L]_T \quad [L]_B$

As definition, the concentration of the total available site ($[L]_T$) is the molar ratio of the total available sites to the amount of repeat units (n) in the membrane. The total available site is the product of n and the available site number per repeat unit (l). The equation can be written as Eqn. 4.1.

$$[L]_T = \frac{n \times l}{n} \pm 100\,\% \tag{4.1}$$

The concentration of the occupied available sites ($[L]_B$) is the molar ratio of the occupied available site (x_L) to the repeat unit in the membrane, as Eqn. 4.2.

$$[L]_B = \frac{x_L}{n} \pm 100\,\% \tag{4.2}$$

Since each available site can only be occupied by a single acid molecule, x_L is equal to the amount of the acid (x_A) in the doped membrane.

$$x_L = x_A \tag{4.3}$$

Comparing Eqn. 3.1, Eqn. 4.2 and Eqn. 4.3 gives Eqn. 4.4.

$$[L]_B = \frac{M}{A} Q_A \tag{4.4}$$

If C_0 remains higher than $[L]_B$, the concentration of the occupied available site at equilibrium ($[L]_e$) is equal to the concentration of total available site ($[L]_T$).

$$[L]_e = [L]_T = \frac{M}{A} Q_{A,max} \tag{4.5}$$

$[L]_B$, $[L]_T$ and $[L]_e$ are proportional to the real doping level (Q_A) since both A and M are constant for the investigated system. In the following study, $[L]_B$, $[L]_T$ and $[L]_e$ will be regarded as the doping level of the membrane at the different stages of the doping process.

Based on these conditions, the reaction rate law can be investigated. However, the acid solution contains H_3PO_4 and H_2O, which are both introduced into the ABPBI membranes [39]. Different possibilities of H_3PO_4 and H_2O occupying the available sites have to be considered.

i : As an acid, H_3PO_4 is more active than H_2O to react with the imidazole ring in ABPBI. Therefore, the available sites are occupied only by H_3PO_4 which is used as assumption. The available sites of the polymer chains are occupied with H_3PO_4 molecules. Part of H_3PO_4 molecules are bound with H_2O molecules. In this way, H_2O is introduced into the membrane.

ii : Both H_3PO_4 and H_2O can occupy the available sites. The adsorption occurs among the available sites, H_3PO_4 and H_2O.

The following sections will examine which possibility is the dominant reaction during the doping process. The investigation will be carried out by determining the rate law of the doping process.

It should be noted that the reaction equation discussed is only based on the consideration of the weight gain of the doped membrane. The real chemical reactions between acid and polymer are not regarded in this study. The chemistry of the doping process will be discussed in Chapter 5. In addition, the dehydration and association of phosphoric acid [109; 120] are also not taken into account here.

4.2.2 Pseudo-first-order rate law

As mentioned, the incorporation of phosphoric acid into the membrane can be considered as the adsorption of phosphoric acid by the ABPBI polymer chains. It is assumed that the available sites of the ABPBI polymer chains are occupied only by H_3PO_4 molecules, as illustrated in Fig. 4.4. A certain amount of H_2O molecules will be transferred into the membrane through bonding at the H_3PO_4 molecules.

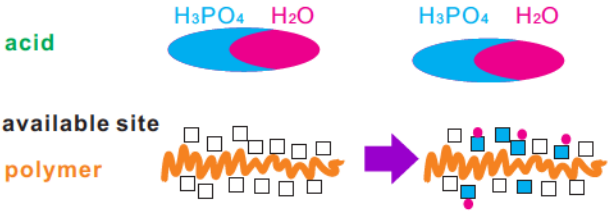

Figure 4.4: Schematic image of available sites occupied by H_3PO_4 molecules. Part of H_3PO_4 molecules are bound with H_2O molecules.

The concentration of the phosphoric acid bath is assumed as constant during the doping process, since the volume of phosphoric acid in bath is three orders of magnitude higher than what is introduced into the membrane. The reaction formula of the doping process is expressed as:

$$\begin{array}{lccccc} & \mathrm{L} & + & \mathrm{H_3PO_4} & \rightleftharpoons & \mathrm{L\times H_3PO_4} \\ t=0 & [L]_T & & C_0 & & 0 \\ t=t & [L]_T\ \ [L]_B & & C_0 & & [L]_B \end{array}$$

The reaction can be supposed as a pseudo-first-order reaction. Therefore, the reaction rate depends on the concentration of available site, as written in Eqn. 4.6 [26; 121].

$$r = \frac{d([L]_T - [L]_B)}{dt} = k_1 C_0([L]_T - [L]_B) = k_1'([L]_T - [L]_B) \tag{4.6}$$

r	wt.-% h^{-1}	reaction rate
C_0	wt.-%	concentration of H_3PO_4 in acid bath
k_1	wt.-%$^{-2}$ h^{-1}	reaction rate constant
k_1'	h^{-1}	pseudo-first-order rate constant, $k_1' = k_1 C_0$

Rearranging of Eqn. 4.6 gives

$$log([L]_T - [L]_B) = log[L]_T - \frac{k_1'}{2.303}t \tag{4.7}$$

k_1' can be obtained from the slope of $log([L]_T - [L]_B)$ against the doping time, as shown in Fig. 4.5. The values of k_1' at different temperatures were listed in Tab. 4.1, which also contains the values of the equilibrium doping level and regression coefficients. When the membrane samples were doped at 25 °C, the regression coefficient value was 0.95, and the calculated equilibrium doping

level ($[L]_T$) was lower by 20 wt.-% than the experimental equilibrium doping level. The difference between the calculated and the experimental value is smaller than the deviation of the doping level ($\otimes$ 25 wt.-%, see in Fig. 4.1). In other words, the calculated equilibrium doping levels are consistent with the experimental values. This means the pseudo-first-order model is appropriate to describe the doping process at room temperature. Therefore, the reaction rate is proportional to the concentration of free available site raised to the first power. The same reaction rate model was also appropriate for doping PBI at room temperature [23]. The value of $k_1{}'$ here is 3 orders of magnitude higher than the one obtained for PBI-phosphoric acid system in [23]. This is caused by the higher concentration of the acid bath in this study, 85 wt.-%, compared to 30 wt.-% and 70 wt.-% in the literature. As the acid concentration increases, the viscosity of the solution also increases [24]. This leads to a slower kinetic of the doping process and a lower rate constant [23].

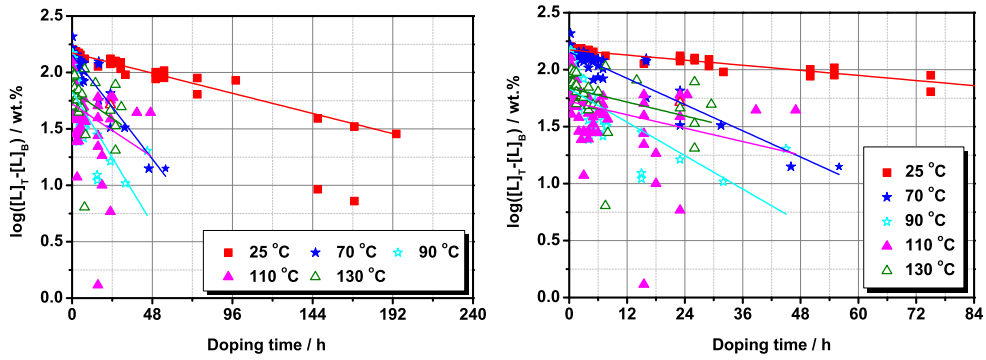

Figure 4.5: Pseudo-first-order plots of phosphoric acid adsorption on ABPBI polymer chains. The original data were obtained from Fig. 4.1. (b) is the magnification of (a) in the period of 0 – 84 h.

Table 4.1: Fitted results obtained with pseudo-first-order rate law.

Doping temperature	Experimental equilibrium doping level (from Fig. 4.1a)	Calculated equilibrium doping level ($[L]_T$)	R^2	$k_1{}'$
°C	wt.-%	wt.-%		h^{-1}
25	163	143	0.954	8.58E-3
70	296	130	0.725	4.42E-2
90	320	56	0.423	5.63E-2
110	354	49	0.109	2.26E-2
130	349	23	-0.048	1.57E-1

However, the results were different when the doping temperature was raised above 70 °C. The regression coefficient values were much lower than a factor of 0.9. The calculated equilibrium doping level declined as the temperature increased. Therefore, the model can not be applied for the doping process at temperatures higher than 70 °C. This indicates that the assumptions for the

pseudo-first-order model are not appropriate for the doping process at higher temperatures. Under these conditions, the reaction between the available sites and H_2O has to be taken into account.

4.2.3 Pseudo-second-order rate law

During the doping process, if both H_3PO_4 and H_2O can "occupy" available sites of the ABPBI chains, the doping process can be illustrated as Fig. 4.6.

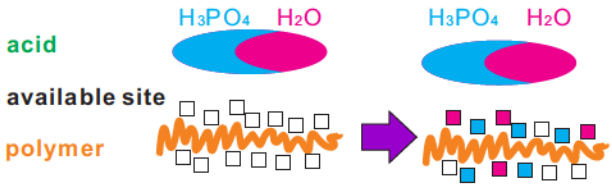

Figure 4.6: Schematic image of available site occupied by H_3PO_4 and H_2O molecules.

The occupied available sites can be distinguished as bound with H_3PO_4 and H_2O, respectively. The reaction formula is written as

$$
\begin{array}{lccccccc}
 & 2\mathrm{L} & + & \mathrm{H_3PO_4} & + & \mathrm{H_2O} & \rightleftharpoons & \mathrm{L{\cdot}H_3PO_4} + \mathrm{L{\cdot}H_2O} \\
t = 0 & [L]_T & & C_0 & & C_0' & & 0 \quad 0 \\
t = t & [L]_T \quad [L]_B & & C_0 & & C_0' & & [L]_{H_3PO_4} \quad [L]_{H_2O}
\end{array}
$$

The concentration of H_3PO_4 and H_2O in the acid bath is considered constant during the doping process, since a great volume of acid was used. The reaction can be supposed as a pseudo-second-order reaction. Therefore, the reaction rate depends on the concentration of available sites given by Eqn. 4.8 [26; 121].

$$
r = \frac{d([L]_T \quad [L]_B)}{dt} = k_2'([L]_T \quad [L]_B)^2 \tag{4.8}
$$

$[L]_{H_3PO_4}$, $[L]_{H_2O}$	wt.-%	doping level of H_3PO_4 and H_2O, $[L]_B = [L]_{H_3PO_4} + [L]_{H_2O}$
k_2	wt.-%$^{-3}$ h^{-1}	second-order rate constant
k_2'	wt.-%$^{-1}$ h^{-1}	pseudo-second-order rate constant, $k_2' = k_2 C_0 C_0'$

Rearranging of Eqn. 4.8 gives

$$
\frac{t}{[L]_B} = \frac{1}{k_2'[L]_T{}^2} + \frac{1}{[L]_T}t \tag{4.9}
$$

k_2' can be obtained from the slope of $\frac{t}{[L]_B}$ against the doping time, as shown in Fig. 4.7. The values of k_2' are listed in Tab. 4.2, as well as the equilibrium doping level and regression coefficients.

A regression coefficient of 0.833 means the model can be applied but is not really appropriate to the doping process at 25 °C. At higher temperatures, the regression coefficients are higher than 0.97. In addition, the difference between expected and calculated equilibrium doping level is less than 40 wt.-%, which is still in the deviation range of the doping level. This reveals that the model is appropriate to describe the doping process in the temperature range of 70-130 °C. The rate of the doping process is proportional to the concentration of the square of free available sites. The available sites are "consumed" by H_3PO_4 and H_2O simultaneously. Moreover, higher rate constants are obtained at higher doping temperatures. This follows the general tendency [25, p.878]. As the temperature is raised, on the one hand, the mobility of polymer molecules increases [118, pp.569-572]; on the other hand, the viscosity of phosphoric acid declines [66; 122]. Both effects are favorable for the diffusion of the acid molecules into the bulk of the membrane.

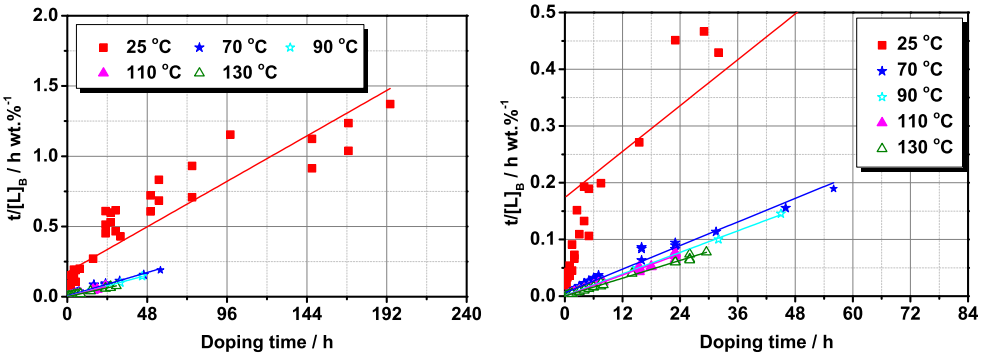

Figure 4.7: Pseudo-second-order plots of phosphoric acid adsorption on ABPBI polymer chains. The original data were obtained from Fig. 4.1. (b) is a magnification of (a) in the time range of 0 – 84 h.

Table 4.2: Fitted results obtained with pseudo-second-order rate law.

Doping temperature	Experimental equilibrium doping level (Fig. 4.7a)	Calculated equilibrium doping level ($[L]_T$)	R^2	k_2'
°C	wt.-%	wt.-%		wt.-% h^{-1}
25	163	148	0.833	2.61E-4
70	296	288	0.975	2.03E-3
90	320	316	0.999	9.22E-3
110	354	323	0.993	6.33E-2
130	349	383	0.995	2.56E-2

The pseudo-second-order model (Eqn. 4.9) also gives the initial adsorption rate, which is defined as Eqn. 4.10. The values are obtained from the reciprocal of the fitted plot interceptions in Fig. 4.7. The initial adsorption rate is plotted as a function of the doping temperature in Fig. 4.8a.

$$\textit{initial adsorption rate} = k_2'[L]_T^2 \tag{4.10}$$

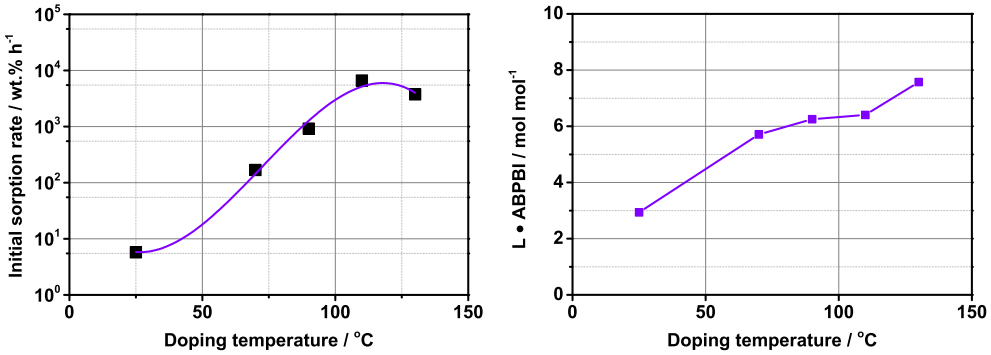

(a) (b)

Figure 4.8: (a) Initial adsorption rate of phosphoric acid adsorption on ABPBI membrane samples; (b) Amount of available site per repeat unit of ABPBI. The data was calculated based on Tab. 4.2.

The initial adsorption is accelerated as the temperature increases until 110 °C. Therefore, less time is required to reach the equilibrium at higher temperature (Fig. 4.1). The further increase of temperature results in a reduced adsorption rate. This can be explained by the dissolution of ABPBI into the phosphoric acid. In the experiment, the acid bath became yellow, the same color as the ABPBI membrane, when doping membrane at temperature above 70 °C for more than 20 h. At 130 °C the dissolution is so serious that the ABPBI samples in the acid bath were broken into pieces after 20 h.

Based on the equilibrium doping level, the amount of available sites per repeat unit can be calculated by Eqn. 4.1 and Eqn. 4.5. For calculation, the molar ratio of H_3PO_4 and H_2O in the doped membrane is supposed as 1.03:1, the same as in 85 wt.-% phosphoric acid [38]. When ABPBI is doped in 85 % phosphoric acid the concentration in the membrane is the same as in the doping bath as will be shown in Fig. 5.2. The same effect was observed for PBI [38]. Fig. 4.8b shows the amount of available sites per ABPBI repeat unit at different doping temperatures. The value is also the maximum number of acid molecules adsorbed on each repeat unit of the polymer chains. At room temperature, 3 molecules were adsorbed by each repeat unit of ABPBI polymer. In literature more than 10 molecules of H_3PO_4 and H_2O can be adsorbed by each imidazole ring for PBI membrane at room temperature [23; 38]. This indicates that the activity of ABPBI membrane investigated here is lower compared to PBI membrane in the literature. This could be associated with the macro-structure of ABPBI polymer chains.

The values of available sites increased from 3 to 7.5 when the doping temperature increased from 25 °C to 130 °C. The larger amount of available sites at higher temperature is consistent with the volume swelling of the doped membrane, as shown in Fig. 4.2. More free space between the

polymer chains due to the improved mobility of polymer chains [118, pp.569-572] are available for H_3PO_4 and H_2O at higher temperature.

4.2.4 Activation energy

Based on the pseudo-second-order rate constants (k_2') at different temperatures (Tab. 4.2), the activation energy can be calculated by Arrhenius equation [25, pp.807-809], as written in Eqn. 4.11. An Arrhenius plot has been plotted in Fig. 4.9. The rate constant obtained at 25 °C was not taken into account since the doping process fits better to the pseudo-first-order rate law. The temperature of 130 °C was also not involved because of the serious dissolution of ABPBI occurring during the doping process. The activation energy of the doping process is found as 94 kJ mol^{-1} in the temperature range from 70 °C to 110 °C.

$$ln k_2' = c \quad \frac{E_a}{R} \times \frac{1}{T} \tag{4.11}$$

E_a	kJ mol^{-1}	activation energy
R	kJ mol^{-1} K^{-1}	gas constant, 8.314 $\pm 10^{-3}$ J mol^{-1} K^{-1}
T	K	absolute temperature
c		constant in Arrhenius equation

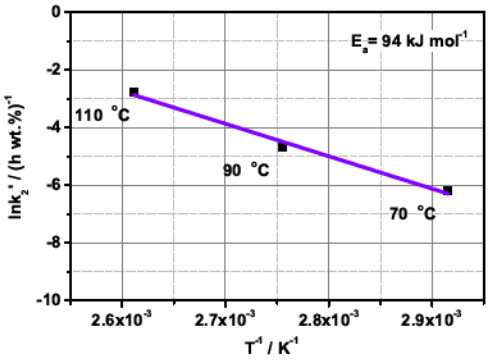

Figure 4.9: Arrhenius plot in the temperature range of 70 – 110 °C. The values of k_2' were obtained from Tab. 4.2.

4.3 Diffusion mechanism of doping process

Another task is to predict the rate-limiting step of the adsorption [29] of phosphoric acid on the polymer chains. The most common technique to identify the mechanism of the adsorption process is by fitting an intraparticle diffusion plot, which is given by Eqn. 4.12 [28].

$$Q_A = k_{id} t^{0.5} \tag{4.12}$$

Q_A	wt.-%	doping level
k_{id}	wt.-% $s^{-0.5}$	intraparticle diffusion coefficient

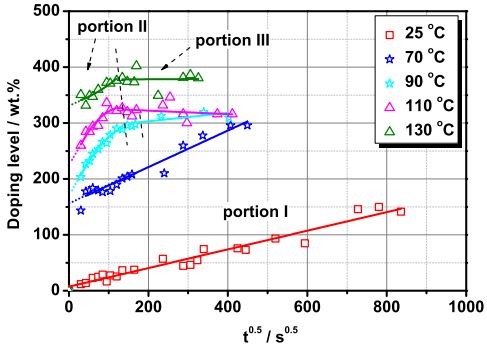

(a)

Figure 4.10: Intraparticle diffusion plots of phosphoric acid adsorption on ABPBI membrane.

Fig. 4.10 shows the intraparticle diffusion plot for doping ABPBI membrane in the temperature range from 25 °C to 130 °C. For the doping process at room temperature, the plot is linear and passes through the origin. As the first step of the adsorption [26], the molecules of phosphoric acid have to diffuse from the acid solution to the interface of ABPBI membrane. The linear plot obtained at room temperature indicates that the boundary layer diffusion is the rate-controlling step [123]. In other words, the adsorption occurs mainly at the interface between the membrane and acid solution. H_3PO_4 molecules are more active to occupy the available sites at the interface of the membrane in relation to H_2O molecules, which fits to the assumptions of the pseudo-first-order rate model.

At temperatures above 70 °C, the plots failed to pass through the origin. The positive intercept indicates a rapid external adsorption occurred within a short period of time. The latter curve portion is dominated by the acid diffusion into the bulk of the membrane. And the final plateau is considered as the saturation of the acid in the membrane. The last two portions are both determined by the intraparticle diffusion. At higher temperatures, the mobility of molecule chains [118, pp.569-572] and the viscosity of phosphoric acid [124, p.648] are promoted simultaneously. Both effects reduce the resistance of acid diffusion into the membrane bulk, for both of H_2O and H_3PO_4. The kinetics enhance in comparison to the one at room temperature. Therefore, the H_2O contribution has to be considered into the elemental reaction. From another point of view, the increased amount of acid molecules in the bulk of the membrane expanded the space between polymer chains. This agrees with the significant swelling of the membranes, as shown in Fig. 4.2.

4.4 Summary

The present chapter deals with the effect of the temperature on the ABPBI doping process in phosphoric acid. The doping process was considered as the adsorption of phosphoric acid by polymer chains. The reaction kinetic was investigated based on the content variation of phosphoric acid in ABPBI membranes. The following results were observed:

i : The content of phosphoric acid in ABPBI increased significantly at the beginning of the doping process and then slowly until approaching the equilibrium. Higher equilibrium doping levels was achieved with increasing doping temperature. Both area and thickness of membranes were expanded after doping.

ii : The rate law of the doping process was determined experimentally. A first order reaction order was found for the doping process at 25 °C. The reaction can be considered to occur between H_3PO_4 molecules and available sites of the polymer chains. Three H_3PO_4 molecules in maximum can be adsorbed by each repeat unit of ABPBI polymer at 25 °C doping temperature.

iii : In the temperature range of 70-130 °C, a second order reaction order was found for the doping process. The available sites "react" with both H_3PO_4 and H_2O simultaneously. Each repeat unit of ABPBI polymer can adsorb acid molecules up to 7.5 when the doping temperature is increased up to 130 °C. The rate constant increases with the doping temperature. The maximum initial adsorption rate occurs at 110 °C.

iv : The adsorption of phosphoric acid mainly occurs at the surface of the membrane during doping at room temperature. The acid diffusion into the bulk of the membrane is promoted at higher temperature.

v : The investigated doping process of ABPBI membranes in concentrated phosphoric acid can be regarded as an endothermic reaction. The activation energy is estimated as 94 kJ mol^{-1} in the temperature range from 70 to 110 °C.

5 Determination of Acid Doping Level II

In Chapter 4 the kinetics of doping ABPBI membranes in concentrated phosphoric acid was investigated. In this work, the attention will be focused on the chemistry of the doping process. The effect of the acid concentration on the doping process was investigated. The isotherm study was carried out by means of Scatchard method [27; 41; 42]. A series of thermodynamic parameters was estimated, *e.g.* the equilibrium constant, the change of Gibbs free energy and the equilibrium dissociation constant.

5.1 Isotherm study at room temperature

5.1.1 Doping level with different acid concentrations

Chapter 4 reveals that the process of doping membranes at room temperature needs more time to approach the equilibrium than the doping process at higher temperatures. In this work, the samples of ABPBI membrane were doped in a phosphoric acid solution at room temperature for one year. The concentration of the phosphoric acid bath was varied from 0 to 14.8 mol L^{-1}. The doping process occurred in a closed system to keep the acid concentration unchanged during the experiment.

The equilibrium acid doping level was plotted in Fig. 5.1a. The doping level increased as the concentration of the acid solution was raised. For concentration of 14.8 mol L^{-1} (85 wt.-%), the equilibrium doping level was found as 144 wt.-%. The value is in good agreement with the highest doping level obtained in the open system at room temperature for 200 h (Fig. 4.1). This means that in this case the doping process was not sensitive to the system whether open or closed, because the concentration of the acid solution in the open system probably had no obvious change up to 200 h at room temperature in the laboratory where the temperature and the relative humidity was nearly constant during the doping time.

The contents of H_3PO_4, H_2O and ABPBI were estimated separately by chemical characterization (see Section 3.1). All the calculations are performed under the assumption that the ABPBI structure is equivalent to the structure shown in Fig. 2.2b. Fig. 5.1b shows the H_3PO_4 and H_2O uptake per ABPBI repeat unit. The water uptake of the membrane increased as the concentration of acid bath was raised up to 5 molL^{-1} H_3PO_4. Further increase in the acid concentration led to a reduced water uptake. The H_3PO_4 uptake of the membrane increased rapidly with the concentration of the

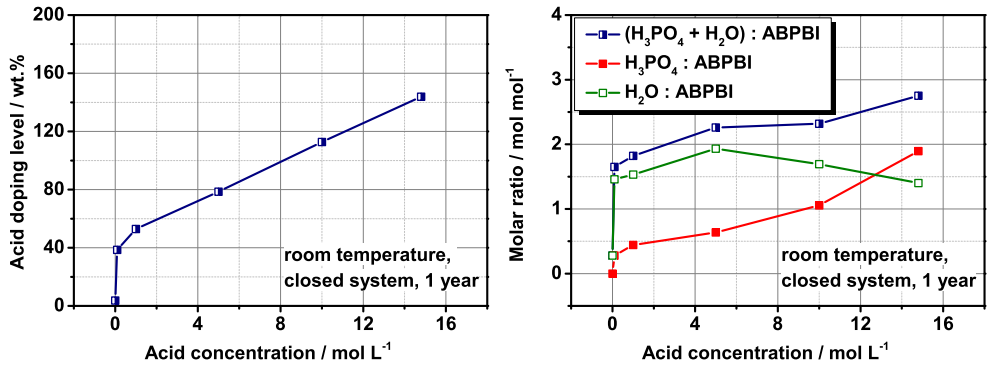

Figure 5.1: The equilibrium doping level at room temperature: (a) acid doping level calculated by Eqn. 3.1; (b) uptake of (H_3PO_4 + H_2O), H_3PO_4 and H_2O separated by element characterization. The ABPBI samples were immersed into phosphoric acid bath in closed system at room temperature for one year.

acid solution up to 1 mol L^{-1}. In the concentration range from 1 to 10 mol L^{-1}, the acid uptake rose slightly. For the acid solution of 14.8 mol L^{-1}, the H_3PO_4 uptake of ABPBI increased sharply. The variation tendency of H_3PO_4 uptake of ABPBI against the acid bath concentration is consistent with that of PBI [38]. However, the value of H_3PO_4 uptake obtained here is lower by 0.5 mol mol^{-1} than that per imidazole ring in PBI [27]. It means the investigated ABPBI has a lower affinity to react with phosphoric acid than the PBI described in the literature.

From the contents of H_3PO_4 and H_2O, the acid concentration inside the doped membrane can be calculated. The acid concentration in the doped membrane is defined as the number of moles H_3PO_4 per liter of doped membrane. Fig. 5.2 shows that the acid concentration in the membrane is higher than that in the surrounding acid solution. In other words, the acid is concentrated in the doped membrane. Moreover, the concentrating effect was also observed for PBI [38], which is attributed to the acid-base interaction between H_3PO_4 and polymer chains.

5.1.2 Scatchard plot

As suggested in Chapter 4, the doping process can be considered as the adsorption of H_3PO_4 molecules onto the ABPBI polymer chains. Here, the reaction chemistry will be investigated. The location of the ABPBI binding to the acid molecule is referred to as the coordinating site. It is believed that the reaction occurs at the imidazole group [15; 16]. The coordinating sites can be divided into several groups depending on the affinity of the reaction bond [27]. The present work focus on the coordination of H_3PO_4 and ABPBI as suggested in [27]. To clarify, the assumptions in the study are listed below:

i : There is no change in acid concentration during the doping process.

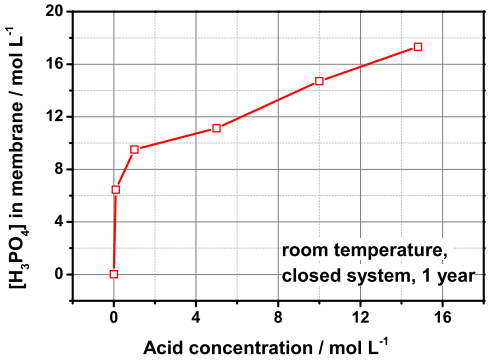

Figure 5.2: Acid concentration inside the doped membrane. The data were calculated from the data in Fig. 5.1b.

ii : The effect of water on the studied isotherm is not taken into account.

iii : The coordinating sites can be divided into *i* types.

The isotherm of doping ABPBI at the room temperature can be investigated with the Scatchard method [41; 42], which has been applied to the doping process of PBI [27]. According to the description in Section 2.2.2, $\frac{[L]_{H_3PO_4}}{C_0}$ is plotted against $[L]_{H_3PO_4}$ (Eqn. 2.10). The curve in Fig. 5.3 is so-called Scatchard plot. Two linear portions can be distinguished. This means there are two types of the coordinating sites in the ABPBI molecules. The slope and x-intercept of two linear portions are used to calculate $[L_i]_T$ and K_i, as summarized in Tab. 5.1. The calculated data are listed in Tab. 5.2.

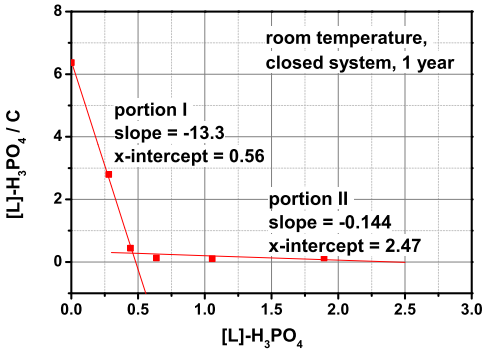

Figure 5.3: Scatchard plot for doping ABPBI membrane at room temperature. Points: experimental data obtained from Fig. 5.1b; lines: linear fitting plots.

Tab. 5.2 shows that $[L_1]_T$ is estimated as 0.5 mol mol^{-1}. It means, in total, there is 0.5 first coordinating site per imidazole ring for ABPBI. The value is the half of that per each imidazole ring for PBI [27]. In addition, the slope of this portion gives an equilibrium constant (K_1) of 13.3 L mol^{-1}. The value is close to the value of 12.7 L mol^{-1} for PBI. This indicates that there is no obvious

Table 5.1: Chemical meaning of parameters in Scatchard plot (see in Section 2.2.2).

	Symbol	Definition
x-intercept	$[L_i]_T$	maximum uptake of H_3PO_4 for *i*th type of coordinating sites
slope	K_i	equilibrium constant of adsorption at *i*th type of coordinating sites

Table 5.2: Thermodynamic parameters obtained by the Scatchard method at 25 °C.

		ABPBI		PBI [27]	
		Portion I	Portion II	Portion I	Portion II
$[L_i]_T$	mol mol^{-1}	0.5	2.5	2 *	6.6 †
K_i	L mol^{-1}	13.3	0.14	12.7	0.19
$\Omega G_i^{0,25\,°C}$	kJ mol^{-1}	-6.4	4.8	-6.3	4.11
$K_i^{a_1,25\,°C}$	mmol L^{-1}	0.52	48	0.54	36

* *1 coordinating site per imidazole ring for PBI;*
† *3.3 coordinating sites per imidazole ring for PBI.*

difference between the affinities of the acid to the imidazole ring in ABPBI and PBI. The smaller amount of this type of coordinating sites in ABPBI could be related to the macro-structure of polymer chains, which blocks the diffusion of H_3PO_4 molecules into the bulk of the ABPBI membrane (see Chapter 4).

For the second portion, the total amount of coordinating sites and equilibrium constant (K_2) are estimated as 2.5 mol mol^{-1} and 0.144 L mol^{-1}. Both values are consistent with that per each imidazole ring in PBI [27]. It means the macro-structure of ABPBI has no obvious influence on this type of adsorption. It can be supposed that the second type of coordinating sites is mainly located at the interface between membrane and the acid solution, for both ABPBI and PBI. The value of K_1 is two orders of magnitude higher than that of K_2, which indicates a stronger affinity of the first type bound than that of the second type.

As listed in Tab. 5.2, the sum of the maximum doping levels for two types of coordinating sites is 3 mol mol^{-1}for ABPBI, which is the same as the value obtained by kinetic study at room temperature in Chapter 4. The adsorbed H_3PO_4 can be separated depending on the affinity of the reaction bond. The H_3PO_4 molecules were coordinated priority at the first type sites due to the high affinity of the bond. Fig. 5.4 shows that the H_3PO_4 uptake increases rapidly as the concentration of the acid solution was raised up to 1 mol L^{-1}. Afterwards, the value rose slowly until approaching to the maximum uptake for this type of coordinating site, *e.g.* 0.5 mol mol^{-1}. The rest of H_3PO_4 uptake is contributed to the adsorption at the second type of the coordinating sites. The uptake increased significantly after the saturation of the first type site. The tendency is consistent with that observed with PBI [38].

Based on the equilibrium constants, the change of Gibbs free energy is calculated by Eqn. 5.1. The calculated results have been listed in Tab. 5.2.

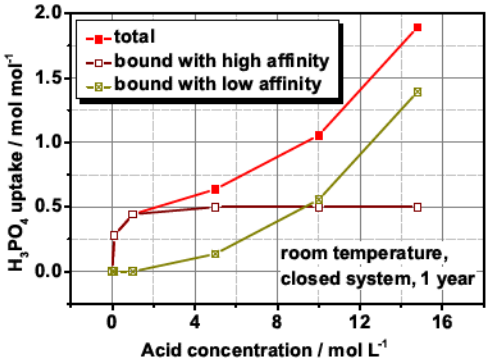

Figure 5.4: Separation of adsorbed H_3PO_4 in doped membrane. The value was obtained from Fig. 5.1b and Tab. 5.2.

$$\Omega G_i^0 = RT\ln K_i \tag{5.1}$$

The negative value of ΩG_1^0 = -6.4 kJ mol^{-1} means that H_3PO_4 molecules occupy the first type of coordinating sites spontaneously at atmospheric pressure and room temperature. However, the positive value for the second type, ΩG_2^0 = 4.8 kJmol^{-1}, indicates that the reaction is less favorable as that onto the first type. A higher concentration of the acid solution is required to promote the adsorption. From another point of view, the reverse reaction, the acid departing from the second type of coordinating site, takes place spontaneously. This fits the fact that the amount of acid in the membrane immediately started to decrease after the doped samples were taken out of the acid bath. A significant reduction of doping level occurred when the doped membrane was immersed into water or diluted acid solution.

As discussed above, the results obtained from Scatchard plots are in agreement with the isotherm study in literature [27] and the kinetic study in Chapter 4. However, it must be noted that the results were analyzed based only on 6 experimental points. In addition, the doping level has a variation range of 10 % in relative (Chapter 4). Therefore, there is an uncertainty of the fitting result due to experimental errors. This should always be taken into account, especially for the quantitative comparison.

5.1.3 Dissociation of ABPBI-H_3PO_4

In an aqueous solution, the phosphoric acid undergoes stepwise dissociation. The first step contributes most to the proton conductivity, as Eqn. 5.2 [125], since the dissociation constant for the first step is several orders of magnitude higher than the two subsequent steps [16; 27].

$$H_3PO_4 \rightleftharpoons H^+ + H_2PO_4^- \qquad K_{H_3PO_4}^{a1,25\,^\circ C} = \frac{[H^+][H_2PO_4^-]}{[H_3PO_4]} = 6.9 \pm 10^{-3}\ mol\ L^{-1} \tag{5.2}$$

The equilibrium dissociation of the complexes ABPBI-H_3PO_4 can be supposed as H_3PO_4 bound onto each type of coordinating sites in ABPBI. The same estimation has been described in [27]. The process can be easily represented as:

$$L_i \times H_3PO_4 \rightleftharpoons L_i + H^+ + H_2PO_4^- \qquad K_{i\,H_3PO_4}^{a1} = \frac{[H^+][L_i][H_2PO_4^-]}{[L_i]_{H_3PO_4}} \tag{5.3}$$

Combining Eqn. 2.4, Eqn. 5.2 and Eqn. 5.3,

$$K_i^{a_1} = \frac{K_{H_3PO_4}^{a1}}{K_i} \tag{5.4}$$

The values of $K_i^{a_1}$ are listed in Tab. 5.2 for different types of the coordinating sites. $K_1^{a_1}$ is 13 times smaller than $K_{H_3PO_4}^{a1}$, while $K_2^{a_1}$ is 7 times higher. This means the adsorbed H_3PO_4 onto the second type of the coordinating site would contribute more to the proton conductivity of the acid doped ABPBI. The comparisons of the adsorption at two types of the coordinating site are summarized in Tab. 5.3.

Table 5.3: Comparison of the H_3PO_4 molecules adsorption onto coordinating sites at room temperature.

	Type I	Type II
Maximum uptake of H_3PO_4 / mol mol^{-1}	0.5	2.5
Reaction affinity	high	low
Spontaneous reaction	yes	no
Dissociation constant	$\frac{1}{13}K_{H_3PO_4}^{a1}$	$7K_{H_3PO_4}^{a1}$

5.2 Isotherm study at 70 °C

5.2.1 Doping level with different acid concentrations

In addition to room temperature, it is interesting to investigate the thermodynamics of doping process at higher temperatures. Fig. 4.1 shows that the equilibrium of the doping process at 70 °C is approached after 15 h. Therefore, the ABPBI samples were immersed into the acid bath at 70 °C for 15 h. The concentration of the acid bath was varied from 0 to 14.8 mol L^{-1}. The system involved a reflux device to keep the concentration of phosphoric acid solution constant. The experiments were repeated three times.

The acid doping level at 70 °C was plotted as a function of acid concentration in Fig. 5.5a. The acid doping level increased slightly with the concentration of the acid bath until 12 mol L^{-1}. The value in this range is smaller than the data obtained at 25 °C. This indicates that the doping process at 70 °C did not reach the equilibrium. More time is required for doping membrane in the diluted

acid to approach the equilibrium. For the concentrated phosphoric acid (14.8 mol L^{-1}), the doping level at 70 °C reached at 230 wt.-%, which is the same as that obtained without the reflux device (Fig. 4.1).

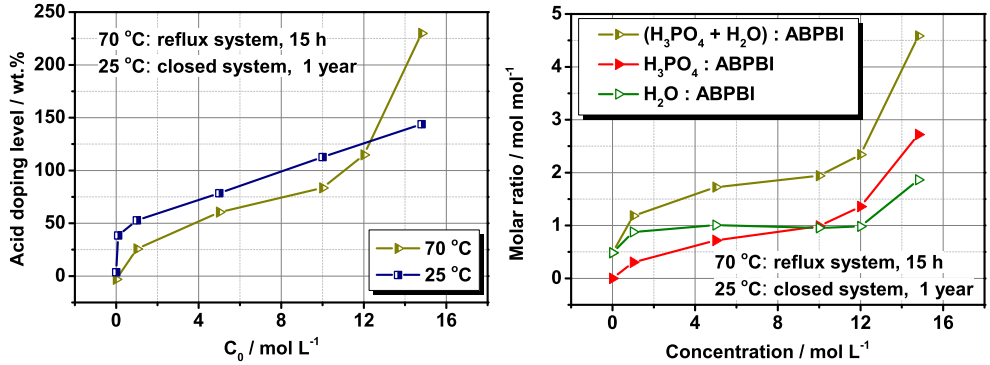

Figure 5.5: The equilibrium doping level at 70 °C as a function of the acid concentration: (a) acid doping level. The acid doping level at 25 °C from Fig. 5.1b was taken as reference. (b) uptake of (H_3PO_4 + H_2O), H_3PO_4 and H_2O separated by the vacuum heating. The ABPBI membrane samples were immersed into phosphoric acid bath in a reflux system at 70 °C for 15 h.

The contribution of H_3PO_4 and H_2O for the acid uptake was separated by heating the doped membrane in the vacuum oven. Fig. 5.5b shows that the H_3PO_4 uptake increases with the concentration of the acid bath, significantly at 14.8 mol L^{-1}. The H_2O uptake increases rapidly as the acid concentration was raised up to 1 mol L^{-1}. Afterwards, it keeps almost constant and increases sharply in the concentrated phosphoric acid bath. The variation of H_2O uptake as a function of the acid concentration is consistent with that of PBI in [38]. However, the tendency differed from that at room temperature, which is chemical characterized (Fig. 5.1b). The difference is attributed to the technical errors of quantitative characterization as described in Section 3.1. After heating in the vacuum oven, part of water still remained in the doped membranes, which were considered as the mass of H_3PO_4 in calculations. Therefore, the number of moles H_2O in the doped membrane obtained by the vacuum heating is smaller than that obtained by the chemical characterization.

5.2.2 Scatchard plot

The Scatchard method was also used in the investigation of the doping ABPBI membranes at 70 °C in the same way as that at 25 °C. The plot and related parameters are shown in Fig. 5.6 and Tab. 5.4.

For the first type of coordinating site, the maximum doping level is 1 mol mol^{-1}, which fits to the amount of imidazole rings in the repeat unit of ABPBI. This indicates that there is no limitation of

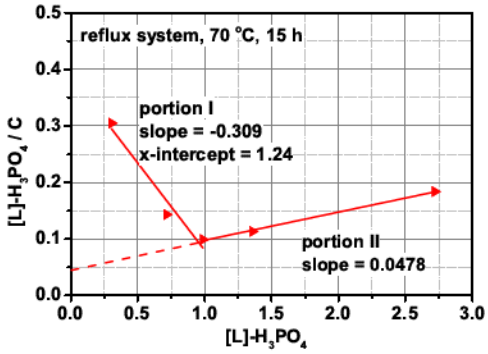

Figure 5.6: Scatchard plot for doping ABPBI membrane at 70 °C. Points: experimental data obtained from Fig. 5.5a; lines: linear fitting plots.

Table 5.4: Thermodynamic parameters obtained by the Scatchard method at 70 °C.

		ABPBI	
		Portion I	Portion II
$[L_i]_T$	mol mol^{-1}	1.24	-0.95
K_i	L mol^{-1}	0.31	-0.05
$\Omega G^{0,70\,°C}$	kJ mol^{-1}	3.36	–
$K_i^{a_1,70\,°C}$ ⋆	mmol L^{-1}	7.26	–

⋆ $K_{H_3PO_4}^{a1,70\,°C} = 2.23\,mmol\,L^{-1}$ [120].

H_3PO_4 molecules diffusion into the matrix of ABPBI molecules, which occurs at room temperature. It agrees with the opinion in Chapter 4 that the acid diffusion into the bulk of the membrane is promoted at higher temperatures. The equilibrium constant obtained at 70 °C is two orders of magnitude lower than that at 25 °C. It indicates the affinity of the first type bound decreases as the temperature increases, due to the promoted activity of molecules at higher temperature. The positive value of $\Omega G^{0,70\,°C}$ means the doping reaction can not take place spontaneously. In addition, the dissociation constant of ABPBI-H_3PO_4 is ten times higher than that at room temperature. Therefore, the complexes coordinated at this type sites contribute more on the conductivity at 70 °C in comparison to that at room temperature.

For the second portion, the negative values of $[L_2]_T$ and K_2 were obtained, as listed in Tab. 5.4. The unacceptable values of the thermodynamically parameters indicates that the coordination at the second type site can not be described by Scatchard plot at 70 °C. The kinetic study in Chapter 4 found that the doping process at 70 °C follows the pseudo-second-order rate law. The elemental reaction can be represented as the reaction among the coordinating site, H_2O and H_3PO_4. The effect of water on the studied isotherm has to be considered, which differs from the elemental reaction at room temperature. Mathematically, the Scatchard method can only be used for two types of systems [42]: (i) one type of small molecules adsorbed on the macromolecules with one to three types of binding sites, and (ii) two types of small molecules adsorbed on the

macromolecules with one type of binding sites. In the process of doping ABPBI in phosphoric acid at 70 °C, there are molecules of H_3PO_4 and H_2O, and at least two types of bounding sites for the adsorption. Therefore, the Scatchard method is not appropriate.

5.3 Summary

The present work focuses on the effect of the acid concentration on the process of doping ABPBI in phosphoric acid solution. The thermodynamic study was investigated by Scatchard method. The results were listed as following.

i : The equilibrium doping level increases as the concentration of the acid solution is raised.

ii : There are two types of coordinating sites in the ABPBI membranes which can react with H_3PO_4, one with a high affinity and the other with a lower affinity. At room temperature, the strong adsorption with the high affinity takes place spontaneously, and 0.5 H_3PO_4 molecule is adsorbed by each ABPBI repeat unit in maximum. The weaker adsorption with the lower affinity can not occur spontaneously, with 2.5 H_3PO_4 molecules per ABPBI repeat unit adsorbed in maximum.

iii : At room temperature, the dissociation constant of the ABPBI-H_3PO_4 via the strong adsorption is 13 times lower than that of aqueous phosphoric acid solution; while the one via the weaker adsorption is 7 times higher than that in aqueous, which contributes more to the proton conductivity of the doped membrane.

iv : The Scatchard method is not suitable to describe the H_3PO_4 uptake of ABPBI at 70 °C, since the influence of H_2O uptake has to be taken into account.

6 Microporous Layer of Anode and Cathode

This chapter evaluates the impact of a MPL on the properties of the GDEs and the performance of the HT-PEFCs. The experimental results show that a suitable arrangement of anodic and cathodic MPL is beneficial to improve the cell performance.

In this chapter, the experimental work was mainly performed by Sajedeh Mohajeri, and a part of the content has been included in her master thesis [126]. The microscopic images were taken with Katja Klafki. The analysis of EIS results were completed with the help of Dr. Klaus Wippermann.

6.1 Effect of MPL on physical properties of GDE

6.1.1 Structure and morphology

Two commercial GDLs were investigated in the present work, H2315 CX165 and H2315. The H2315 CX165 consists of a layer of carbon fibre matrix and a MPL, while H2315 has the same carbon fibre matrix as H2315, excluding the MPL. The thickness and area weight of the samples were measured and are listed in Tab. 6.1. The thickness difference between the two GDLs is attributed to the inclusion of the MPL with an approximate thickness of 40 µm.

Table 6.1: Physical parameters of two GDLs purchased from Freudenberg FCCT KG.

	H2315 CX165	H2315
Carbon fibres	non-woven	non-woven
MPL	with	without
Thickness / µm	245 $\otimes$ 4	203 $\otimes$ 3
Area weight / mg cm^{-2}	13.3 $\otimes$ 0.2	9.8 $\otimes$ 0.1

The morphology of the GDL was characterized by microscopic images. In the top-view image, Fig. 6.1a, H2315 CX165 is homogeneous and dense due to the MPL on the top of it. In Fig. 6.1c a double layer consisting of a dense top layer and a porous bottom-layer can be identified clearly. In the bottom layer, the white spots are the cross-sectional view of the carbon fibres and the rest volume are free space between fibres. The matrix of the carbon fibres are the same for H2315, Fig. 6.1b for the top-view image and Fig. 6.1d for the cross-sectional view. The dense top layer in

Fig. 6.1c is attributed to the MPL. A part of the MPL penetrates into the matrix of carbon fibres. As can be seen in Fig. 6.1, the thicknesses of the two GDLs are 260 µm and 230 µm, which are higher by 15 – 25 µm than the ones listed in Tab. 6.1, because the values of thicknesses as in Tab. 6.1 were measured under force as described in Section 3.2.1.

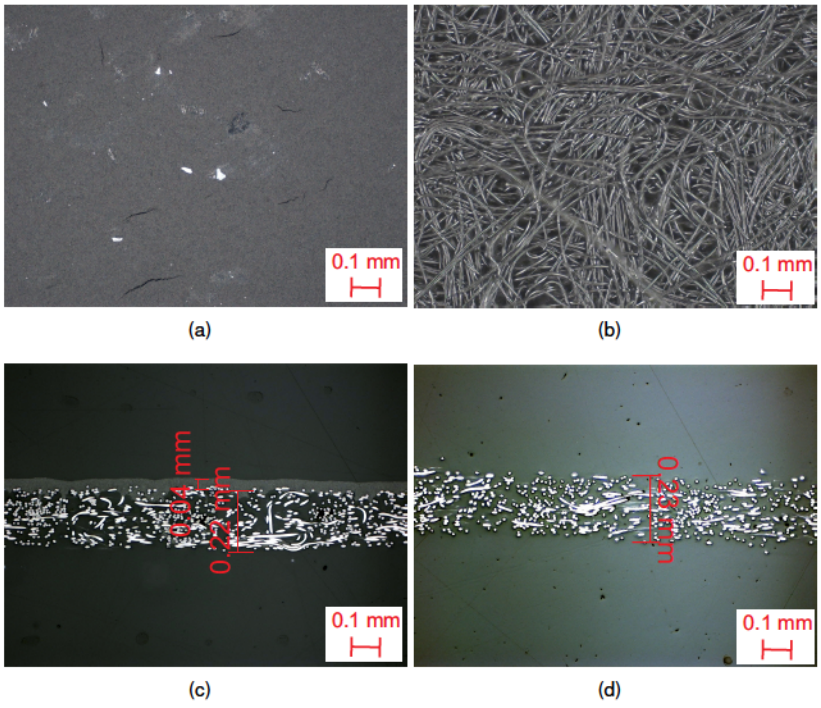

Figure 6.1: Morphologies of GDLs: (a) top- and (c) cross-sectional view of H2315 CX165 (with MPL); (b) and (d) for H2315 (without MPL).

Catalyst layers were deposited on top of the two GDLs with the same procedure as described in Section 3.2.1. Fig. 6.2a and Fig. 6.2b show the top-view of the final catalyst layers with a platinum loading of $1.0 \otimes 0.1\,\mathrm{mg\,cm^{-2}}$. The catalyst layer shows blocks divided by cracks, which is an often observed morphology of catalyst layers [22; 59]. Since the surfaces of the GDLs are visible in the cracks (Fig. 6.2b), the cracks extend through the entire catalyst layer thickness.

The widths of 30 cracks were measured from the top-view images in Fig. 6.2. The Histograms of the crack width have been plotted in Fig. 6.3. The crack width of the catalyst layer with MPL scatters in the ranges of 10 – 40 µm and 50 – 70 µm, with a mean value of $36 \otimes 18$ µm. For the catalyst layer without MPL, the crack widths locates in the ranges of 30 – 40 µm and 50 – 70 µm, with a mean value of $47 \otimes 17$ µm. Therefore, the presence of the MPL causes a reduction of the crack width in general. The form of the cracks could be attributed to the evaporation of solvent in the catalyst slurry during the catalyst layer deposition. The wider cracks in the absence of a MPL denote the faster removal of solvent from the catalyst slurry.

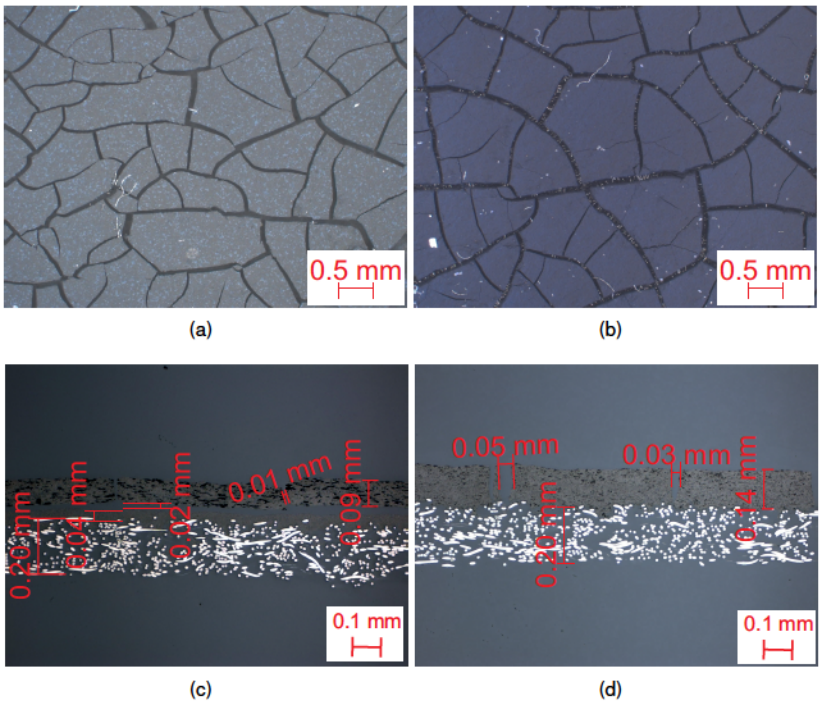

Figure 6.2: Morphologies of GDEs: (a) top- and (c) cross-sectional view for the one with H2315 CX165 (with MPL); (b) and (d) for the one with H2315 (without MPL) (reorganized from [126, Fig.4.2 and 4.3]). The Pt loading is $1.0 \otimes 0.1$ mg cm^{-2} for both samples.

Fig. 6.2c shows the cross-sectional view of the GDE including MPL. Compared to Fig. 6.1c, a well defined catalyst layer is deposited on top of the GDL. The black spots are recognized as unmelt PTFE which has low electronic conductivity. In addition, there is a gap visible at the interface of the catalyst layer and MPL, estimated as 20 µm. Hizir *et al.* attributes the formation of these interfacial gaps to the rough surface characteristics of the catalyst layer and MPL [59]. The interfacial gaps weaken the adhesion between catalyst layer and GDL [59]. In the experiment, the catalyst layer blocks are peeling away from the GDL with a MPL much easier than for the MPL free GDE. The phenomena differs from the catalyst layer which are air-sprayed onto the carbon paper [45], in which the presence of MPL improves the adhesion between the catalyst layer and the GDL.

For the GDE without a MPL, as shown in Fig. 6.2d, there is no distinguished interface between the catalyst layer and the GDL. Comparing Fig. 6.1d and Fig. 6.2d, the measured thickness of the GDL is reduced by 30 µm after the deposition of the catalyst layer. Considering the deviation of the GDL thickness around 3 µm (Tab. 6.1), the thinner GDL in the cross-sectional image is due to a part of GDL covered by the catalyst layer. In other words, a part of the catalyst slurry penetrates into the matrix of the carbon fibres, in the same way as the MPL does [58, p.21]. The penetration of the catalyst layer also explains the difference of catalyst layer thickness as in the cross-sectional images (Fig. 6.2). The thickness is estimated as 90 µm for the catalyst layer with MPL and 140 µm

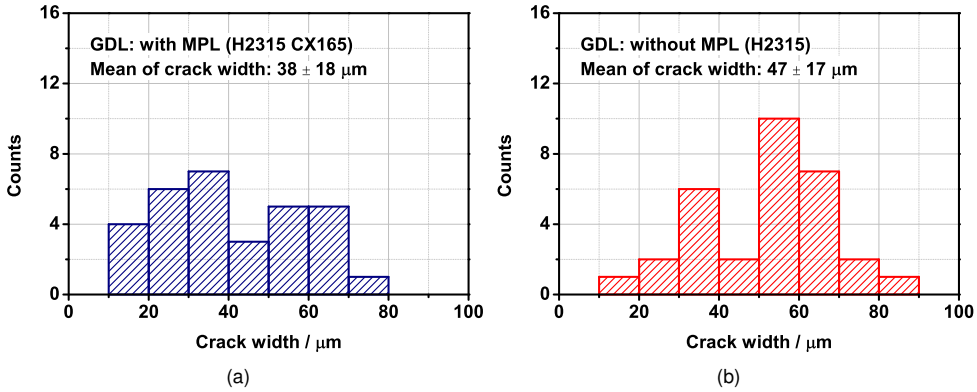

Figure 6.3: Histograms of the crack width of the catalyst layer deposited on top of (a) H2315 CX165 (with MPL) and (b) H2315 (without MPL). The crack widths were measured on Fig. 6.2a and Fig. 6.2b.

for the one without MPL, although they were deposited with the same platinum loading in average.

6.1.2 Catalyst loading gradient

The catalyst layer of the GDE was deposited with a fixed speed by means of the doctor blade technique, as illustrated in Fig. 3.4. After drying, the GDE was cut into pieces to detect the catalyst loading gradient along the coating direction (Fig. 3.4). The catalyst layer thickness and the platinum loading of each piece were plotted against the position in x direction, where x is the direction of coating (see in Fig. 6.4). The experiments have been repeated three times.

There is a clear tendency that the thickness of the catalyst layer and the catalyst loading decrease along the coating direction. The gradient is more pronounced and scatted for the MPL free GDE. In addition, the average thickness and Pt loading are both higher for the GDE without MPL in relation to the one with MPL. During the deposition, as illustrated in Fig. 3.2b, the weight of the catalyst slurry in the blade decreases along the coating direction. This reduces the force on the catalyst slurry attached to the GDL, which decreases the weight of the catalyst slurry deposited on the GDL. Therefore, a gradient of the catalyst weight and catalyst loading is observed along the coating direction. The gradient becomes obvious for the MPL free GDE, since the penetration of catalyst slurry into GDL (Fig. 6.2d) declines with the weight of catalyst slurry in the blade. In addition, the solvent in the slurry can easier infiltrate through the GDL in the absence of the MPL. The accelerated solvent removal results in the thicker catalyst with wider cracks (Fig. 6.2).

The catalyst layer thickness of GDEs without MPL has to be reduced to 100 µm in order to reach the same catalyst loading as that of the GDEs with MPL. It is achieved by decreasing the thickness of the spacer during the preparation of the catalyst layer.

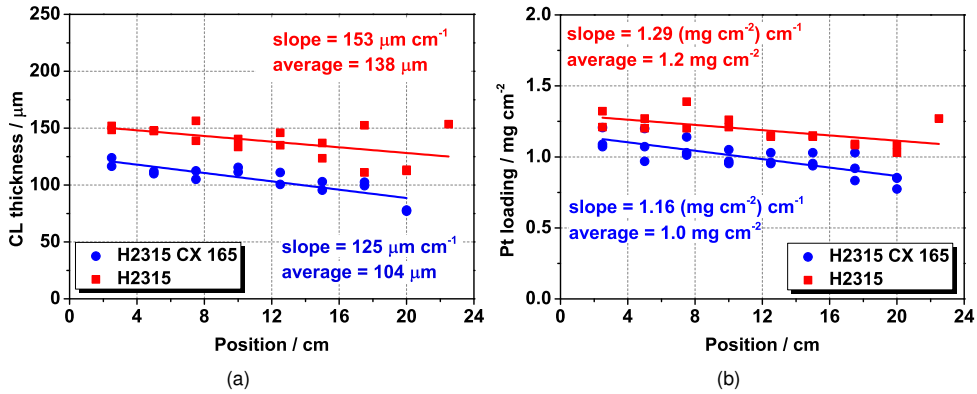

Figure 6.4: (a) Thickness and (b) Pt loading gradient of catalyst layers prepared on top of H2315 CX165 (with MPL) and H2315 (without MPL).

6.1.3 Air permeability

As a porous material, the gas permeability is one of the most important properties of the GDE [8, p.15]. In the present work, the air permeability is calculated by Eqn. 3.3, based on the Gurley number. The Gurley number is expressed as the time required passing a certain volume of flow through the gas diffusion media in the through-plane direction [8, p.15].

Tab. 6.2 lists the air permeabilities of the GDL and the GDE samples. It shows that the air permeability of the GDL with MPL is two orders of magnitude higher than that without MPL. This reveals that the air permeability of the GDL is dominated by the MPL [58, p.29]. The deposition of the catalyst layer has no clear influence on the permeability in the presence of a MPL. However, it reduces the air permeability to about 50 % in the absence of a MPL, since the macropores of GDL are partly closed by the catalyst layer. The impact of the catalyst layer on the air permeability is much weaker than that of MPL due to the macro-cracks in the catalyst layer, comparing Fig. 6.1 and Fig. 6.2.

Table 6.2: Air permeability (through-plane, / μm (Pa s)$^{-1}$) of GDL and GDE at 1 atm..

	GDL	GDE
H2315 CX165 (with MPL)	10.1 ⊗ 2.5	12.1 ⊗ 2.4
H2315 (without MPL)	1748 ⊗ 56	985 ⊗ 94

6.2 Effect of MPL on electrochemical performance of HT-PEFCs

A series of electrochemical experiments was carried out to determine the effect of anodic and cathodic MPLs on the performance of HT-PEFCs. A two-level factorial plan was designed and is

visualized in Fig. 6.5. There are four cells involved in the present study. The cell with inclusion of the MPL for both anode and cathode was taken as the reference.

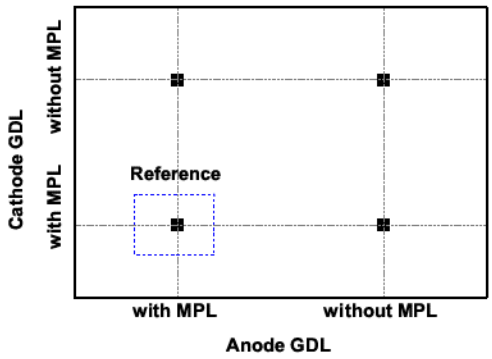

Figure 6.5: Experimental design to investigate the effect of MPL on performances of HT-PEFCs (redrawn from [126, Fig.4.1]).

6.2.1 Polarization curves

After the break-in process, polarization curves were recorded for each cell under $\lambda_{H_2/air}$ = 2/2, as shown in Fig. 6.6. The voltages of the three modified cells are in the same level, which are all higher than that of the reference cell in almost the whole current density range.

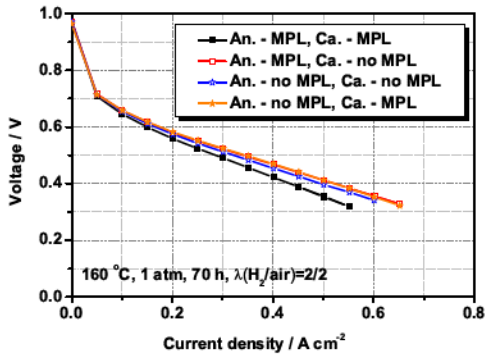

Figure 6.6: Polarization curves of the cells with different GDLs under $\lambda_{H_2/air}$ = 2/2 (redrawn from [126, Fig.4.9]). The cells were operated at ambient pressure and 160 °C after a break-in process of 70 h.

Subsequently, polarization curves were also recorded under different cathode stoichiometries. The voltages at 200 mA cm^{-2} and the slopes in the range of 0.3 – 0.6 V were collected and are compared in Fig. 6.7. In general, the voltage increases and the slope decreases when the cathode stoichiometry is raised. The voltages of the four cells present a tendency as follow: only with anodic MPL ↑ only with cathodic MPL ⩾ without any MPL > with MPL for both sides (*e.g.* the

reference cell). The tendency is independent of the cathode stoichiometry. This differs from the conclusion observed by Lobato *et al.* [58, pp.34-36] that the absence of a MPL at one side reduces the voltage of the HT-PEFC. The conflict may be associated with the different composition in the catalyst layer. Although the same catalyst powder was used, the catalyst loading is 1.0 mg cm^{-2} in this work and 0.5 mg cm^{-2} in their study. In addition, 3.3 mg cm^{-2} of PTFE was used as the binder here, while 0.5 mg cm^{-2} of PBI powder was introduced in their GDEs as the ionomer. The different catalyst layers make it difficult to compare the effects of MPLs from different groups.

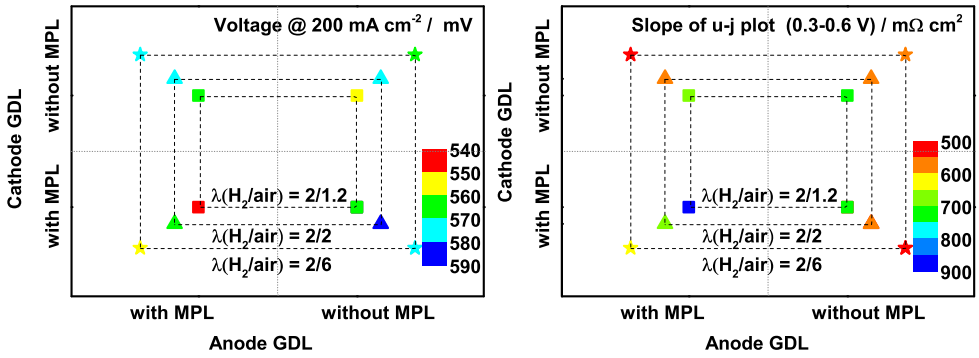

Figure 6.7: (a) Voltage at 200 mA cm^{-2} and (b) slope of polarization curves in the range of 0.3 – 0.6 V. All data were obtained with polarization curves recorded at ambient pressure and 160 °C after the cell operation of 70 h.

6.2.2 Resistances

EIS was performed on the different cells to determine and quantify the resistances. The recorded Nyquist plots were further analyzed by the equivalent circuit with the classical transmission line model [67; 111; 116; 117], as shown in Fig. 3.6. A series of resistances have been obtained for the varied cells, the ohmic, kinetic and mass transport resistances. The obtained ohmic resistances are plotted in Fig. 6.8a at 200 mA cm^{-2} and Fig. 6.8b at 400 mA cm^{-2}. The data for the cell with MPL for both sides under $\lambda_{H_2/air}$ = 2/1.2 was missing, since the cell voltage was not stable during the recording of Nyquist plots.

Two tendencies of ohmic resistance are observed in Fig. 6.8:

- I : When the cathodic stoichiometry is reduced or the current density is raised, the ohmic resistance decreases independent of the modification on the MEA.
- II : At the same cathodic stoichiometry, ohmic resistance present a tendency as: only with anodic MPL $\leqslant$ only with cathodic MPL $<$ without any MPL $\leqslant$ with MPL for both sides. This agrees with the result observed from the polarization curves (Fig. 6.7).

The first tendency follows the general behavior of phosphoric acid in the HT-PEFC. The water

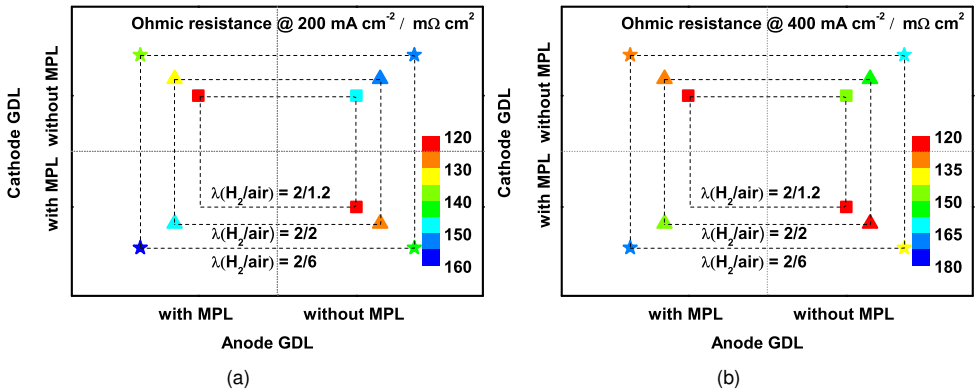

Figure 6.8: Ohmic resistances at (a) 200 mA cm^{-2} and (b) 400 mA cm^{-2}. The data were obtained by analyzing Nyquist plots with the equivalent circuit model as shown in Fig. 3.6. The Nyquist plots were recorded with amplitude of 5 mV in a frequency range of 100 kHz – 100 mHz. The cells were operated at ambient pressure and 160 °C for 140 h.

removal from the electrode to the outlet is hindered by reducing the flow rate, which will increase the water content in the MEA. The water content in the MEA can also be improved by raising the current density [70; 127]. The higher water content leads to a dilution of the phosphoric acid, which increases the proton conductivity of the membrane [61; 65; 66].

The second tendency needs more analysis. The ohmic resistances of the reference cell were recorded for 10 times with different identical MEAs, as shown in Fig. A10. The plot in black is in the mean range of all plots (Fig. A10), which is used to evaluate the effect of MPL as shown in Fig. A11. The intercept at the real axis in the high frequency range is known as the ohmic resistance [117]. The variation of the intercepts in Fig. A11 follows the second tendency. Therefore, the tendencies of ohmic resistance obtained here is reproducible.

As shown in Fig. 6.9, the mass transport resistances are determined mainly by the cathode stoichiometries. There is no clear dependence on the presence/absence of the MPL at 200 mA cm^{-2}, see Fig. 6.9a. The same observation was also found for the kinetic resistance (not shown here). While at 400 mA cm^{-2}, Fig. 6.9b, the mass transport resistances are smaller for the cell without cathodic MPL in comparison to the one with cathodic MPL under the cathodic stoichiometries of 1.2 and 2.

6.2.3 Water collection

In the HT-PEFC, water is produced at the cathode and transferred through the membrane to the anode [3]. The produced water was collected at the outlet of the anode and the cathode during cell operation. The mass ratio of the water collected at the anode to the total water collection is referred to as the water anode ratio (w) as described in Eqn. 3.7. The ratio is used to characterize the transport of water in the MEA.

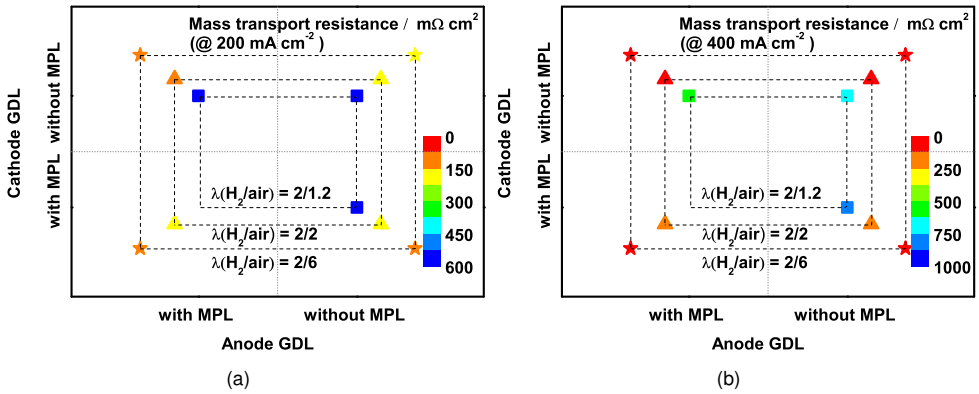

Figure 6.9: Mass transport resistances at (a) 200 mA cm^{-2} and (b) 400 mA cm^{-2}. The data obtained in the same way as those in Fig. 6.8.

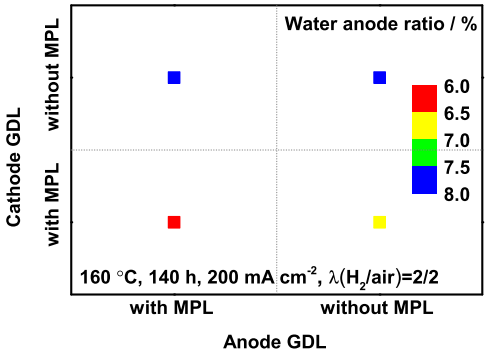

Figure 6.10: Water anode ratio of cells with different GDLs (redrawn from [126, Fig.4.16]). The cells were operated at ambient pressure and 160 °C for 140 h, at 200 mA cm^{-2} under $\lambda_{H_2/air}$ = 2/2. The temperature of the outlet condenser was set as 7 °C.

The variation of *w* is visualized in Fig. 6.10. The *w* of the cell without the cathodic MPL is higher than the one with the cathodic MPL. Since the overall water collection is constant for all cells, it means less water was collected from the cathode at the absence of the cathodic MPL.

6.2.4 Discussion

A series of cells were operated to evaluate the effect of MPLs on the cell performance. To clarify, the modified cells can be divided into three sets (Fig. 6.11). The experimental results are summarized as following. If not stated otherwise, all results are compared to the reference cell, which is assembled with a MPL at both electrodes.

I : **The cells with absence of MPL at least one side.** This set contains all other collec-

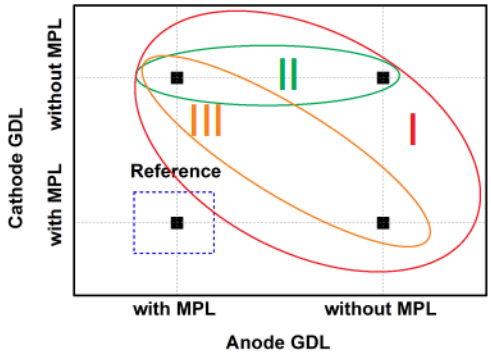

Figure 6.11: Schematic set of modified cells as designed in Fig. 6.5.

tions as subsets. The voltage is higher at 200 mA cm^{-2}; the slopes of the polarization curves are smaller.

II : **The cells with the MPL free cathode.** The mass transport resistance is smaller at 400 mA cm^{-2} under λ_{air} = 1.2 and 2. The water anode ratio is higher.

III : **The asymmetric cells, e.g. only with MPL for one side.** The ohmic resistances are smaller than those of the symmetric cells independently of the current density and the cathode stoichiometries.

In the absence of a MPL, the gas permeability of the GDE is improved (Tab. 6.2). Therefore, the O_2 supply in the catalyst layer is improved without cathodic MPL [58, p.34]. This reduces the mass transport resistance especially at higher current density or smaller cathodic stoichiometry Fig. 6.9.

Likewise, the water vapor departing from the cathode to the outlet should also be improved in the absence of the cathodic MPL, which results in an increased water collection at the cathode. However, the inference is contrary to the experimental results. As shown in Fig. 6.10, the w is higher for the cell with the MPL free cathode. In other words, the water removal is hindered in the absence of the MPL. It indicates the diffusion process is not the limited step of the water removal. In the absence of the MPL, the acid can enrich as droplets in the cracks of the catalyst layer and macro-pores in carbon-fiber matrix, in the similar way as water droplets in PEFC [64; 128–130]. This will reduce the area of the interface between acid solution and the gas flow, and hinder the water evaporation. The effect agrees with the conclusion from the PEFC that the MPL is efficient to remove water from the catalyst layer [8, p.9].

Moreover, the lowest ohmic resistances are obtained for the asymmetric cells which consist of MPL only for one side, as shown in Fig. 6.8. This means the proton conductivity of the membrane is highest in this case. The proton conductivity of the ABPBI membrane is modified with the content and composition of phosphoric acid in the membrane. In other words, the MPL influences the distribution and the concentration of phosphoric acid in the membrane. To identify this effect, more techniques would be required, like the in-situ synchrotron X-ray radiography [70; 98; 111; 127; 131] and *in-situ* Raman spectroscopy [108].

Nevertheless, the reduced ohmic and mass transport resistances of the modified cells agree with the increased voltages and reduced slope of the polarization curves. In other words, the absence of one MPL is beneficial to the cell performance.

6.3 Summary

Based on the experimental characterization and discussion, effects and properties of MPL can be summed up as follow:

I : The presence of MPL avoids the catalyst penetration into the matrix of carbon fibres during the deposition of the catalyst layer.

II : The MPL leads to a weak attachment between the catalyst layer and GDL when the doctor blade technique is used to coat the catalyst layer. In addition, the cracks in the catalyst layer become smaller with the inclusion of the MPL.

III : The gas permeabilities of the GDLs and GDEs are reduced significantly when the MPL are involved.

IV : The performance of HT-PEFC is promoted when a MPL is used only at one side.

7 Anode Thickness

As discussed in Chapter 6, the absence of a MPL at one side of the MEA is beneficial to the performance of a HT-PEFC. However, it should be noted that the overall thickness of the GDE without MPL is lower than the one with MPL. Therefore, which is the significant factor, the thickness or the absence of MPL? In addition, the thickness of the catalyst layer is as high as 125 µm in Chapter 6. How will the cell performances be changed if the thickness of the catalyst layer is reduced? This chapter will focus on these two issues. In order to simplify the investigation, the variation of GDEs only occurred at the anode.

The experimental work was mainly performed by Sajedeh Mohajeri, and the description of the experimental procedure and part of the results has been included in her master thesis [126]. The microscopic images were taken with Katja Klafki.

7.1 Effect of catalyst layer thickness on physical properties of GDE

Two commercial GDLs were used in the present work, H2315-CX165 and H2315, which have been investigated in Chapter 6. H2315-CX165 contains the same carbon fibre support as H2315, while a MPL was incorporated only on top of H2315-CX165. The catalyst layers were deposited on top of the GDLs with different thicknesses in the range of 15 to 125 µm for H2315-CX165 and of 60 to 125 µm for H2315. A raised catalyst layer thickness (θ_{CL}) leads to an increase in the GDE thickness and the platinum loading, as shown in Fig. 7.1. To reach the same GDE thickness as a GDE with MPL, the ones without MPL were deposited with a 40 µm thicker catalyst layer, since the thickness of the MPL is about 40 µm.

7.1.1 Morphology

Fig. 7.2 shows the top-view morphologies of the GDEs with different θ_{CL} in the absence and presence of a MPL. The catalyst layers were divided into blocks by the appearance of cracks. The widths of 30 cracks were measured for each image. The distributions of the crack width are plotted as Histograms in Fig. 7.3. The majority class of the crack widths shifts to a higher value with increasing thickness of the catalyst layer, independent of the presence of a MPL. With the same thickness of the catalyst layer, the majority class of the crack width is larger for the GDE without MPL in comparison to the one with MPL, see Fig. 7.3-(a) and Fig. 7.3-(e), Fig. 7.3-(c) and

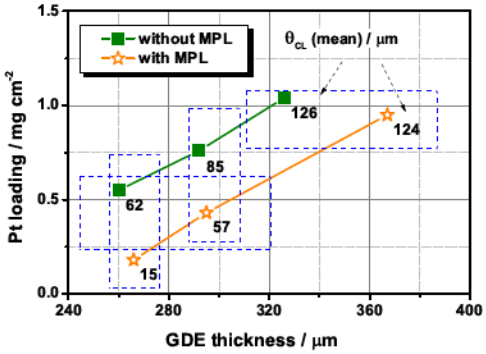

Figure 7.1: Platinum loading as a function of the GDE thickness.

Fig. 7.3-(f). When the thickness of the catalyst layer on a GDL with MPL was reduced to 15 µm, no obvious crack was found in the catalyst layer as shown in Fig. 7.3-(d).

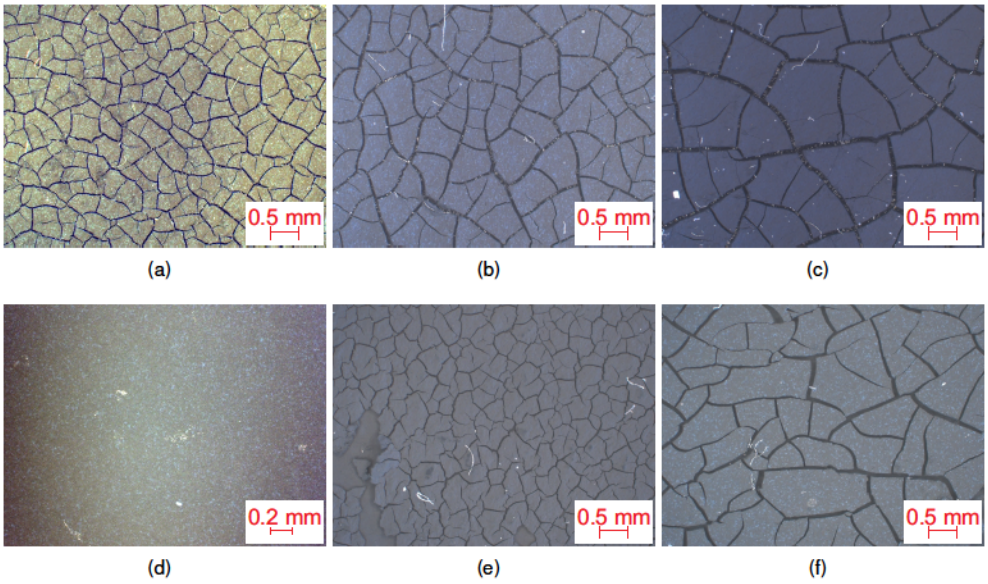

Figure 7.2: Top-view morphologies of GDEs as shown in Fig. 7.1 (reorganized from [126, Fig.5.2 and 5.3]). θ_{CL} of GDEs without MPL: (a) 62 µm, (b) 85 µm and (c) 126 µm; and the ones with MPL: (d) 15 µm, (e) 57 µm and (f) 124 µm.

7.1.2 Air permeability

The air permeability of these GDEs was also examined, as shown in Fig. 7.4. The variation of the catalyst layer thickness presents no obvious impact on the gas permeability in the presence of the MPL, since the dominant factor is the MPL [58, p.33]. For the MPL free GDEs, the air permeability

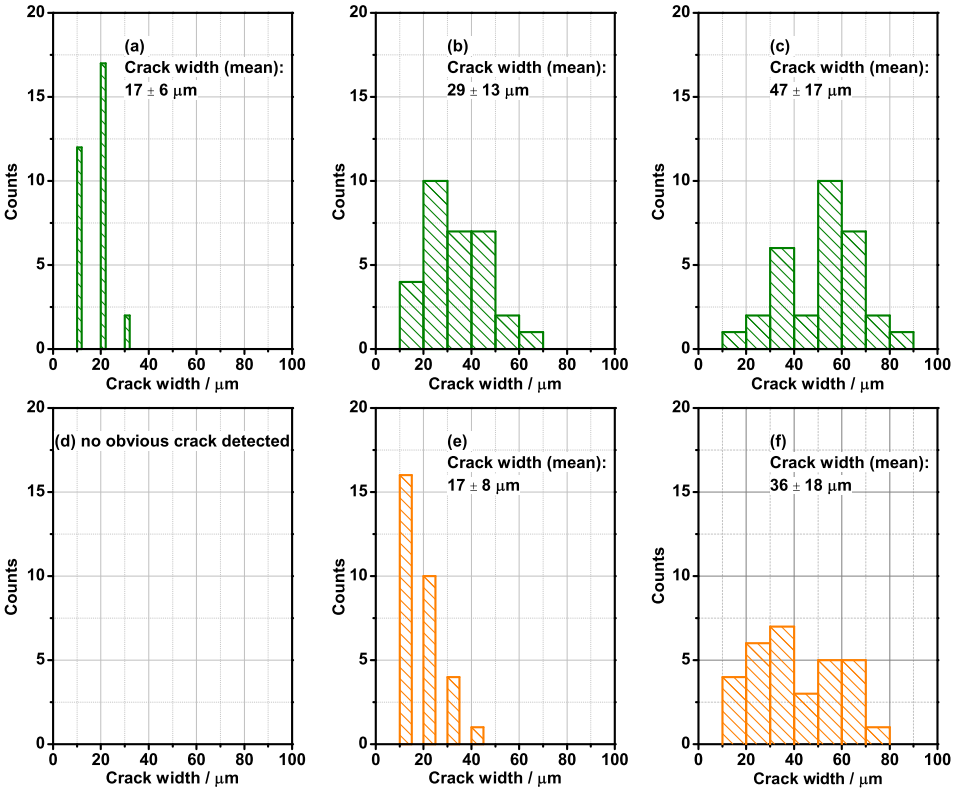

Figure 7.3: Histograms of the cracks width of the catalyst layer. The crack widths were measured in Fig. 7.2, 30 points for the single images.

declines with the reduction of θ_{CL}. This is attributed to the crack structure in the catalyst layer. The narrower crack in the thinner GDE hinders the pathway of air flow through the GDEs.

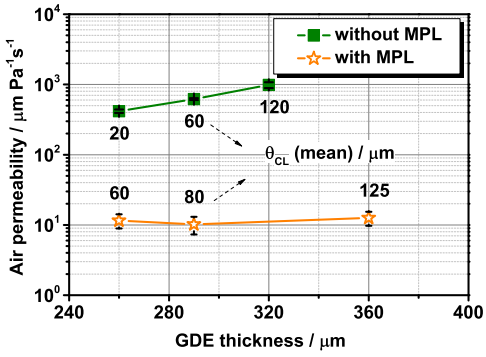

Figure 7.4: Air permeability as a function of the GDE thickness. The data are mean values of three samples for each condition. The error bars are standard deviation in absolute.

7.2 Effect of catalyst layer thickness on performance of HT-PEFC

Six different electrodes as presented in Fig. 7.2 were used as anodes for HT-PEFCs. The cathodes and the cells were prepared and operated in the same way as the standard cell, as described in Chapter 3.

7.2.1 Polarization curves

The polarization curves were recorded after the break-in process. Fig. 7.5 shows the polarization curves of cells with the different anodes. The voltage at 200 mA cm^{-2} and the slope of polarization curves were collected to compare the cell performance. As shown in Fig. 7.6a, the voltage at 200 mA cm^{-2} increases by 40 mV when the thickness of the anodic catalyst layer ($\theta_{CL,An.}$) is decreased from 124 µm to 15 µm in the presence of the MPL. It seems that the reduction of the anode thickness is beneficial to the performance of HT-PEFC. At the same thickness of the anode, at 200 mA cm^{-2}, the voltage of the cell with anodic MPL is higher by 50 mV than that of the ones without anodic MPL. Therefore, the presence of MPL improves the cell performance at least when the thickness of the anode is lower than 90 µm. The opposite effects obtained in Chapter 6 are only valid for the thicker catalyst layer at the anode, for instance 120 µm.

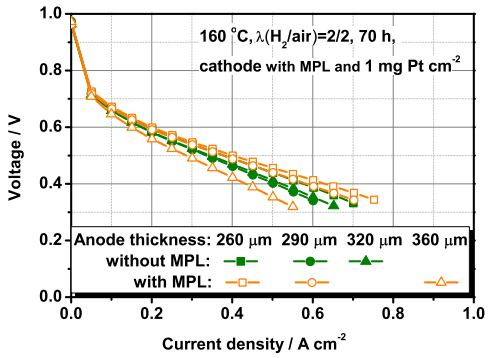

Figure 7.5: Polarization curves of the cells with different anode thicknesses (redrawn from [126, Fig.5.10]). The curves were recorded at 160 °C with $\lambda_{H_2/air}$ = 2/2 after a break-in process of 70 h. The cathode contained a MPL and a platinum loading of 0.94 ⊗ 0.05 mg cm^{-2}, and the uptake of the phosphoric acid was 15 ⊗ 1 mg cm^{-2}.

Fig. 7.6b shows the polarization curve slope are varied in the same way as the voltage in the presence of the anodic MPL. The cell without the anodic MPL does not present a clear tendency. To be aware of the HOR kinetic at a low level of the anode catalyst loading, the Nyquist plots were recorded with λ_{H_2} of 2 and 6. Fig. A12 shows that, with an anodic catalyst loading of 0.15 mgcm^{-2}, the kinetic resistance became even higher at a higher flow rate of H_2. It means the decreased anode catalyst loading has no negative influence on the HOR kinetic, at least in the range studied. The increased kinetic resistance is attributed to the drying effect at a high flow rate, which will be further discussed in Chapter 8.

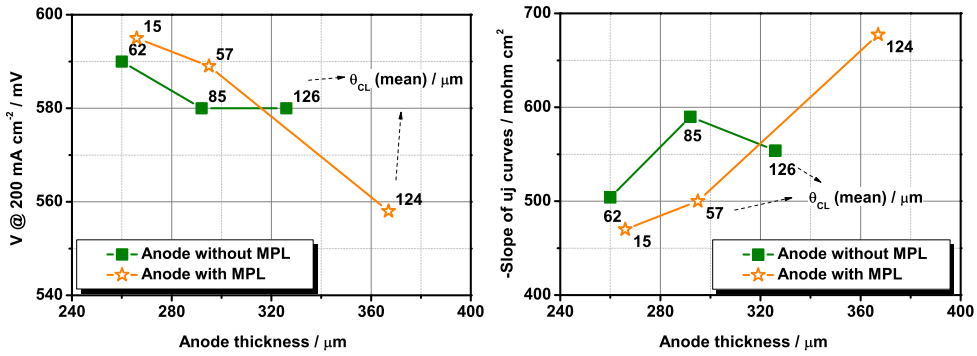

Figure 7.6: (a) Voltage at 200 mA cm^{-2} and (b) slope of polarization curves in the range of 0.3 – 0.6 V as a function of the anode thickness. All data were obtained from Fig. 7.5.

7.2.2 Water collection

The water production was collected during the operation. The mass ratio of the anodic water collection to the total collection gives the water anode ratio, which can be used to characterize the water transport in the cell. As shown in Fig. 7.7, the water anode ratio increases as the anode thickness is reduced in the presence of the anodic MPL. This means more water was collected from the thinner anodic catalyst layer. In addition, at the same thickness of the anode, the water anode ratio is higher for the cell with the anodic MPL in comparison to the one without anodic MPL. Therefore, with the same thickness, the MPL is more efficient than the catalyst layer to remove the water vapor from the anode to the outlet. In other words, the presence of the MPL improves the water removal from the anode.

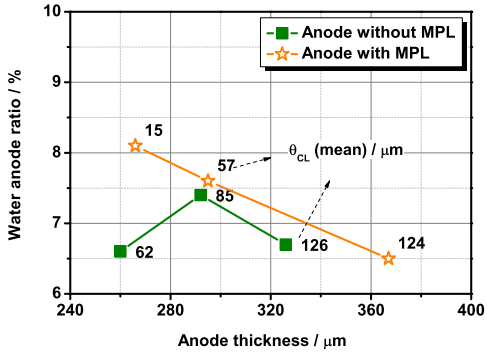

Figure 7.7: Water anode ratio of HT-PEFCs with different anodic thicknesses. The cells were operated at 200 mA cm^{-2} with $\lambda_{H_2/air}$ = 2/2. The temperature of the water condenser was set at 7 °C.

7.3 Discussion

The GDE thickness and the platinum loading both decrease as θ_{CL} is reduced (Fig. 7.1). Meanwhile, the cracks in the catalyst layer become narrower with a reduction of θ_{CL} (Fig. 7.3). This hinders the pathway of the air flow through the GDEs (Fig. 7.4), and results in the smaller gas permeabilities of the GDEs samples. In the assembled MEA, phosphoric acid transports into the cracks prior due to the hydrophobic nature of the catalyst layer [60, pp.893-898]. The shrank cracks force the acid into the catalyst blocks. It enhances the contact area of the liquid and the gas flow in the anode, which improves the water evaporation. In addition, the thinner catalyst layer improves the water removal by reducing the transport distance. Combining all these effects, the higher content of water was collected from the thinner anodic catalyst layer, as shown in Fig. 7.7. On the other side, the increased water collection at the anode indicates a higher content of water in the MEA. It leads to a dilution of the phosphoric acid [66; 127], which improves cell performances (Fig. 7.5 and Fig. 7.6) due to the enhanced proton conductivity of the membrane [61; 65; 70] and the oxygen transport through the electrolyte [67; 69].

In the absence of the MPL, some parts of catalyst penetrate into the matrix of the carbon fibres (Chapter 6). There is no limit for the acid distribution in the MEA, and thus more acid would enrich in the matrix of carbon fibres in GDL. This might increase the content of acid leaching from the catalyst layer and the membrane, which would be harmful to the performance of HT-PEFC [10; 20; 71]. As mentioned, the acid distribution and water vapor transport in the GDE are modified with the thickness and crack structure of catalyst layer. However, there is no simple rule observed from the experimental results when the θ_{CL} is reduced for the cells with MPL free anode.

In brief, the thinner anode is beneficial to the cell performance especially in the presence of the anodic MPL in relation to the one without anodic MPL.

7.4 Summary

The present chapter compares the electrode with different thicknesses of the catalyst layers in the presence and the absence of the MPL, respectively. Following results are observed:

- I : As the thickness of the catalyst layer increases, the thickness and platinum loading of GDE increase as well as the crack width in the catalyst layer.
- II : The gas permeability of the GDE increases as the catalyst layer thickness is raised with the inclusion of the MPL. There is no obvious tendency for the MPL free GDE.
- III : The cell performance is improved as the anode thickness is reduced. The best anode is the GDE containing a MPL with θ_{CL} of 15 µm.

8 Catalyst Layer Morphology, Platinum Loading and Phosphoric Acid Content

Chapter 7 has revealed that improved cell performance can be achieved by reducing the thickness of the anodic catalyst layer. In this chapter the catalyst layer thickness (and catalyst loading) of anode and cathode will be modified simultaneously as well as the acid uptake in the MEA. A series of experiments was carried out to investigate these effects and interactions on the performance of the HT-PEFC.

The experimental work was partly completed by Sajedeh Mohajeri and Yidu Di within their master thesis [126] and scientific internship, respectively. The impedance analysis was supported by Dr. Klaus Wippermann. A part of this work was published [112; 113] and presented as an oral presentation at EFCF 2013 – 4th European PEFC and H_2 Forum.

8.1 Experimental plan

To determine the effect of the catalyst layer thickness, the platinum loading and the acid uptake on the cell performance, a three-level factorial matrix encompassing 15 experimental points was designed as visualized in Fig. 8.1.

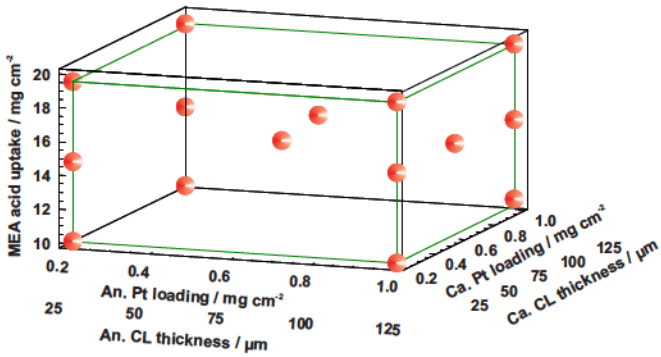

Figure 8.1: Experimental plan to evaluate the MEA component contents on the performance of HT-PEFCs [113, Fig.1].

According to the pre-defined plan (Fig. 8.1), three catalyst loadings of the electrodes are required. In the experiments, they were achieved by depositing the catalyst layer with identical catalyst slurries and varied thicknesses of the spacers, as described in Chapter 7. The relationship between the Pt loading and the thickness of the catalyst layer (θ_{CL}) is plotted in Fig. A13. Three different electrodes were prepared with modified catalyst loadings and thicknesses as listed in Tab. 8.1.

Table 8.1: Pt loading and thickness of catalyst layer as required in Fig. 8.1.

		I	II	III
Pt loading	mg cm^{-2}	0.16 $\otimes$ 0.02	0.43 $\otimes$ 0.08	0.95 $\otimes$ 0.05
θ_{CL}	µm	18 $\otimes$ 4	52 $\otimes$ 12	128 $\otimes$ 17

Three levels of acid uptakes were obtained by varying the method to introduce the phosphoric acid into the MEA:

- I : the membranes were immersed into an open bath (Fig. 4.1) of 85 wt.-% phosphoric acid at 70 °C for 15 h. The acid uptake reached a level of 11$\otimes$1 mg cm^{-2}.
- II : the membranes were doped in the same way as in process I, while the temperature of the acid bath was raised up to 115 °C. The acid uptake was increased to 15$\otimes$1 mg cm^{-2}.
- III : a part of the required acid uptake was obtained as in process I; the rest of phosphoric acid was introduced into GDEs directly with a pre-defined volume as described in Section 3.2.2. The final acid uptake of the MEA was 19$\otimes$1 mg cm^{-2}.

In total, 21 cells were prepared according to the pre-defined conditions. A few cells were repeated twice or three times for controlling the reproducibility of the experiments. The values of the catalyst loading, θ_{CL} and the acid uptake of the investigated cells are listed in Tab. A3. The electrochemical characterization was carried out with these cells as described in Section 3.4. The experimental data were collected and statistically analyzed according to the method mentioned in Section 2.5 and Section 3.6. The fitted results were expressed in three-dimensional graphics cubes.

8.2 Results and analysis

8.2.1 Cell voltage

The polarization curves of the HT-PEFCs were recorded after the break-in procedure. The voltage at 200 mA cm^{-2} was collected and further analyzed as described in Section 3.6. The results are visualized as a graphic cube in Fig. 8.2. The voltage is strongly influenced by the interactions of the MEA components as well as of the thickness of anodic and cathodic catalyst layer ($\theta_{CL,An.}$ and $\theta_{CL,Ca.}$). The highest voltage is obtained at an acid uptake of 20 mg cm^{-2}, and a catalyst loading of 1.0 mg cm^{-2} and 0.6 mg cm^{-2} for cathode and anode, as marked with a star in Fig. 8.2. The related thickness of the catalyst layer is 125 µm and 75 µm, respectively. In addition, a similar

tendency was also observed for the current density at 0.5 V (not shown here). This indicates that the interactions of the catalyst and acid content have the same effects on the cell performance at both low and high current densities. To understand the effects of each parameter and their interactions on the cell performance, a series of investigations was carried out as following.

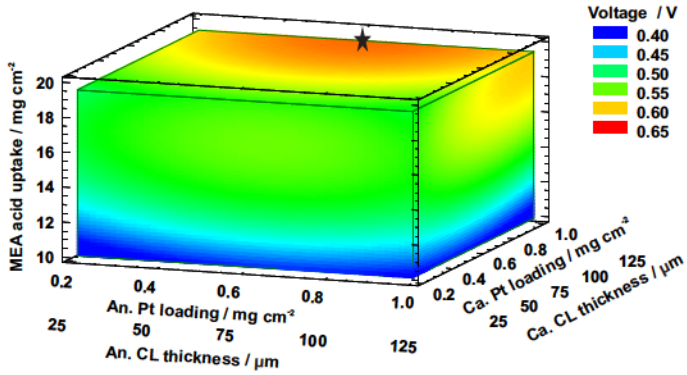

Figure 8.2: Cell voltage at 200 mA cm^{-2} with $\lambda_{H_2/air}$ = 2/2 [113, Fig.4]. The original data were obtained from polarization curves recorded after a break-in process of 70 h. The goodness-of-fit of the statistical model is 92.0 %.

8.2.2 Resistances

EIS measurements were performed after 140 h of operation in order to distinguish and quantify all kinds of resistances according to the equivalent circuit as shown in Fig. 3.6. Ohmic resistance (R_o), proton resistance (R_p), charge transfer resistance (R_{ct}) and mass transport resistance (R_m) were distinguished from high to low frequency, respectively. The values of resistances are visualized as cubes after the statistical analysis, which are presented from Fig. 8.3 to Fig. 8.6.

R_o denotes the resistance of the proton conductivity in the membrane [117]. Fig. 8.3a shows R_o at OCV. R_o is about 250 m cm^2 for the cell with catalyst loadings of 1.0 mg cm^{-2} in both anode and cathode as well as for a MEA acid uptake of 20 mg cm^{-2}, as marked with $\star$ in Fig. 8.3a. The value of R_o is consistent with the one obtained by [117]. However, it must be noted that the membrane here is twice as thick as the one used in the literature, and shows 50 % less acid uptake. This means R_o obtained here is expected higher than the observed value. The reduced value is attributed to the operating process. The Nyquist plot was recorded when the cell was operated at OCV for 10 min in the present work. However, [117] revealed that the cell needs about 1 h to reach steady-state at OCV. In other words, the cells did not reach steady-state during the recording of the Nyquist plots. Since all of the cells were operated at the same procedure, R_o observed here can be used for a qualitative characterization but not for a quantitative comparison with other publication.

As shown in Fig. 8.3a, R_o at OCV is reduced by raising the MEA acid uptake. This agrees with *ex-*

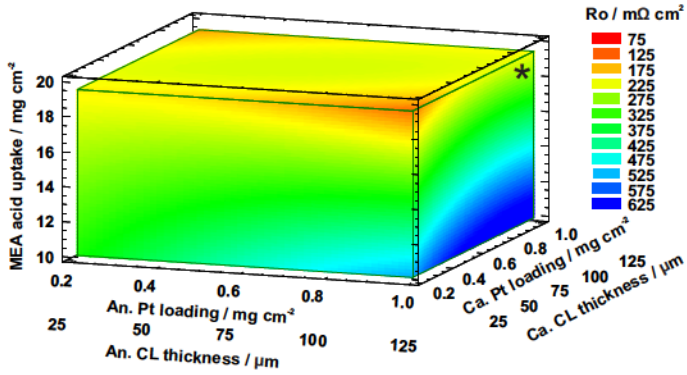

(a)

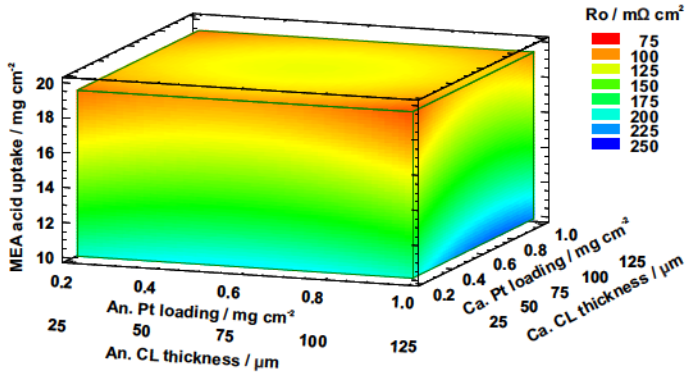

(b)

Figure 8.3: Ohmic resistance (R_o) at (a) OCV and (b) 200 mA cm^{-2} with $\lambda_{H_2/air}$ = 2/2 [113, Fig.5]. The goodness-of-fit of the statistical model is 90.2 % and 93.8 %, respectively.

situ resistances of doped membranes, as described in Appendix A2.3. In addition, R_o increases with θ_{CL}, especially at the low level of the MEA acid uptake. Moreover, R_o declined when switching the cell from a currentless operation to the one where current was drawn (Fig. 8.3). The decay of R_o is caused by the fact that the water production leads to a hydration of phosphoric acid [65; 70]. Fig. 8.3 shows the lowest R_os at OCV and 200 mA cm^{-2} at an acid uptake of 20 mg cm^{-2} with two combinations of the cathode and anode as below:

i : catalyst loadings of 1.0 mg cm^{-2} and 0.2 mg cm^{-2} for cathode and anode, with thicknesses of the corresponding catalyst layer of 125 µm and 25 µm;

ii : catalyst loadings of 0.2 mg cm^{-2} and 1.0 mg cm^{-2} for cathode and anode, with thicknesses of the corresponding catalyst layer of 25 µm and 125 µm;

R_p is defined as the resistance of proton conductivity in the cathode [117; 132]. It is sensitive to

the acid content and distribution in the porous cathode catalyst layer [70]. Fig. 8.4 shows that R_p decreases mainly with the increase in the acid uptake of MEA. In addition, R_p shows a complicated variation with $\theta_{CL,An.}$. As $\theta_{CL,An.}$ is raised, R_p decreases and increases at a low and a high level of MEA acid uptake, respectively. In overall, the lowest R_p is obtained with the MEAs containing a high level of acid uptake and a low level of $\theta_{CL,An.}$.

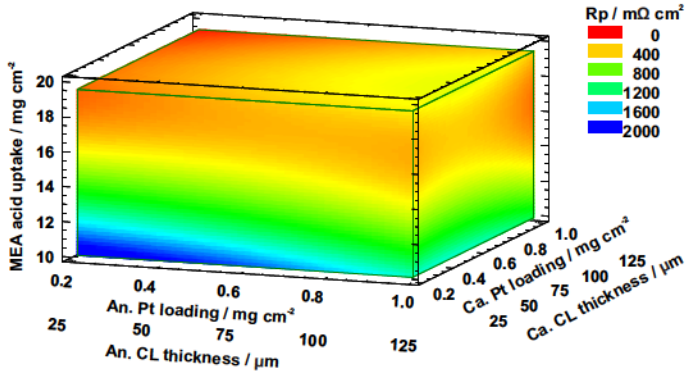

Figure 8.4: Proton (cathode) resistance (R_p) at 200 mA cm^{-2} with $\lambda_{H_2/air}$ = 2/2 [113, Fig.6]. The goodness-of-fit of the statistical model is 88.8 %.

R_{ct} is normally determined by the cathodic kinetics since the ORR kinetic is several orders of magnitude slower than that of HOR [1, p.38; 60, p.92]. Chapter 7 and Appendix A3.5 confirm that the reduction of the anodic catalyst loading has no negative influence on the HOR kinetics. Therefore, the varied R_{ct} here (see in Fig. 8.5) is attributed only to the cathodic kinetics. The cathodic kinetics can be improved by the enlargement of the cathode active area and the improvement of the O_2 supply [69; 100; 117; 133].

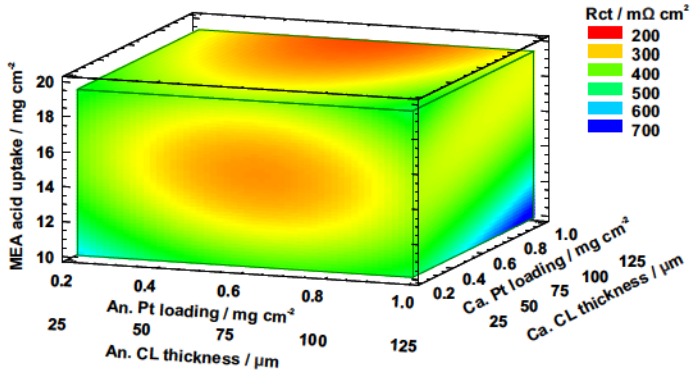

Figure 8.5: Charge transfer resistance (R_{ct}) at 200 mA cm^{-2} with $\lambda_{H_2/air}$ = 2/2 [113, Fig.7]. The goodness-of-fit of the statistical model is 86.0 %.

It can be seen in Fig. 8.5, that R_{ct} declines firstly then rises as long as the MEA acid uptake and $\theta_{CL,An.}$ are raised. With an elevated $\theta_{CL,Ca.}$, R_{ct} increases at the low level of the MEA acid uptake, however, decreases at the high level of the MEA acid content. It should be noted that the enhanced $\theta_{CL,Ca.}$ also increases the cathode catalyst loading and enlarges the initial surface area of platinum (Fig. 8.9). The lowest R_{ct} can be found when the cell contains 20 mg cm^{-2} of phosphoric acid, 1.0 mg cm^{-2} and 0.6 mg cm^{-2} of cathode ($\theta_{CL,Ca.}$ = 125 µm) and anode ($\theta_{CL,An.}$ = 75 µm). The optimized cell performance is obtained under the same condition as shown in Fig. 8.2. In other words, the performance of HT-PEFC is mainly determined by the kinetics of ORR.

R_m is related to the oxygen depletion along the flow channel in the cell [134]. Fig. 8.6 shows that R_m is modified by the MEA acid uptake and $\theta_{CL,Ca.}$. As long as the MEA acid uptake is raised, R_m declines until the minimum and then rises especially when $\theta_{CL,Ca.}$ is in a low level. If the MEA acid uptake is maintained in a low level, R_m increases with $\theta_{CL,Ca.}$. However, the extent of the R_m variation is 5 times smaller than that of R_{ct} (Fig. 8.5 and Fig. 8.6). The lowest R_m is obtained at an acid uptake of 15 mg cm^{-2} and a cathodic catalyst loading of 0.2 mg cm^{-2} ($\theta_{CL,Ca.}$ = 25 µm).

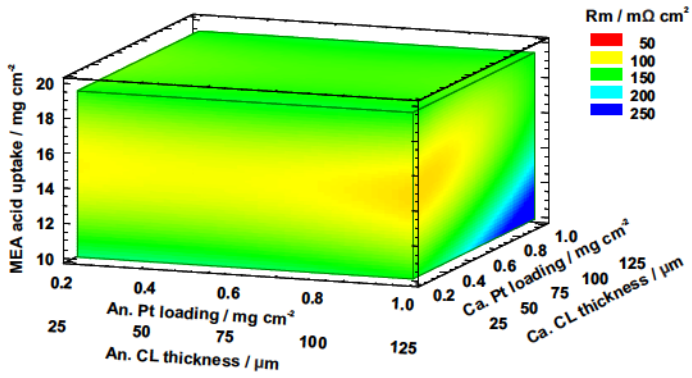

Figure 8.6: Mass transport resistance (R_m) at 200 mA cm^{-2} with $\lambda_{H_2/air}$ = 2/2 [113, Fig.8]. The goodness-of-fit of the statistical model is 92.3 %.

8.2.3 Water collection

The water anode ratio (w) is defined as the mass ratio of water collected at the anode to the total water collection (Eqn. 3.7). The higher value of w means more water departs from the anode to the outlet, or less water is removed from the cathode. Fig. 8.7 shows the variation of w with the component content. The value of w is lower than 20 %, which is independent of the acid and catalyst content. This means the water collected at the anode is less than that at the cathode. This is associated with the fact that the cathode was fed by air. With the same stoichiometry, the flow rate of H_2 at the anode is 0.42 times smaller than that of air at the cathode. Therefore, less water evaporates and departs from the anode to the outlet in comparison to the cathode.

As long as $\theta_{CL,Ca.}$ and $\theta_{CL,An.}$ are raised, w increases at a low level of the MEA acid uptake, while it

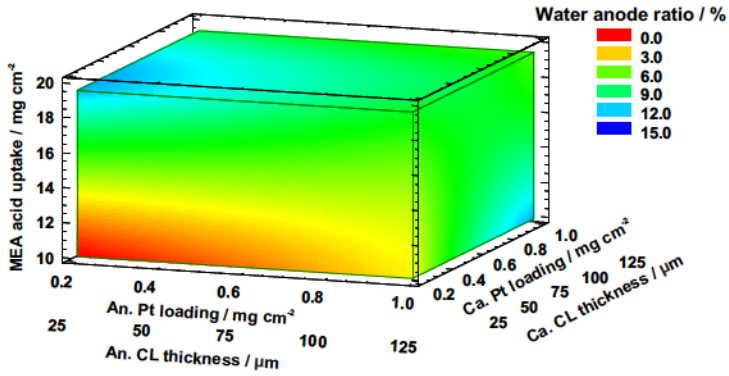

Figure 8.7: Water anode ratio (w) after 145 h of operation. The HT-PEFCs were operated at 200 mA cm^{-2} and $\lambda_{H_2/air}$ = 2/2 [113, Fig.9]. The goodness-of-fit of the statistical model is 84.5 %.

decreases at a high level of the MEA acid uptake. Since the overall water collection is constant for all cells, the variation of w indicates the change of water distribution in the MEAs (Chapter 6 and Chapter 7). The water transport in the MEA is modified with regard to the structure of the catalyst layer and the MEA acid uptake. The possible mechanisms will be discussed in Section 8.3.

8.2.4 Active surface area of cathode catalyst

Based on CV curves, the active surface area of the cathode ($A_{act.}$) was computed according to Eqn. 3.6 [46]. It should be noted that $A_{act.}$ is associated with the area of the catalyst with electrical and proton conductivity. The phase of O_2 is not included since the CV experiments are carried out at the O_2 free cathode [20]. Assuming that the catalyst is well electrically connected, $A_{act.}$ obtained with CV curves then depends on the surface area of platinum covered by phosphoric acid. ECSA in unit of m^2 g^{-1} is not considered here because it focuses on the utilization of the catalyst. For the comparison among the varied cathodic catalyst loading, the absolute value of the active area ($A_{act.}$ in unit of m^2) is more reasonable to evaluate the acid distribution in the catalyst layer.

It is shown in Fig. 8.8 that $A_{act.}$ is dominated by the cathode catalyst loading, as emphasized in Fig. 8.9. $A_{act.}$ rises linearly with the cathode catalyst loading. This general behavior is independent of the MEA acid uptake and the anode catalyst loading. The slope of $A_{act.}$ against the cathode catalyst loading is a factor of 8 smaller than that for the initial Pt surface area (before operation). A decay of cathode catalyst utilization was observed with the increase in the catalyst loading (Fig. A9).

In addition, $A_{act.}$ is also influenced slightly by the MEA acid uptake and $\theta_{CL,An.}$. Fig. 8.8 illustrates that $A_{act.}$ is enlarged 35 % approximately when the MEA acid uptake increases from 10 mg cm^{-2} to 20 mg cm^{-2}. As long as the anode catalyst loading is raised, $A_{act.}$ rises by 25 % if the MEA acid uptake and cathode catalyst loading are both at high levels. The highest $A_{act.}$ is given by the

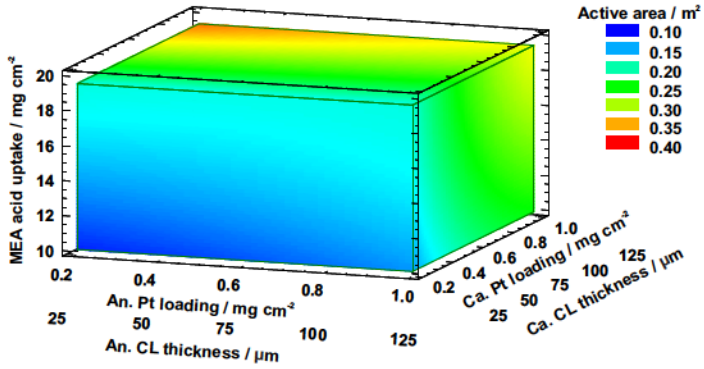

Figure 8.8: Cathode active area after 145 h of operation (redrawn from [112, Fig.3]). The goodness-of-fit of the statistical model is 97.3 %.

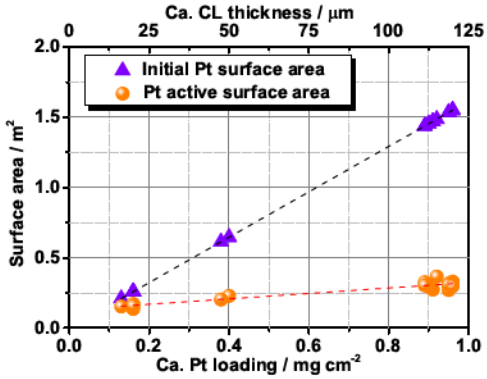

Figure 8.9: Cathode active area as a function of the cathode loading (redrawn from [112, Fig.4]). The values of cathode active area are the same as the original data in Fig. 8.8.

following conditions: 20 mg cm^{-2} of MEA acid uptake, 1.0 mg cm^{-2} and 0.2 mg cm^{-2} of catalyst loadings for cathode ($\theta_{CL,Ca.}$ = 125 µm) and anode ($\theta_{CL,An.}$ = 25 µm).

In brief, the effects discussed above have been summarized in Tab. 8.2 under currentless operation and in Tab. 8.3 for 200 mA cm^{-2}. The optimized cell performance is obtained at an acid uptake of 20 mg cm^{-2}, a cathode and anode loadings of 1.0 mg cm^{-2} and 0.6 mg cm^{-2}. The catalyst layer thickness is 125 µm for the cathode and 75 µm for the anode. At the same condition, the lowest R_{ct} is found, along with a low level of R_o and R_p, and a high level of $A_{act.}$.

Table 8.2: Effects of MEA component contents on the performance of HT-PEFCs under OCV.

	Increase of MEA acid uptake	Increase of cathode Pt loading and $\theta_{CL,Ca.}$	Increase of anode Pt loading and $\theta_{CL,An.}$
low MEA acid uptake	R_o $A_{act.}\downarrow$	$R_o\downarrow$ $A_{act.}\downarrow$	$R_o\downarrow$ (slight)
high MEA acid uptake	R_o $A_{act.}\downarrow$	$A_{act.}\downarrow$	$A_{act.}$

Table 8.3: Effects of MEA component contents on the performance of HT-PEFCs at 200 mA cm^{-2}.

	Increase of MEA acid uptake	Increase of cathode Pt loading and $\theta_{CL,Ca.}$	Increase of anode Pt loading and $\theta_{CL,An.}$
low MEA acid uptake	R_o R_p R_{ct} R_m	$R_{ct}\downarrow$ $R_m\downarrow$ $w\downarrow$	R_p R_{ct} then $\downarrow$ $w\downarrow$
high MEA acid uptake	R_o R_p $R_{ct}\downarrow$ $R_m\downarrow$	R_{ct} w	$R_p\downarrow$ R_{ct} then $\downarrow$ w

8.3 Discussion

The experimental results will be further discussed in this section to reveal the effects of the catalyst and phosphoric acid content on the cell performance. When the cells are operated under load, the water is produced and modifies the acid distribution in the MEA. Therefore, the following discussion will be divided into two parts depending on whether the cell is operated under currentless condition or under constant load.

8.3.1 Cell operated under currentless condition

Ex-situ conductivity experiments (Appendix A2.3) revealed that R_o is proportional to the membrane acid uptake at constant water vapor partial pressure. The same values of R_o are expected to be observed in the *in-situ* experiments of the HT-PEFC, if the acid content of the membrane and the surrounding conditions are identical. This simple estimation assumes that the proton conductivity is isotropic for the doped ABPBI membranes. The conductivity obtained with the *ex-situ* experiments are measured in the in-plane direction, whereas the *in-situ* experiments are performed in the through-plane direction. In the other words, the in-plane conductivity is considered as the same as the through-plane conductivity of the doped ABPBI membrane. To make it clear, the assumption can be presented as the following statement:

if $m_{acid\ in\ ABPBI,\ in-situ} = m_{acid\ in\ ABPBI,\ ex-situ}$, $R_0(in\text{-}situ) = R_0(ex\text{-}situ)$, and *vice versa*.

Under these assumptions, the acid content in the assembled membrane can be estimated by comparing R_0 obtained with *in-situ* (Fig. 8.3a) and *ex-situ* (Fig. A7) measurements. Since the acid conductivity is sensitive to p_{H_2O} [65], the comparison must be carried out under the identical p_{H_2O}. For the cell which is fed with dry gases (Section 3.4.1) and operated at OCV, a certain amount of water will be produced due to the H_2 leakage through the membrane and recombination to water [135]. There are no detailed data available on p_{H_2O} in the MEA at the interface between phosphoric acid and the surrounding gas phase under this condition. On one side, a rough estimation was published in [70]. The authors estimated p_{H_2O} in the MEA in the vicinity of the cell outlet as being about 8 mbar. In the present work the value of p_{H_2O} at the interface between the acid solution and the gas flow in the cathode was approximately estimated as 15 mbar. The details about the estimation will be given in Section 8.3.3. On the other side, the lowest p_{H_2O} applied in the *ex-situ* experiments was 20 mbar when the conductivities of the doped membranes were measured at 160 °C without any additional water supply (Appendix A2.3). Therefore, the value of p_{H_2O} is assumed as 20 mbar at the surrounding of the membrane during the operation at OCV. Subsequently, the acid contents in the assembled membranes are given for the cells operated at OCV. The results are visualized in Fig. 8.10.

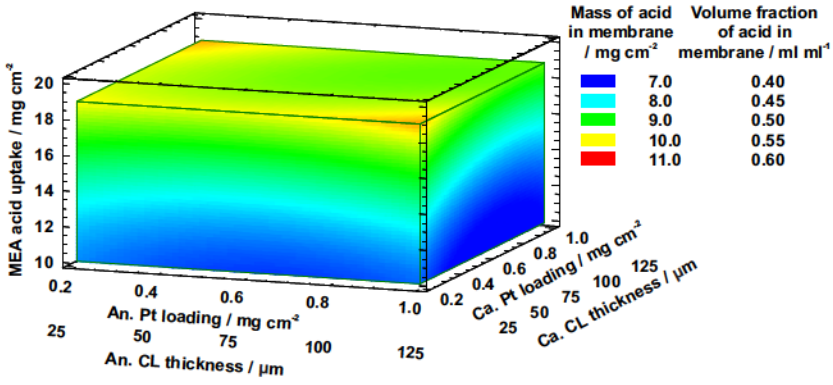

Figure 8.10: Phosphoric acid in the membrane at OCV: the mass ($m_{acid\ in\ ABPBI}$) and the volume fraction (r_{ABPBI}). The cells were operated with the gas flow equivalent to $\lambda_{H_2/air}$ = 2/2 at 200 mA cm^{-2}. The original values were obtained by comparing Fig. 8.3a and Fig. A7. The goodness-of-fit of the statistical model is 82.7 %.

The acid amount in the membrane increases with the acid uptake of the MEA, which leads to a reduction of R_0 (Fig. 8.3a) [15–17]. When p_{H_2O} = 20 mbar, the concentration of phosphoric acid reaches a value around 74 wt.(P_2O_5)% at 160 °C [65] with a density (ρ) of 1.777 g cm^{-3} [136]. These values are used to calculate the acid volume fraction of the membrane (r_{ABPBI}), which denotes the volume ratio of the acid solution to the membrane [68]. When using these values for the calculation it is implicitly assumed that the acid concentration in the membrane is nearly the same as in the surrounding electrolyte which is in contact with the gas phase. This assumption

seems to be reasonable at least for high acid concentrations (Chapter 5). It can be written as Eqn. 8.1, where A is the active area of MEA. The value of r_{ABPBI} varied from 0.40 to 0.55 by considering the thickness of the assembled membrane (θ_{AM}) as 100 µm (Fig. 8.10 and Fig. A2).

$$r_{ABPBI} = \frac{m_{acid\ in\ ABPBI}}{\rho \times A \times \theta_{AM}}\ [\mathrm{ml\ ml^{-1}}] \tag{8.1}$$

In the present MEA, there is a MPL inserted in the MEA between the catalyst layer and carbon fibers in the GDL. This MPL is regarded as a boundary layer for the phosphoric acid. Therefore, the phosphoric acid is assumed to be fixed inside the membrane and the catalyst layer. The content of acid in the catalyst layers is the mass difference between the overall acid uptake in the MEA and the acid content in the membrane. When the MEA contains 10 mg cm^{-2} of phosphoric acid, 7 mg cm^{-2} are located in the membrane and 3 mg cm^{-2} in the electrodes. When the MEA acid uptake is 19 mg cm^{-2}, the acid content differs around 10 mg cm^{-2} in the membrane and 9 mg cm^{-2} in the electrodes. It indicates that phosphoric acid is absorbed priority by the membrane rather than by the catalyst layers.

When θ_{CL} is raised, more acid will accumulate in the catalyst layer. The acid volume in the catalyst layer can also be calculated in the same way as that of the membrane. It is assumed that the volume of the catalyst layer remained stable during the assembly and the operation.

The next step is to separate the acid content in the anode and cathode. Two possible models are described in the following.

I: The same amount of acid in the cathode and anode.

The basis of the hypothesis is that the same amount of acid will be pressed out of the membrane to both sides during the cell assembly, which is independent of θ_{CL}. The content and volume fraction of the acid in the catalyst layer can be computed according to Eqn. 8.2 and Eqn. 8.3. Since the effects of both factors are the same in the anode and cathode, Fig. 8.11 only illustrates the acid content and volume fraction in the cathode.

$$m_{acid\ in\ Ca.} = m_{acid\ in\ An.} = \frac{1}{2}(m_{acid\ in\ MEA} \quad m_{acid\ in\ ABPBI})\ [mg\ cm^{-2}] \tag{8.2}$$

$$r_{Ca.} = \frac{m_{acid\ in\ Ca.}}{\rho \times A \times \theta_{CL,Ca.}}\ [\mathrm{ml\ ml^{-1}}]\ ,\ r_{An.} = \frac{m_{acid\ in\ An.}}{\rho \times A \times \theta_{CL,An.}}\ [\mathrm{ml\ ml^{-1}}] \tag{8.3}$$

The acid content in the cathode is independent of $\theta_{CL,Ca.}$, while it is proportional to the MEA acid uptake. When $\theta_{CL,Ca.}$ is less than 30 µm, the acid volume fraction is close to 1 at a high level of the MEA acid uptake. This means the catalyst layer is saturated with the acid at this condition. In the rest of the studied range, the acid volume fraction of the cathode is lower than 0.4. More than half of the catalyst layer is not in contact with the acid. Considering the wider cracks in the thicker

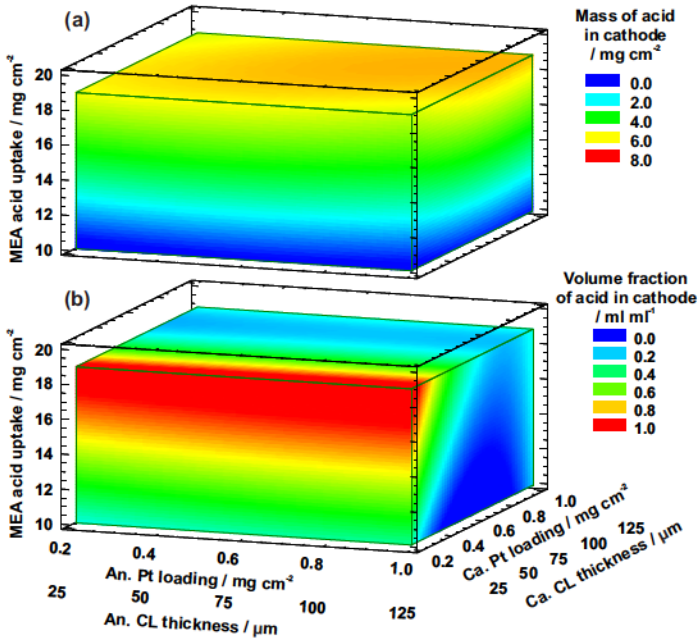

Figure 8.11: Phosphoric acid in the cathode at OCV: (a) the mass ($m_{acid\ in\ Ca.}$) and (b) the volume fraction ($r_{Ca.}$). The cells were operated with the gas flow equivalent to $\lambda_{H_2/air}$ = 2/2 at 200 mA cm^{-2}. The original values were obtained by comparing Fig. 8.3a and Fig. A7, according to Model I. The goodness-of-fit of the statistical model is 95.1 % for (a) and 98.4 % for (b).

catalyst layer (Fig. 7.2), more acid accumulates in the cracks due to the hydrophobic nature of the catalyst layer [60, pp.893-898]. The content and volume fraction of the acid are reduced in the porous blocks, which hinders the contact between the acid solution and the Pt surface. Therefore, $A_{act.}$ decreases with an increased $\theta_{CL,Ca.}$. However, the experimental results revealed that $A_{act.}$ was enlarged when $\theta_{CL,Ca.}$ was raised. The assumption seems to be inappropriate to characterize the acid distribution in the MEA.

II: The same acid volume fraction of anode and cathode.

The assumption considers that the acid transport into the catalyst is proportional to the volume fraction of the corresponding catalyst layer. The acid content and volume fraction are calculated by Eqn. 8.4 and Eqn. 8.5. In the same way as for Model I, the variations of the two parameters in the cathode are presented in Fig. 8.12.

$$m_{acid\ in\ Ca.} + m_{acid\ in\ An.} = m_{acid\ in\ MEA} \quad m_{acid\ in\ ABPBI}\ [mg\ cm^{-2}] \tag{8.4}$$

$$r_{Ca.} = r_{An.} = \frac{m_{acid\ in\ MEA} \quad m_{acid\ in\ ABPBI}}{\rho \times A \times (\theta_{CL,Ca.} + \theta_{CL,An.})}\ [\mathrm{ml\ ml^{-1}}] \tag{8.5}$$

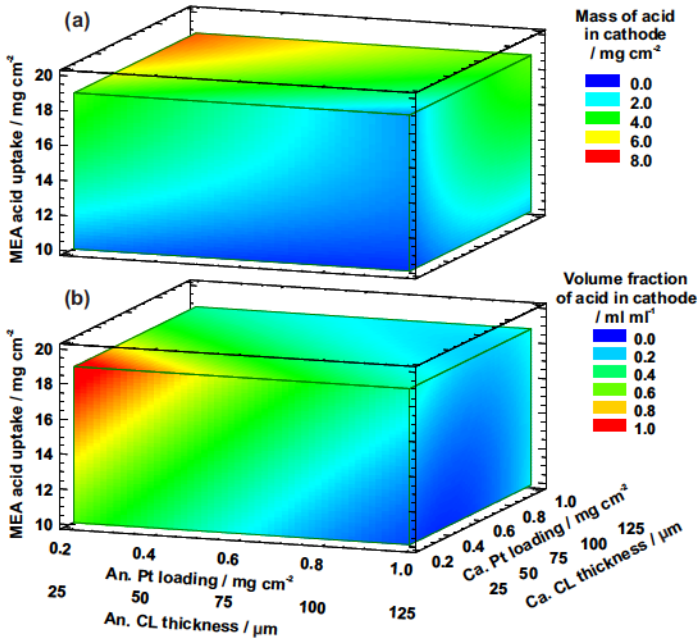

Figure 8.12: Phosphoric acid in the cathode at OCV: (a) the mass ($m_{acid\ in\ Ca.}$) and (b) the volume fraction ($r_{Ca.}$). The cells were operated with the gas flow equivalent to $\lambda_{H_2/air}$ = 2/2 at 200 mA cm^{-2}. The original values were obtained by comparing Fig. 8.3a and Fig. A7, according to Model II. The goodness-of-fit of the statistical model is 98.1 % for (a) and 98.4 % for (b).

Fig. 8.12 shows that the catalyst layer is saturated with the acid for the cell with a high level of acid uptake and low levels of $\theta_{CL,An.}$ and $\theta_{CL,Ca.}$, simultaneously. Except at full saturation, the acid volume fraction of the catalyst layer is lower than that of the membrane in the entire tested range. The increase in $\theta_{CL,Ca.}$ leads to a reduction of $r_{Ca.}$. More acid is forced into the cathode, which increases the acid content in the cracks and blocks of the catalyst layer. It is beneficial for the enlargement of $A_{act.}$ (Fig. 8.8). If $\theta_{CL,An.}$ is raised, more acid will transport into the thicker anode. It leads to a lack of the acid in the cathode and a reduced $A_{act.}$, especially when the MEA acid uptake is in a high level.

In addition to $A_{act.}$, the variation of θ_{CL} also influences R_o at OCV, if comparing Fig. 8.3a and Fig. 8.12-b. As long as θ_{CL} is raised, R_o rises when $r_{Ca.}$ (= $r_{An.}$) is less than 0.5; while R_o declines when $r_{Ca.}$ is higher than 0.5. The factor of 0.5 is also the mean value of r_{ABPBI}. It indicates more acid will be adsorbed by the thicker catalyst layer when $r_{Ca.} < r_{ABPBI}$. The lack of the acid content in the membrane causes an increase in R_o. However, this is not suitable for the case

when $r_{Ca.} > r_{ABPBI}$. Because the reduction on the acid content in the membrane is not clearly observed (Fig. 8.12-a). The decreased R_o is attributed to the variation of the acid concentration. As mentioned above, the acid concentration at OCV is considered as 73.8 wt.(P_2O_5)%. With this concentration, the proton conductivity increases when the acid concentration is reduced [65]. In other words, the elevated θ_{CL} causes a reduced R_o due to the dilution of phosphoric acid.

Therefore, the content of phosphoric acid in the anode and cathode can be characterized by the second model. To explain the variation of the acid concentration in the MEA, the further discussion is required especially when the water is produced under constant load.

8.3.2 Cell operated under constant load

When the cell is operated under constant load, the situation inside the cell is completely different from the case at OCV. At OCV only a small amount of water was generated due to the hydrogen leakage through the membrane. Therefore, the phosphoric acid inside the MEA could be assumed to be in thermodynamic equilibrium with the gas inside the gas channels. The acid concentration can be correlated with the water vapor partial pressure inside the gas channel [70]. When a cell is operated under load, water will be produced at the phosphoric acid coated catalyst sites in the cathode. The reaction occurs inside the phosphoric acid solution. The transport of the water through the phosphoric acid, the catalyst layer, the MPL and the GDL into the gas channel results in a consequence where the acid concentration cannot directly be estimated as that at OCV.

In addition to the hydration of phosphoric acid, the water production also causes an expanded acid volume in the MEA in comparison to OCV [127]. The content and volume fraction of the acid in the catalyst layer should be higher than that shown in Fig. 8.12. This also changes the acid distribution inside the catalyst layer simultaneously. As discussed in Chapter 7, the porous catalyst layer is divided into blocks by macro-cracks. The micro- and/or meso-pores are found in the blocks [47]. The cracks become wider when θ_{CL} is raised. Since the catalyst layer consists of a large amount of PTFE, the cracks can be considered as hydrophobic capillaries [60, pp.893-898; 64]. The macro-cracks will be filled with phosphoric acid before the micro- and/or meso-pores are flooded, as illustrated in Fig. 8.13.

The acid distribution in the catalyst layer has significant influences on the water vapor transport. There are two major effects:

i : When the acid accumulates in cracks, the water evaporation occurs at the interface between the acid solution and the gas flow. When θ_{CL} is raised, the cracks become wider (Chapter 7) and d rises as illustrated in Fig. 8.13. The area of the liquid-gas interface is enlarged, which improves water departing from the catalyst layer.

ii : When the acid solution is present in the micro- and meso-porous blocks, the water vapor is forced to diffuse through the porous media. The diffusion distance (l, see in Fig. 8.13) become larger as long as θ_{CL} is increased. Therefore, the water removal from the catalyst layer is reduced.

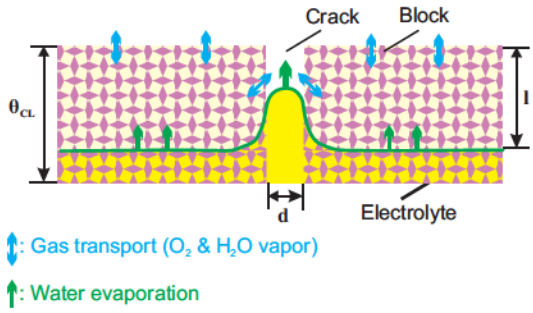

Figure 8.13: Schematic illustration of the water evaporation from the acid solution in the cathode catalyst layer.

The effect of acid distribution and water vapor transport on the performance of HT-PEFC will be described below. The discussion will be categorized into five parts depending on the variation of the MEA acid uptake, the thickness and the catalyst loading of the anode and the cathode.

A: Increase in MEA acid content

As long as the acid uptake of MEA is raised, the acid content in the membrane and the catalyst layers increase simultaneously, in the same tendency as that at OCV (Fig. 8.10 and Fig. 8.12). R_o and R_p decline [70], as shown in Fig. 8.3b and Fig. 8.4.

In the case of low phosphoric acid content in the MEA, the acid fills mostly the cracks of the electrodes. The transport of the gases through the acid-free pores is not hindered. However, at the same time, the percolating network of the proton conducting phase from the cathode to the membrane is limited. Therefore, the area of the three-phase boundary is low which results in a high level of R_{ct}.

When a high level of acid is present in the MEA, the micro- and meso-pores will be filled in addition to the cracks. All catalyst particles are covered with the acid. The percolating pathway for the gases is blocked. This again leads to a high R_{ct}. The consequence also occurs in the case of very thin electrodes, because no obvious cracks are observed.

Therefore, R_{ct} and R_m decreased first and then increased with the raised MEA acid uptake, as shown in Fig. 8.5 and Fig. 8.6.

B: Increase in anode catalyst loading (thickness) at a low level of MEA acid content

With the increase in $\theta_{CL,An.}$, more water is collected from the anode when the MEA acid uptake is in a low level (see in Fig. 8.7). The effect agrees with *Effect i*. It indicates that the acid accumulates in the cracks of the anode catalyst layer. The water evaporation from the cracks dominates the process of water departing from the catalyst layer.

Meanwhile, the decreased water collection at the cathode is associated with the reduction of the water concentration. In another words, the concentration of phosphoric acid in the cathode rises

with an elevated $\theta_{CL,An.}$. Since R_p declines at the same time, it means the proton conductivity of phosphoric acid at the cathode increases with the acid concentration. The effect will be further discussed in Section 8.3.3.

However, the O_2 transport through the phosphoric acid is hindered when the acid concentration is increased [69]. Moreover, the thicker anode adsorbs more acid, which reduces the acid content in the cathode. Both effects cause an increase in R_{ct} as long as $\theta_{CL,An.}$ is raised. It is not clear why R_{ct} declines at first with the elevated $\theta_{CL,An.}$. It could be associated with the acid distribution in the cathode. More detailed evaluation would be required to clarify this effect.

C: Increase in anode catalyst loading (thickness) at a high level of MEA acid content

Fig. 8.7 shows that less water is collected from the thicker anode, when the MEA acid uptake is in a high level. It indicates that the water departing from the anode is determined by the vapor diffusion through the micro- and meso-porous media at the anode, as *Effect ii*. This is different from the effect described in Section 8.3.2.B because more acid is present in both cracks and blocks of the anode catalyst layer.

In the meanwhile, the water removal from the cathode is improved. This means the water concentration in the cathode is increased with the elevated $\theta_{CL,An.}$. As mentioned in Section 8.3.2.B, the proton conductivity of the acid declines with the acid dilution. The inference confirms the description in Fig. 8.4 that R_p increases with $\theta_{CL,An.}$.

The reduced acid concentration improves the oxygen transport through the phosphoric acid [69]. This is beneficial to the cathodic kinetics. However, the acid content in the cathode decreases because more acid is adsorbed by the thicker anode. The $A_{act.}$ at the cathode is reduced, which hinders the ORR kinetics. As a result, R_{ct} decreases to the minimum and then increases along with the raised $\theta_{CL,An.}$.

D: Increase in cathode catalyst loading (thickness) at a low level of MEA acid content

As long as $\theta_{CL,Ca.}$ increases, the water collection from the cathode is reduced at a low level of the MEA acid uptake (see in Fig. 8.7). The effect follows *Effect ii*, that the phosphoric acid is present not only in the cracks but also in the porous blocks of the cathode. The acid distribution is different to that in the anode, which has been discussed in Section 8.3.2.B. The gas flow rate at the cathode was 2.4 times higher than that at the anode, when H_2 and air were fed into the cell with a stoichiometry of 2. In addition, the concentration of acid solution in the cathode catalyst layer is assumed to be lower than that in the anode, while the acid volume be larger, because the ORR occurs at the cathode. All these effects enhance the water evaporation at the cathode in comparison to that at the anode. Therefore, the water removal from the cathode is determined by the vapor diffusion through the porous media.

Due to the raised $\theta_{CL,Ca.}$ the limited gas diffusion also hinders the O_2 transport at the cathode. Both R_{ct} and R_m increase with $\theta_{CL,Ca.}$ at a low level of MEA acid uptake (Fig. 8.5 and Fig. 8.6).

E: Increase in cathode catalyst loading (thickness) at a high level of MEA acid content

When $\theta_{CL,Ca.}$ is raised, more water is removed from cathode at a high level of the MEA acid uptake (Fig. 8.7). As discussed in *Effect i*, the evaporation process is the dominant issue for the water removal from the cathode. The case is different to that in Section 8.3.2.D because the volume of acid solution in the cathode catalyst layer is higher here. The whole cathode catalyst layer can be flooded with the acid, which reduces the distance of gas diffusion through the porous block. Therefore, the vapor diffusion process is not the dominant issue anymore.

As $\theta_{CL,Ca.}$ increases, the loading and surface area of platinum in the cathode increases. The expanded catalyst surface area and the liquid volume in the cathode improve the active area of the cathode, which is beneficial to the ORR kinetics. The lowest R_{ct} is obtained with a high level of the MEA acid uptake, the catalyst loading and the thickness of the cathode catalyst layer.

8.3.3 Acid concentration in cathode

As mentioned above, the concentration of phosphoric acid inside the electrodes at OCV is nearly in a thermodynamic equilibrium with the water vapor partial pressure in the gas channel. When the current is drawn from the cell, water will be produced inside the phosphoric acid and disturbs the equilibrium between the water vapor partial pressure in the gas channels and the phosphoric acid in the electrode. The question which arises is: what the concentration of phosphoric acid inside the MEA?

A rough estimation can be given according to the water vapor partial pressure at the cell outlet. It is assumed that dry gases are fed at the inlet and all water production will be removed from the cathode outlet. The difference in water vapor partial pressure between the gas channel and the electrochemical active area due to water vapor transport will be taken into account. The water transport in the cathode is illustrated in Fig. 8.14. Two transport processes will be distinguished: through the acid film and through the porous GDE.

The ORR takes place at three-phase boundary. The area of three-phase boundary in an operated cell is smaller than the value of $A_{act.}$ examined by CV, because the CV experiments were carried out at the O_2 free cathode [20]. Considering the oxygen transport in the acid solution, only the top layer of the catalyst is assumed to be involved in the ORR. The three-phase boundary is located at the catalyst surface close the interface between the acid solution and the gas, which is depicted as blue line in Fig. 8.14.

Process I: ORR at active site (Pt surface)

The ORR occurs at the Pt surface at the reactive sites of the cathode. The water flux is calculated according to Faraday's law [1, p.21] (Eqn. 8.6).

$$n_{\mathrm{H_2O}} = \frac{j}{2F} \tag{8.6}$$

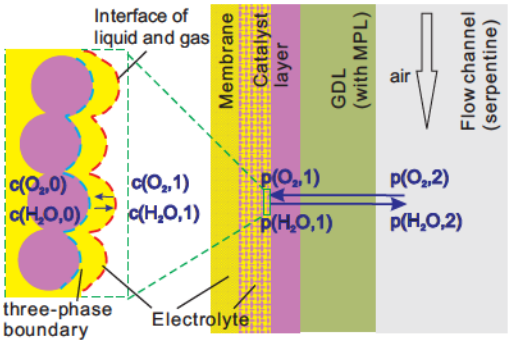

Figure 8.14: Schematic illustration of the reaction and the mass diffusion in the cathode.

n_{H_2O}	mol $s^{-1}cm^{-2}$	water flux
j	mA cm^{-2}	current density
F	C mol^{-1}	Faraday constant, 96485 C mol^{-1} = 96485 A s mol^{-1}

When water is produced at 200 mA cm^{-2}, n_{H_2O} is calculated as 1.03 ± 10^{-6} mol $s^{-1}cm^{-2}$. The water concentration at the three-phase region is denoted as $c_{H_2O,0}$, as shown in Fig. 8.14.

Process II: Water diffusion through the acid solution

The diffusion of one oxygen molecule into the sphere around the catalyst generates two water molecules according to the electrochemical reaction. Therefore, it is non-equimolar diffusion. Despite this fact a rough estimation is applied considering Fick's diffusion.

$$n_{H_2O} = D_{H_2O,l}\frac{\Omega c_{H_2O}}{x_1} \tag{8.7}$$

$D_{H_2O,l}$	$cm^2 s^{-1}$	diffusion coefficient of water in phosphoric acid solution
Ωc_{H_2O}	mol L^{-1}	concentration difference of water in phosphoric acid solution as illustrated in Fig. 8.14, $\Omega c_{H_2O} = c_{H_2O,0}$ $c_{H_2O,1}$
x_1	cm	diffusion distance of water in phosphoric acid solution (film thickness of the acid covered on the catalyst surface)

There is no available data of $D_{H_2O,l}$ in the literature. Majerus [137] estimated the diffusion of water in the ABPBI membrane at 160 °C and presented a diffusion coefficient of 10^{-10} cm^2 s^{-1}; Földes [138] estimated the diffusion coefficient of water through dry PBI membrane with a value of 10^{-9} cm^2 s^{-1}; In addition, Chung [139] revealed that the self-diffusion of phosphor in phosphoric acid is about 10^{-7} cm^2 s^{-1}. It is reasonabe to assume that the diffusion coefficient of water in phosphoric acid solution ranges from 10^{-7} cm^2 s^{-1} to 10^{-10} cm^2 s^{-1}. Depending on the acid distribution, the thickness of the acid film (x_1) is expected in the range of 10 nm to 1 µm. Therefore, the estimated Ωc_{H_2O} varies in a wide range from 10^{-2} mol L^{-1} to 10^3 mol L^{-1}.

Process III: Water evaporation

The water evaporation occurs at the interface between the acid solution and the gas. $p_{H_2O,1}$ is proportional to $c_{H_2O,1}$ [25, p.179-180]. According to the phase diagram (Fig. 2.6), the acid concentration at the interface can be obtained if the value of water vapor partial pressure above the solution surface is given.

Process IV: Water vapor diffusion through the GDE to the flow channel

The water vapor diffusion through the porous GDE can be described by Fick's law [140, pp.2-3; 141], as shown in Eqn. 8.8.

$$n_{H_2O} = \frac{1}{RT}\varepsilon^{1.5} D_{H_2O,air} \frac{\Omega p_{H_2O}}{x_2} \tag{8.8}$$

R	J mol^{-1} K^{-1}	gas constant 8.314 J mol^{-1} K^{-1} = 8.314 $\pm 10^4$ mbar cm^3 mol^{-1} K^{-1}
T	K	operation temperature, 433 K in study
ε		porosity of GDE, assumed as 0.5 for GDE [45; 54].
$D_{H_2O,air}$	cm^2 s^{-1}	diffusion coefficient of water in air assumed as 0.28 cm^2 s^{-1} [140, p.102]
Ωp_{H_2O}	mbar	pressure difference of water vapor between gas channel and surface of phosphoric acid in the cathode $\Omega p_{H_2O} = p_{H_2O,1}$ $p_{H_2O,2}$ (Fig. 8.14)
x_2	cm	diffusion distance of water vapor in the cathode

Assuming the catalyst layer is completely dry or flooded, x_2 varies from 275 µm to 375 µm for the investigated MEA. As a result, Ωp_{H_2O} varies from 9 mbar to 13 mbar.

The values of $p_{H_2O,2}$ can be obtained based on the water collection at the outlet. Afterwards, $c_{H_2O,0}$, $c_{H_2O,1}$ and $p_{H_2O,1}$ will be estimated. The results are listed in Tab. 8.4.

In addition, the same estimation is also applied for the case at OCV. The water vapor partial pressure at the outlet was examined as 4 – 8 mbar in [70] at the similar operating conditions as the present work. According to the above estimation and the phase diagram (Fig. 2.6), the acid composition at the interface of gas-liquid is 73 – 76 wt.(P_2O_5)%, which shows a good agreement with [70]. The current density caused by the fuel leakage is assumed as 5 mA cm^{-2} [70]. The resulting acid composition at the active site is higher than 70.5 wt.(P_2O_5)%. Fig. 2.5 displays the conductivity as a function of the acid composition. It can be seen that a maximum in the conductivity exists at temperatures below 100 °C. Therefore, the graph can be divided into two parts. At high acid concentrations the proton conductivity decreases with increasing acid concentration (right part), while an opposite behavior is observed at low acid concentrations. The estimation at OCV therefore results in a conductivity in the cathode which is located in the right part of the graph. In the mentioned region no conductivity data are available, but it can be assumed that the conductivity decreases further with increasing concentration.

Table 8.4: Water content acid concentration in different state at the cathode.

	Under OCV*	At 200 mA cm^{-2} ($\lambda_{H_2/air}$ = 2/2)
Active site (Pt surface)	$\sim c_{H_2O,0} < 2.5\,mol\,L^{-1}$ $\sim c_{PA} > 70\,wt.(P_2O_5)\%$ $\sim \rho_{PA} > 1.72\,g\,cm^{-3}$	$\sim c_{H_2O,0} > 4\,mol\,L^{-1}$ $\sim c_{PA} < 70\,wt.(P_2O_5)\%$ $\sim \rho_{PA} < 1.7\,g\,cm^{-3}$
Interface between liquid-gas	$\sim p_{H_2O,1} \uparrow 15\,mbar$ $\sim c_{H_2O,1} \uparrow 0\,mol\,L^{-1}$ $\sim c_{PA} = 73 - 76\,wt.(P_2O_5)\%$ $\sim \rho_{PA} = 1.76 - 1.82\,g\,cm^{-3}$	$\sim p_{H_2O,1} \uparrow 180\,mbar$ $\sim c_{H_2O,1} \uparrow 4\,mol\,L^{-1}$ $\sim c_{PA} \uparrow 70\,wt.(P_2O_5)\%$ $\sim \rho_{PA} \uparrow 1.70\,g\,cm^{-3}$
Flow channel	$\sim p_{H_2O,2} \uparrow 8\,mbar$ [70]	$\sim p_{H_2O,2} \uparrow 170\,mbar$ (calculated based on Fig. 8.7)

* *The flow rate is equivalent to 200 mA cm^{-2} with $\lambda_{H_2/air}$ = 2/2.*
The water vapor pressure, the acid composition (c_{PA}) and density (ρ_{PA}), at 160 °C are calculated based on [65; 136].

When the cell is operated under the current of 200 mA cm^{-2} with $\lambda_{H_2/air}$ = 2/2. The acid composition reaches a level of 70 wt.(P_2O_5)% at the gas-liquid interface and a lower level at the active site. This is a conservative estimation because the water evaporation from the phosphoric acid doesn't reach an equilibrium state during the cell operation. Therefore, the concentration of the phosphoric acid inside the electrode should be lower than the values listed in Tab. 8.4. The conductivity versus acid composition diagram (Fig. 2.5) shows that no data are available for the temperature of 160 °C and the concentration below 62 wt.(P_2O_5)%. This can be clearly explained by the fact that the phase diagram (Fig. 2.6) and the conductivities (Fig. 2.5) are measured at ambient pressure under equilibrium conditions. Under these conditions the maximal water vapor partial pressure is 1 bar. As a consequence the lowest concentration is 62 wt.(P_2O_5)%. The estimation under constant load gives a reasonable result that the proton conductivity of phosphoric acid in the cathode decreases as the acid concentration is reduced. This inference agrees with the discussion in Section 8.3.1 and Section 8.3.2.

Tab. 8.5 summarizes the effects of the catalyst layer and acid content on the mass distribution in the MEA, as well as the further influences on cell resistances. Considering all effects discussed above, the high acid uptake of the MEA is necessary to yield high proton conductivity of the membrane and the cathode. The catalyst loading and thicknesses of the cathodic catalyst layer at a high level provides a larger surface area of the catalyst and absorbs more acid. Both effects enlarge the active area, which improves the cathodic kinetics. The higher $\theta_{CL,An.}$ declines the acid content in the cathode. In addition, it causes an increase in the acid concentration with a low level of the MEA acid uptake, and a decrease with a high level one. The modified content and concentration of the phosphoric acid at the cathode influence both R_p and R_{ct}.

The optimum performance is obtained with a high level of $\theta_{CL,Ca.}$ and a medium level of $\theta_{CL,An.}$ (Fig. 8.2). The acid volume fraction of cathode catalyst layer reaches 0.3 at OCV under this condition. Comparing the difference of acid density (as listed in Tab. 8.4), the acid volume fraction is higher than 0.33 in the cathode catalyst layer when the cell is operated under load. This agrees with a simulation study which expresses an optimum volume fraction of phosphoric acid between 0.3 and 0.55 in the cathode catalyst layer [71]. It should be noted that the above discussion based

Table 8.5: Effects of the MEA component content on the mass distribution in the MEA and the cell resistances.

MEA acid uptake	Cathode Pt loading and $\theta_{CL,Ca.}$	Anode Pt loading and $\theta_{CL,An.}$	Mass distribution parameter	R_o	R_p	R_{ct}	R_m
$\downarrow$			Acid amount in membrane				
$\downarrow$	$\downarrow$	^{H}	Acid amount in cathode			^{L} $\downarrow^{H}$	^{L} $\downarrow^{H}$
$\downarrow$		^{H}	Acid volume fraction in cathode			^{L} $\downarrow^{H}$	^{L} $\downarrow^{H}$
$\downarrow$	$\downarrow$	^{H}	Active area of cathode				
		$\downarrow^{L}_{H}$	Acid concentration in cathode		$\downarrow^{O}_{j}$		
$\downarrow^{L}_{H}$	^{L}	^{L} $\downarrow^{H}$	O_2 transport in cathode				

$\uparrow$ *The raised parameter in column causes an increase on the parameter in row, and vice versa;*
$\downarrow$ *The raised parameter in columns causes a reduction on the parameter in row, and vice versa;*
$-$ *The raised parameter in column causes complicated effects the parameter in row, and vice versa*
^{H} *The effect is significant at a high level of phosphoric acid amount;*
^{L} *The effect is significant at a low level of phosphoric acid amount;*
^{O} *The effect occurs when the cell is operated at OCV;*
^{j} *The effect occurs when the cell is operated under constant load.*

on the electrode prepared in-house. A large amount of macro-cracks appears in the catalyst layer. The width of the cracks increases with the thickness of the catalyst layer. A completely different acid distribution would be obtained with a catalyst layer without any crack. The content and structure of the MEA components exhibit their influences on the mass distribution and the cell resistances in a different tendency.

8.4 Summary

The present study investigated the effects of the thickness and platinum loading of the anode and cathode catalyst layer, as well as the uptake of phosphoric acid on the performance of a HT-PEFC. According to the experimental results, the following conclusions can be made:

I : The transport of phosphoric acid in the MEA is forced by the difference of acid volume fraction between the membrane and the catalyst layer. The membrane exhibits a higher affinity to absorb the acid in comparison to the catalyst layer. The distribution of the acid in the catalyst layer is determined by the overall MEA acid uptake, the thickness and the structure of the catalyst layer.

II : As another critical factor, the concentration of phosphoric acid is modified by the water retention in the MEA. The water removal is controlled either by the evaporation pro-

cess or by the vapor diffusion. The dominant step is varied depending on the acid distribution and the gas flow. When the cells are operated under certain load, the acid concentration at the cathode remains at a low level where the acid dilution leads to a decrease in the proton conductivity of the phosphoric acid.

III : The performance of a HT-PEFC is influenced by the content of phosphoric acid in the MEA, the thickness of the anode and cathode catalyst layer, the cathodic catalyst loading, and their interactions. The interactions are connected by the distribution of phosphoric acid and gases (oxygen and water vapor) in the MEA. The optimum cell performance was obtained with an acid uptake of 20 mg cm^{-2}, and a catalyst thickness of 125 µm at cathode and 75 µm at anode. The related catalyst loadings of are 1.0 mg cm^{-2} and 0.6 mg cm^{-2}.

9 Flow Field Geometry

The former chapters have revealed that the performance of the HT-PEFC can be improved by the modification of gas and acid distribution in the MEA. In this chapter, the attention will focus on the effect of gas distribution on the cell performance. To avoid the variation of the electrode macrostructure, the gas distribution will be modified by the geometries of the flow fields.

In the present work, a customized spiral flow field was investigated. The spiral flow field was characterized and optimized with varied channel depths in a series of experiments. In addition, a long-term test was performed for the HT-PEFC assembled with an optimized spiral flow field. The same experiments were also carried out for a conventional serpentine flow field as reference.

The design of the spiral flow field was completed by Dr. Mirko Kvesić, Jens Bohner and Nils Schneider. The experimental work was performed with the help of Yuan Yuan, who worked for her scientific internship. Analysis of EIS results were accomplished with the help of Dr. Klaus Wippermann. Part of experimental results was presented as [114] and oral presentation at the Honolulu, PRiME 2012 Electrochemical Society (ECS) 222nd Meeting. In addition, the work has been partly published [99; 100].

9.1 Customized spiral flow field

A customized spiral flow field was investigated in the present work. The geometry of the flow field is shown in Fig. 9.1a. It is similar to the design proposed in [86]. The inlet and outlet located at the edge of the active area are connected by a single spiral channel. The arrangement of the spiral flow channel differs from that of the serpentine flow channels (Fig. 9.1b), where three parallel channels serpentine down from inlet to outlet. The design of the serpentine flow field has been widely used for HT-PEFCs in different groups [12; 61; 72; 82; 142].

The active area of the cell with a spiral flow field (Fig. 9.1a) was 9.1 cm^2. The widths of channel and rib, and the channel depth were all 1.0 mm. The cells assembled with these flow fields were referred to as the spiral-1.0 cell. A conventional serpentine flow field (as shown in Fig. 9.1b) was investigated as reference. The width and depth of channel were 1.0 mm as was the width of rib. The active area of the MEA was 14.4 cm^2. The related cell was referred to as the serpentine cell. The cells were assembled and characterized as described in Chapter 3.

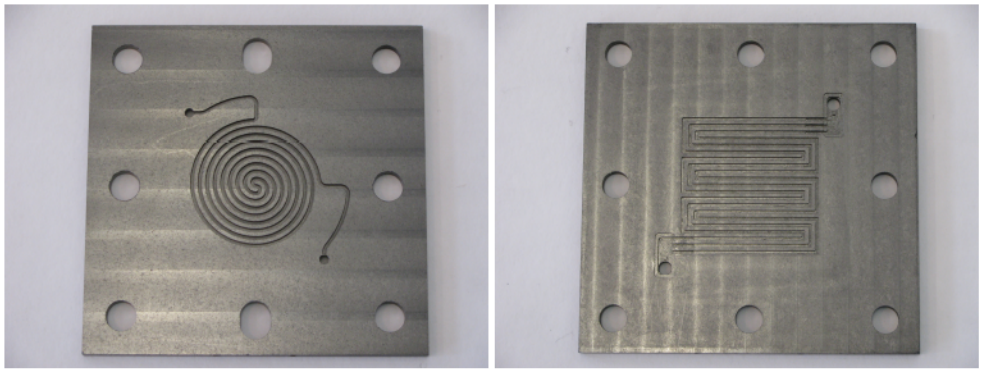

Figure 9.1: Photographs of (a) spiral and (b) serpentine flow field plates. Both flow fields have an identical rib width, and channel width and depth, all of which measured 1.0 mm.

9.1.1 Arrangement of flow channels

The geometries of spiral and serpentine flow field can be illustrated more clearly, as shown in Fig. 9.2. The first four channels from the edge of the active area were chosen to investigate the gas transport from the flow channels to the GDEs. The channels were numbered as 1, 2, 3 and 4 from the outside in order.

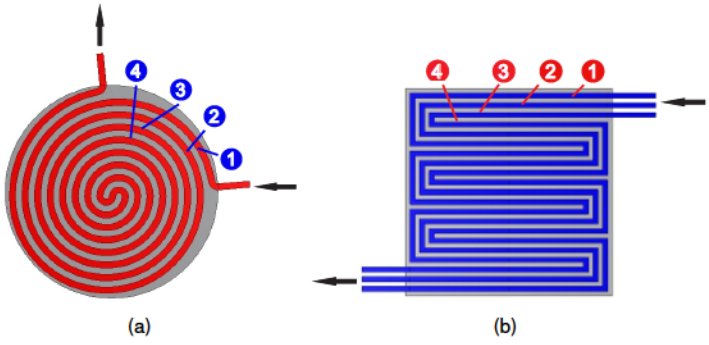

Figure 9.2: Schematic images of (a) spiral and (b) serpentine flow field, with the same geometries as shown in Fig. 9.1 (redrawn from [114, Fig.1;100, Fig.1;99, Fig.1]).

For the design of the spiral flow field, each channel close to the inlet (inlet channel) is adjacent to one close to the outlet (outlet channel). Fig. 9.2a shows that the distance between two neighbor channels is much smaller through the rib than along the spiral flow channel. Therefore, there is an obvious difference on the gas pressure between the two neighboring channels, Channel 1 and 2, as well as Channel 2 and 3. The pressure difference between adjacent channels will force the gas transport through the GDE under the rib by means of convection. Fig. 9.3a illustrates the convective flow in the GDE under the rib between two adjacent channels. This leads to a

reduction of the pressure drop between inlet to outlet of the cell. A similar effect was described in PEFCs with interdigitated [90; 91], serpentine [92–94] and spiral flow fields [89], as well as in some HT-PEFCs [81; 82]. The effect is referred to as flow crossover [89; 93].

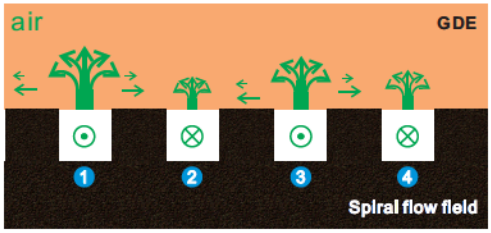

(a)

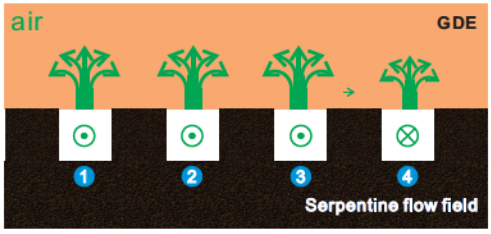

(b)

Figure 9.3: Schematic images of gas transport from (a) spiral and (b) serpentine flow channels to GDE. Arrows indicate the flow direction in the horizontal plane of the paper; • represents an air flow perpendicular to the paper from the bottom upwards, and ⊙ for the flow perpendicular to the paper from the bottom downwards.

In contrast, the serpentine flow field consists of three channels in parallel connecting the inlet and the outlet. The pressure difference between channels, 1 and 2, or 2 and 3 can be considered as zero, as shown in Fig. 9.2b and Fig. 9.3b. Although there is a pressure difference between Channel 3 and 4, the total strength of the flow crossover is still much weaker than that in the spiral cell. As a result, the flow transport through the GDE under the rib is driven mainly by diffusion rather than by convection [18; 81; 82; 94].

9.1.2 Pressure drop between inlet and outlet

The gas flow in the flow channel can be characterized by the pressure drop between inlet and outlet (ΩP). The pressure measurement was carried out with different flow rates for the spiral-1.0 and the serpentine cell. ΩP as a function of the flow rate has been plotted in Fig. 9.4. ΩP rises significantly as the flow rate increases. The slope of the spiral-1.0 cell is 6 times higher than that of the serpentine cell.

In addition to measuring the complete cell including a MEA, the pressure test was carried out for the cell assembled with a low-permeable film (PFA) with a thickness of 300 µm in order to examine the influence of the MEA on the pressure drop. The pressure drop of the spiral-1.0 cell

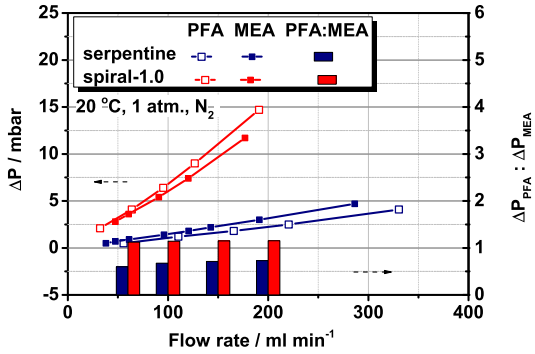

Figure 9.4: Pressure drop between inlet and outlet, and pressure ratio of the spiral-1.0 and the serpentine cells. The cells were constructed with PFA film and standard MEA, respectively, and fed with N_2 at room temperature under atmospheric pressure.

declined when the cell was assembled with a MEA in relation to the case with a PFA film. The intrusion of the GDL into the channel due to the compression of the cell during assembly, reduces the cross section of the channels [131]. This should result in a higher pressure drop. On the other hand, the flow penetration through the porous electrode under the rib should reduce the pressure drop. The effect is associated with a flow crossover as illustrated in Fig. 9.3a. The pressure measurements indicate that a flow crossover occurring between two adjacent channels dominates the total pressure drop along the spiral flow channel. The opposite effect was observed for the serpentine flow field, where the pressure drop increased. Therefore, the pressure drop is determined by the intrusion of the GDL into the channel.

The strength of crossover can be characterized qualitatively by the ratio of the pressure difference of the cells with a PFA film compared to cells with a MEA, which is abbreviated as the pressure ratio here. The higher value indicates the stronger gas permeation through GDE under the rib. In addition, Fig. 9.4 shows the value of the pressure ratio does not change significantly with the variation of the flow rate. It means that the flow crossover is an effect determined by the arrangement of the flow channel.

9.1.3 Cell performance

The cell performances were characterized with electrochemical techniques. Plots of voltages as a function of the operating time were recorded during the break-in process, as shown in Fig. 9.5. Three spiral-1.0 cells were measured. The measurements show a good reproducibility. There is a large variation of voltage at the beginning of the break-in process due to the phosphoric acid redistribution in the MEA [18]. The slope of $u \approx t$ curves became stable after an operation of 50 h. The slope in the time range from 50 h to 70 h have been collected and listed in Tab. 9.1. The positive slope was obtained with the spiral-1.0 cell, the negative one with the serpentine cell. The negative slope is attributed to the uneven distribution of current density over the active area [143].

In addition, the voltage of the spiral-1.0 cell was 35 mV higher than that of the serpentine cell at

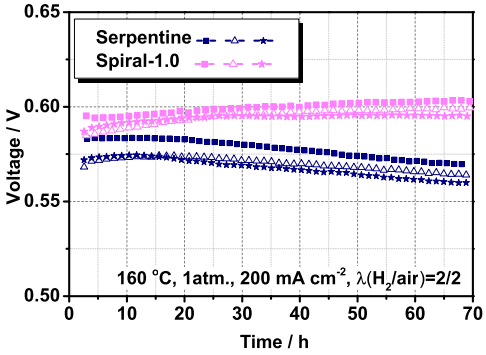

Figure 9.5: Plots of voltage against the operation time of the spiral-1.0 and the serpentine cell during break-in process. The plots were recorded at 200 mA cm^{-2} with $\lambda_{H_2/air}$ = 2/2, at ambient pressure and 160 °C. Each cell type was repeated three times with standard MEAs.

Table 9.1: Performance comparison of the spiral-1.0 and the serpentine cells.

		Spiral-1.0	Serpentine
Slope of voltage ≈ time plot 50 to 70 h *	μV h^{-1}	31.3	-234
Voltage at 200 mA cm^{-2} after operation of 70 h *	mV	599	565
Voltage at 200 mA cm^{-2} after operation of 70 h †	mV	597	555
Peak power density †	mW cm^{-2}	283	174

The data are the mean values of three cells;
* *Data were obtained from Fig. 9.5;*
† *Data were obtained from Fig. 9.6.*

70 h as listed in Tab. 9.1. The same performance trend was also observed with polarization curves after the break-in process, see Fig. 9.6 and Tab. 9.1. Moreover, the peak power density reached 280 mW cm^{-2}, which was improved by 60 % in relation to the serpentine cell.

It should be noted that the active area is 9.1 cm^2 for the spiral-1.0 and 14.4 cm^2 for the serpentine cell. To be aware of the scaling-up topic, it is necessary to compare the specific flow fields with different active areas, additionally. Appendix A4.1 compares two serpentine flow fields with active areas of 16 and 45 cm^2. Fig. A14 shows a few millivolts difference obtained from the cells with different active areas. Therefore, it can be concluded that the significant performance difference between spiral and serpentine flow field, see in Fig. 9.5 and Fig. 9.6, is determined by the flow field design instead of the active area.

9.1.4 Resistances

To distinguish and quantify different kinds of resistances, EIS measurements were carried out with the spiral-1.0 and serpentine cell after 140 h of operation, as shown in Fig. 9.7. Typically, two semi-arcs occur in the Nyquist plot of HT-PEFCs [117; 144], see Fig. 3.6. One semi-arc, from

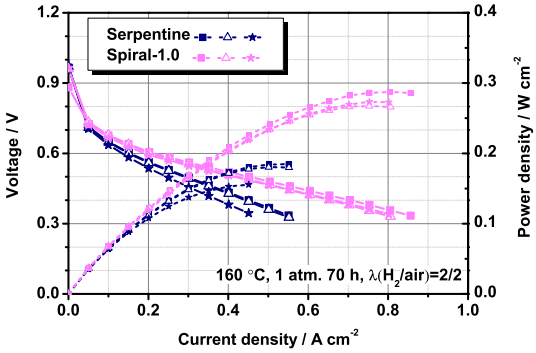

Figure 9.6: Polarization curves of the spiral-1.0 cell and the serpentine cell with $\lambda_{H_2/air}$ = 2/2. The curves were recorded after operation of 70 h at ambient pressure and 160 °C. Each cell type was repeated three times with standard MEAs.

a few kilohertz to a few hertz, is determined by the cathode kinetics and the other, starting from a few hertz, depends on oxygen transport. The diameters of the semi-arcs on the real axis are denoted as kinetic and mass transport resistance, respectively.

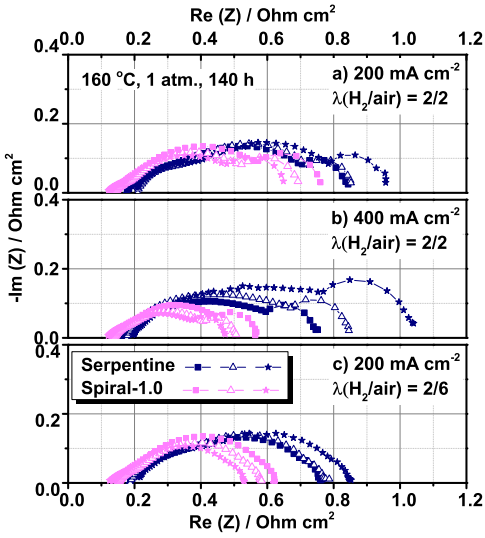

Figure 9.7: Nyquist plots of the spiral-1.0 and the serpentine cells after operation of 140 h; frequency range: 100 mHz – 100 kHz; AC amplitude: 5 mV. Each cell type was repeated three times with standard MEAs.

It is interesting that, two semi-arcs and not just one occur in the frequency range from a few kilohertz to a few hertz for the serpentine cell (see Fig. 9.7). The additional semi-arc appears at 200 mA cm^{-2} even with λ_{air} = 6, but disappears at 400 mA cm^{-2}. Since the leakage of H_2 through the membrane is one order of magnitude lower than that of the methanol in a DMFC, the additional semi-arc could not be caused by the anode fed leakage through the membrane as in

a DMFC [145]. Kulikovsky [134] revealed that the high-frequency semi-arc is associated with the oxygen transport through the electrode. Schneider *et al.* [146] investigated a local impedance of PEFC in the sub-millimeter range. They found pronounced oxygen depletion under the rib and emphasized the important contribution of in-plane diffusion processes to PEFC impedance. The local oxygen distribution is visible as two distinguished semi-arcs in the overall impedance spectra.

In addition to the O_2 transport, the water vapor distribution in the MEA also has a significant effect on the kinetic resistance. Due to the limited gas transport, the water vapor partial pressure is higher in the region under the rib [98]. This leads to a local expansion of phosphoric acid solution. As mentioned in [67], one of the key issues in ORR kinetics is the O_2 transport rate. The transport-limiting step is determined by O_2 diffusion through the electrolyte to the cathode active sites. The expanded acid volume under the rib blocks the pathway of O_2, which hinders the local ORR kinetics.

Therefore, it is reasonable to propose two regions in the electrodes depending on the different oxygen and water content: one under the channel and another one under the rib, as shown in Fig. 2.7. In comparison to the region under the channel, the one under the rib contains less O_2 while high retention of water. This results in two different rates of the kinetic reactions, similar to that predicted in [80] and corresponding to two semi-arcs in the high-frequency range of the Nyquist plot. A modified equivalent circuit was proposed by Dr. Klaus Wippermann, as shown in Fig. 9.8. $R_{ct,ch}$ and $R_{ct,r}$ are kinetic resistances for the region under the channel and rib, respectively. Nyquist plots of the spiral-1.0 cell and the serpentine cell were fitted by the modified equivalent circuit. The values of resistances are plotted in Fig. 9.9.

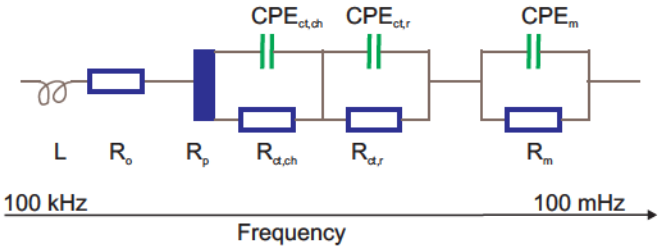

Figure 9.8: Modified equivalent circuit model proposed by Dr. Klaus Wippermann. The model was adapted from Schneider's theory [146] considering the classical transmission line model (Fig. 3.6).

The intercept of the Nyquist curves at high frequency is known as the ohmic resistance [117]. As shown in Fig. 9.7, R_os of the serpentine cell are about 180 m cm^2 at current densities of 200 mA cm^{-2} and 400 mA cm^{-2}, which agreed with the results in [147]. However, the values are 10 – 20 m cm^2 higher than the fitted values in Fig. 9.9 due to the cable inductance.

R_o of the serpentine cell declines by 10 m cm^2 when the current density is increased from 200 mA cm^{-2} to 400 mA cm^{-2}; and R_o rises by 5 m cm^2 when the cathode stoichiometry is increased from 2 to 6. When the cathode flow rate is raised or the current density is reduced, less water will be retained in the MEA. Since an identical content of phosphoric acid was introduced in

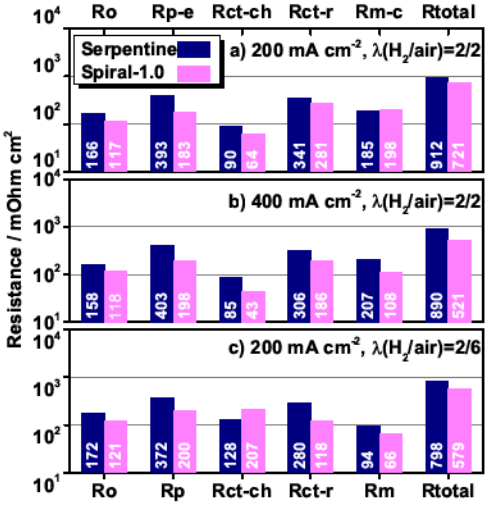

Figure 9.9: Fitted resistance of Nyquist plots in Fig. 9.7 by the equivalent circuit as shown in Fig. 9.8. The values are the mean resistances of three repeat cells assembled with spiral and serpentine flow fields, respectively.

the cells, the reduced water content causes an increase in the acid concentration [66; 136]. The small reduction of R_o (Fig. 9.9) indicates that the acid concentration of the membrane is located at the right-side of the conductivity-composition peak (Fig. 2.5), but close to the plateau. The concentration is in the range of 65 – 70 wt.(P_2O_5)%.

Chapter 8 has revealed that the acid concentration in the cathode is the left-side of the conductivity-composition peak under the same operation conditions and with the identical MEAs. In other words, the acid concentration in the membrane is higher than that in the cathode. This can be explained from two points:

i : the water is produced at the cathode. There is a gradient of water concentration from the active sites to the surrounding.

ii : the acid concentration in the membrane is higher than the surrounding acid solution. The phenomena has been found both in the literature [38] and in this work (Fig. 5.2).

For the spiral-1.0 cells, R_o has no clear variation with the current density and cathode stoichiometries (Fig. 9.9). However, R_o of spiral-1.0 cell is 50 m cm^2 lower than that of the serpentine cell at the same current densities. This means the acid concentration in the membrane of spiral-1.0 cells is lower than the one of the serpentine cells, and at the plateau of the conductivity-composition peak (Fig. 2.5). The reduced acid concentration can be explained as following. Since the dry gases are fed in all cells (Section 3.4.1), the water produced in the serpentine flow field will be transported downstream due to the convective flow along the channel. The water fraction in the gas flow increases along the flow channel from the inlet to the outlet. A CFD[1] simulation shows an

[1] computational fluid dynamics

average water partial pressure over the serpentine flow field of 100 mbar [99]. Correspondingly, there is an opposite gradient of the acid concentration. For the spiral cell, the pressure along the channel was reduced due to the flow crossover between two adjacent channels (Fig. 9.4). In general, the flow pressure declines radially from outside to inside, which leads to an opposite variation of the water fraction [99; 112; 113]. The water concentrates in the center of the spiral flow field. The average water partial pressure over the active area is estimated as 150 mbar by a CFD simulation [99], which is 50 % higher than that of the serpentine cell. The enhanced water partial pressure results in a higher ratio of the water collection at the cathodic outlet and a lower ratio at the anode. The inference is confirmed by the experiments that the water anode ratio of the spiral-1.0 cell is 50 % lower than that of the serpentine cell (Tab. A4). These results indicate a higher water retention over the active area occurred in the spiral-1.0 cell, which reduces the acid concentration in the membrane of spiral-1.0 cells.

As discussed in Chapter 8, the raised water content in the cathode leads to an increase of R_ps. This is the case for the serpentine cell. It can be found in Fig. 9.9 that, R_ps increase by 10 m Ω cm^2 when the current density is raised from 200 mA cm^{-2} to 400 mA cm^{-2}, and decrease by 20 m Ω cm^2 when the cathode stoichiometry increases from 2 to 6. The variation of R_ps confirm again that the acid concentration in the cathode locates in the left-side of the conductivity-composition peak (Fig. 2.5). For the spiral-1.0 cell, R_ps are 50 % lower than the ones of the serpentine cell, while the water vapor partial pressure over the active area is 50 % higher. This indicates that the R_p is dominated by the acid distribution other than the concentration for the spiral-1.0 cell.

The pressure analysis revealed that the appearance of the flow crossover in the spiral-1.0 cell, which forces a gas flow through the porous electrode under the rib by means of convection [80; 86; 93]. It accelerates the oxygen transport into and the water vapor removal from the catalyst layer. The acid concentration becomes more even in sub-millimeter range. The effects benefit the proton conductivity and the kinetics for both regions.

Therefore, $R_{ct,ch}$ and $R_{ct,r}$ of the spiral-1.0 cell were 1.3 times lower than those of the serpentine cell with an exception of $R_{ct,ch}$ at λ_{air} = 6. In addition, with a cathodic stoichiometry of 2, $R_{ct,r}$ was 3.7 times higher than $R_{ct,ch}$ for the serpentine cell, 4.3 times for the spiral-1.0 cell. This is attributed to the local distribution of O_2 in the electrode under the channel and under the rib. $R_{ct,r}$ is reduced by the improved O_2 supple. However, at higher cathode stoichiometry, the faster water removal from the region under the channel increases the acid concentration. It hinders the O_2 transport through the phosphoric acid [69] especially for the spiral-1.0 cell. The ratio of $R_{ct,r}$ and $R_{ct,ch}$ declined to 2.2 and 0.6 at 200 mA cm^{-2} with λ_{air} = 6 for two cells, respectively. The $R_{ct,ch}$ of the spiral-1.0 cell was even 80 m Ω cm^2 higher than that of the serpentine cell. Since $R_{ct,r}$ is the dominant factor, the overall kinetics resistances of the spiral-1.0 cell was still 80 m Ω cm^2 lower than that of the serpentine cell under this operating condition.

For the low-frequency range of the spectra, Fig. 9.7 and Fig. 9.9 show that R_m is almost the same for both cells at 200 mA cm^{-2}. However, at 400 mA cm^{-2}, R_m declines by 90 m Ω cm^2 for the spiral-1.0 cell, but increases by 20 m Ω cm^2 for the serpentine cell. The low-frequency semicircle is related to the oxygen depletion along the channel [134]. The oxygen depletion along the channel is compensated by the flow crossover in the spiral-1.0 cell. The compensation is promoted with

the increase in current density.

In brief, the spiral-1.0 cell presents an obvious flow crossover between two adjacent flow channels. The presence of the flow crossover is benefitial for the local distribution of the gas and acid in the electrode, especially for the region under the rib. This reduces the resistances of the spiral-1.0 cell. There is no clear effect of flow crossover obtained for the serpentine cell. However, in the literature, the significant flow crossover also occurs when using single-channel serpentine flow fields [18; 82]. The conflict comes from the flow field design, *e.g.* the number and length of channels. The same effect also occurs for the spiral designs (comparing Fig. A15 and Fig. A16). Therefore, it is necessary to optimize the flow field, which is also beneficial to understand the effect of the flow crossover on the cell performance.

9.2 Optimization of spiral flow field

In the literature, the flow field geometry for PEFCs can be modified in many different ways to vary the flow crossover. Juarez *et al.* [87] modified the number of the flow channels to optimize the strength of the flow crossover. A 5-channel spiral flow field was investigated by Jang *et al.* [89]. To enhance the flow crossover, the cross-sectional area of the outlet channels was designed smaller than the inlet channel. Cha *et al.* [85] designed a spiral flow field in which inlet and outlet channels are discontinuous to force gas flow transport through the GDL. The authors pointed out that the channel width has complicated effects on the performance of PEFC as well. Here, three different spiral designs (Fig. A15) were also compared and evaluated with a pressure test. Fig. A16 shows that flow crossover can be modified by the flow field design. However, the modification are discontinuously. Another parameter of the flow field geometry is the channel depth, which can be varied continuously. This is hte easiest way of modification because the pattern of the flow field keeps unchanged.

In the following, the spiral flow field was optimized by varying the depth of the flow channel from 0.5 mm to 3.0 mm. This is helpful to further investigate the effect of flow crossover on the performance of HT-PEFC.

9.2.1 Pressure difference

The pressure measurements were performed for the spiral cells as shown in Fig. 9.10. There was a clear tendency towards the reduction in the pressure drop and the pressure ratio as the channel depth was raised. In addition, the spiral-3.0 cell presented a 50 % higher pressure ratio than that of the serpentine cell, although the pressure drop is lower. It confirms that the flow crossover through the electrode under the rib is forced mainly by the pressure difference between two adjacent flow channels.

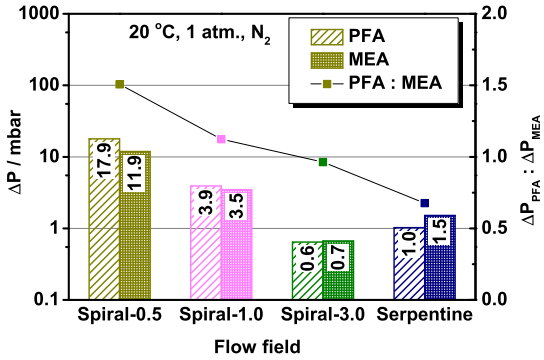

Figure 9.10: Pressure drop between inlet and outlet, and pressure ratio of spiral cells with different depths of flow channel [99, Fig.2]. The data of the serpentine cell (from Fig. 9.4) was taken as reference. The cells were constructed with PFA and the standard MEA, respectively. N_2 is fed at room temperature under atmospheric pressure. The flow rate is calculated with a cathodic stoichiometry of 2 at 200 mA cm^{-2}, e.g. 60 ml min^{-1} for the spiral cells and 100 ml min^{-1} for the serpentine cell.

9.2.2 Cell performance

The voltage of the spiral cells was recorded as a function of the operating time during the break-in process, as shown in Fig. 9.11. The voltage exhibited the following tendency: spiral-1.0 cell $>$ spiral cell-3.0 $>$ serpentine cell $>$ spiral cell-0.5. It becomes clearer when the voltages are plotted against the pressure ratio (Fig. 9.12a). The voltage rises as the pressure ratio increasing up to 1.125, and then droppes sharply. It seems that the spiral-1.0 cell represents the best case.

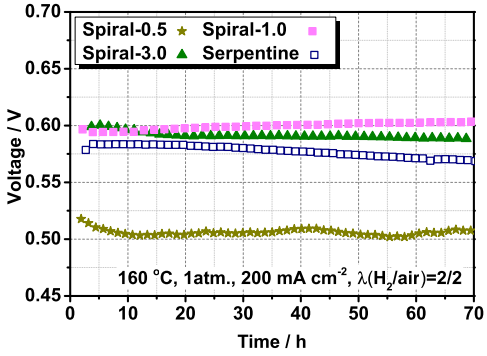

Figure 9.11: Plots of voltage as a function of the operation time for spiral cells with different depths of flow channel [99, Fig.3]. The plots were recorded at 200 mA cm^{-2} with $\lambda_{H_2/air}$ = 2/2, at ambient pressure and 160 °C. The data of the serpentine cell (from Fig. 9.5) were taken as reference.

In addition, the slope in the time range from 50 h to 70 h was also plotted in Fig. 9.12a. It is interesting that the slope increases linearly as a function of the pressure ratio. Kulikovsky [143]

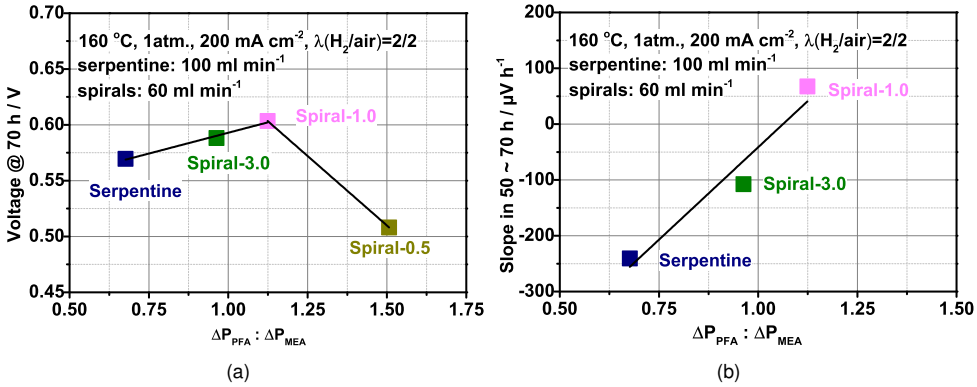

Figure 9.12: Voltage at 70 h and slope in the time range of 50 – 70 h as a function of the pressure ratio. The data were obtained from Fig. 9.11 and Fig. 9.10. Points: experimental data; lines: linear fitting plots.

revealed that the slope of $U \approx t$ curve is influenced by the distribution of current density over the active area. This means the enhanced crossover between adjacent channel benefits a homogeneous distribution of the current density. The comparison between the spiral-3.0 and serpentine cell leads to the conclusion that the improvement of the cell performance is caused by the flow crossover instead of the pressure along the channel. There is a doubt on the spiral-0.5 cell with the voltage as low as 0.5 V, while the slope varied in the whole break-in process. Therefore, the value of the slope is not involved in Fig. 9.12b.

Polarization curves were recorded after the break-in process, and plotted in Fig. 9.13a. The performance presented the same tendency as the voltage obtained in Fig. 9.11. When the cathode stoichiometry was increased up to 6, see in Fig. 9.13b, the polarization curve of the spiral-1.0 cell did not change. The situation was different for the other two spiral cells. A fast increase in the cell voltage was observed. At these very high air stoichiometries, the three spiral cells showed the same performance irrespective of the channel depth, which was better than that of the serpentine cell. This indicates that the differences in spiral cells performance at a low cathode flow rate can be attributed to the variation in gas transport and distribution. Furthermore, the stoichiometric independence of the cell voltage of the spiral-1.0 cell means that this cell design is the most appropriate choice for stable operation with maximum power density.

9.2.3 Resistances

EIS measurements were also carried out with the spiral cells after operation of 140 h. Fig. 9.14a shows the Nyquist plots of the spiral cells with different channel depths. The data of the serpentine cell were taken as reference. The related resistances have been summarized in Fig. 9.14b, which were fitted by the modified equivalent circuit shown in Fig. 9.8. In general, the resistances increase with the channel depth of the spiral cells, with an exception of the spiral-0.5 cell.

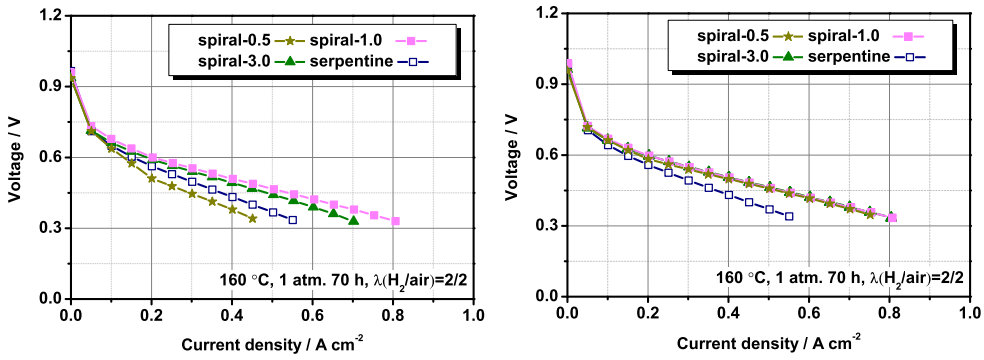

Figure 9.13: Polarization curves of spiral cells with different channel depths [99, Fig.4]. The curves were recorded after operation of 70 h at ambient pressure and 160 °C with (a) $\lambda_{H_2/air}$ = 2/2 and (b) $\lambda_{H_2/air}$ = 2/6. The data of the serpentine cell (Fig. 9.6) were taken as reference.

When the crossover is too weak, due to higher channel depth or flow field geometry such as in the serpentine case, the O_2 undersupply in the electrode becomes worse for the region under the rib. $R_{ct,ch}$, $R_{ct,r}$ and R_m rise simultaneously.

When the crossover is too strong, a “short-cut” will be created like the spiral-0.5 cell. The flow would leak from the inlet to outlet directly resulting in a lack of O_2 at the center of the active area of the spiral flow field. It can be seen from the Nyquist plots of the spiral cell-0.5 that a huge semi-arc occurred in the low-frequency range at λ_{air} = 2 (Fig. 9.14a a, b). R_m, $R_{ct,ch}$ and $R_{ct,r}$ are all significantly higher than that of the other cells (Fig. 9.14b). In addition, the water production gathers at the center of active area. The acid concentration becomes lower [66; 136] and even distributed. As discussed in Section 9.1.4, the acid concentration in the membrane is located at the plateau of composition-conductivity peak, and the one in the cathode at the left-side. The acid dilution leads to a significant increase in R_p. The reduced R_o could be attributed to the homogenous distribution of the acid concentration over the active area.

To sum up, the optimization of the spiral flow field is achieved by modifying the depth of the spiral channels to obtain a suitable flow crossover. It should be noted that the above conclusion is obtained based on the electrode used in the present work. In addition to the flow field geometry, the GDE also has a significant influence on the flow crossover, as shown in Fig. A17. Therefore, the optimized gas distribution is achieved by the interaction of geometric parameters and the structure of GDE beyond the effect of a single parameter. For these reasons, the gas distribution and the water management need to be optimized, not only along the flow channel but also into the electrode, which was achieved by the spiral-1.0 cell.

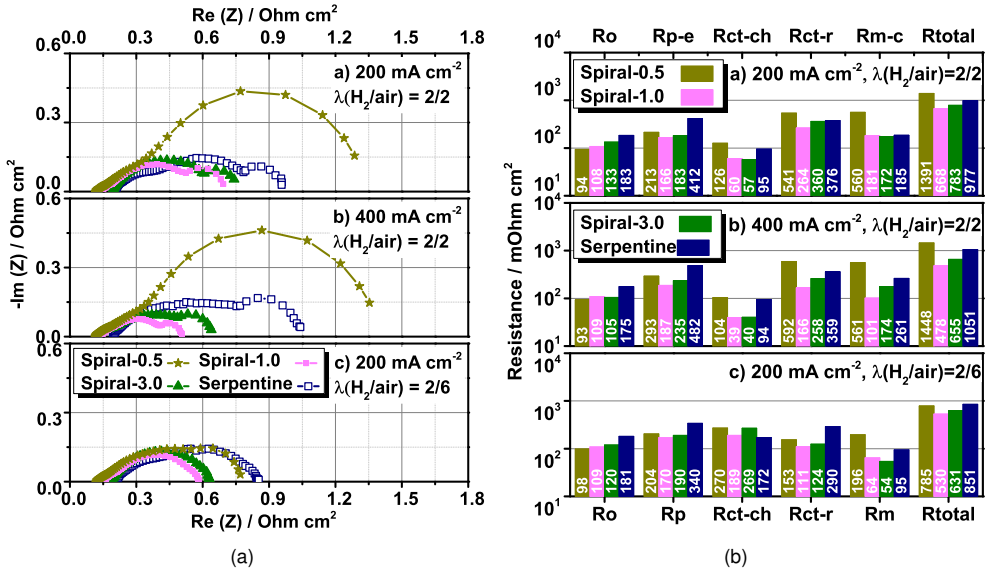

Figure 9.14: (a) Nyquist plots [99, Fig.5] and (b) fitted resistance of spiral cells with different depths of flow channel. The curves were recorded after operation of 140 h; frequency range: 100 mHz – 100 kHz; AC amplitude: 5 mV. The fitted resistances are obtained from the analysis of Nyquist plots in Fig. 9.14a with the equivalent circuit in Fig. 9.8. The data of the serpentine cell were taken as reference.

9.3 Durability of optimized spiral flow field

A durability test up to 1000 h was carried out on a HT-PEFC with the optimized spiral flow field under the constant current and stoichiometry. Fig. 9.15 shows that the degradation rate of the spiral-1.0 cell was estimated at -14 µV h^{-1} in the period of 1000 h, which is a five times lower than that of the serpentine cell. For PBI based HT-PEFC under the constant load, Yu *et al.* [78] reported the degradation rate of 4.9 µV h^{-1} at 200 mA cm^{-2} in 2500 h; 6 µV h^{-1} in 6000 h was published by Schmidt *et al.* [148]. For ABPBI based HT-PEFC, the degradation rate is 25 µV h^{-1} in 1000 h [72]. However, as many of the MEAs and flow field designs found in the literature were not comparable, it is impossible to compare the durability directly.

Büchi and Schmidt [73; 77] revealed that a kinetic degradation starts at the beginning of the operation and causes a slowly, steady and irreversible loss of the cell performance, mainly due to the growth of catalyst grain. In the experiment, the grain size of platinum was characterized by XRD (Section 3.5.2), and the values are listed in Tab. 9.2. The Pt grain size in the initial catalyst powder was obtained as 2.9 nm, consistent with the value stated by the manufacture, which is 2.7 nm. For the dry GDE, the grain size was estimated at 2.5 nm, the same as the value published in [72]. After the operation, the crystallite sizes increase mainly in the period of the first 140 h. The growth of the crystallite is larger for the cathodic catalyst in comparison to the anode, which agrees with [72]. In addition, the grain sizes of the spiral-1.0 cell are even larger than the ones

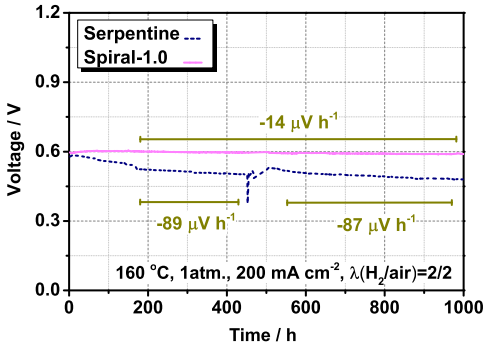

Figure 9.15: Durability test up to 1000 h under constant load for the spiral-1.0 and the serpentine cell [114, Fig.3;100, Fig.4;99, Fig.7]. The plots were recorded at 200 mA cm^{-2} with $\lambda_{H_2/air}$ = 2/2, at ambient pressure and 160 °C.

of the serpentine cell. The increment of the cathodic grain size leads to the reduction of catalyst surface area, 50 % for the serpentine cell and 60 % for the spiral-1.0 cell. However, Fig. 9.15 shows the degradation rate of spiral cell is lower by 74 μV h^{-1} than the serpentine cell. Therefore, the durability of HT-PEFC is not dominated by the growth of catalyst grain. The conclusion differs from [73; 77], because the cathode catalyst in the literature was degraded signicantly due to the carbon corrosion when supplying air at the anode under OCV. The carbon corrosion is caused by the converse voltage due to the presence of H_2/air front in the anode [73; 77]. The effect is minimized in the present work by supplying H_2 for the anode under OCV. Moreover, there is an increase in the Pt crystallite size of the serpentine cell from inlet to outlet, 0.6 nm for 140 h and 1.2 nm for 1000 h, see in Tab. 9.2. This could be associated with the O_2 depletion and the water retention along the flow channel [99; 100]. In contrast, for the spiral geometry (Fig. 9.2), no clear gradient from inlet to outlet can be seen due to the arrangement of flow channels. The homogeneous grain size over the active area might be the reason of the low degradation rate [143] of the spiral-1.0 cell.

Table 9.2: Crystallite size of platinum in catalyst / nm ⊗ 0.1 nm.

Samples	Operation time	Anode			Cathode		
	h	Inlet	Outlet	average	Inlet	Outlet	average
Initial catalyst powder	0			2.9			
Dry GDE	0			2.5			
Serpentine	140	4.0	4.1	4.1	5.1	5.7	5.4
	1000	4.2	4.1	4.2	4.8	6.0	5.4
Spiral-1.0	140	4.1	3.9	4.0	5.9	5.7	5.8
	1000	3.9	4.1	4.0	6.8	6.7	6.8

• *The samples after operation of 140 h and 1000 h were obtained from two standard MEAs for each flow field type.*

In addition, the ECSA of the spiral-1.0 cells and the serpentine cell were obtained by performing cyclic voltammograms after an operation of 140 h and 1000 h, as plotted in Fig. 9.16. The values

of ECSA are summarized in Tab. 9.3. The ECSA decreases by 25 % during the operation from 140 h to 1000 h for the serpentine cell, and 2 % for the spiral-1.0. The Pt utilizations were also calculated by Eqn. A8 based on the crystallite size of the dry GDE and the operated cell. After the long-term test, the utilization was reduced by 25 % for the serpentine cell, while increased by 15 % for the spiral-1.0 cell. Both ECSA and Pt utilization depends on the catalyst surface covered by the acid solution. The variation of ECSA and Pt utilization agrees well with durability of two cells, while opposite to the tendency of the Pt grain growth. It indicates that the contact of catalyst and acid has more dominant effect on the durability in relation to the grain size.

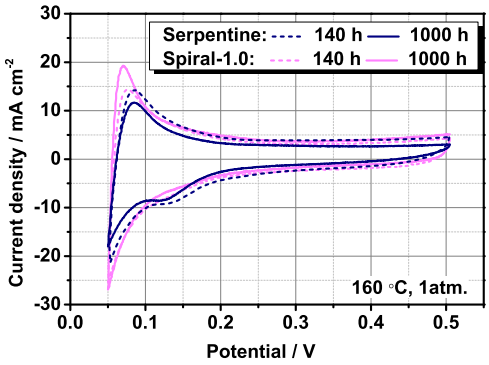

Figure 9.16: Cyclic voltammogram of the spiral-1.0 and the serpentine cell after operation of 140 h [114, Fig.6] and 1000 h, respectively. Anode fed with H_2, and cathode filled with N_2; voltage range: 50 – 505 mV; scan rate: 20 mV s^{-1}.

Table 9.3: ECSA of the spiral-1.0 and the serpentine cells according to curves in Fig. 9.16.

	Operation time	ECSA	Pt utilization I *	Pt utilization II *
	h	$m^2\ g^{-1}$	%	%
Serpentine	140	15.9	14	31
	1000	11.8	11	23
Spiral-1.0	140	18.0	16	37
	1000	17.7	16	43

* *The values of Pt utilization I were calculated based on the crystallite size of dry GDE, 2.5 nm.*
* *The values of Pt utilization II were calculated based on the crystallite size of cathode after operation, as listed in Tab. 9.2.*

Polarization curves were recorded at 1000 h for the spiral-1.0 cell and serpentine cell as shown in Fig. 9.17. The curves recorded at 70 h were plotted as reference. The cell performance of the serpentine cell dramatically degraded, with a voltage loss of 80 mV at 200 mA cm^{-2}. Since no degradation is visible from the polarization curves for the spiral cell after the long-term test, the voltage loss from the plot of voltage *vs*. time might be attributed to the acid distribution in the catalyst layer. Since the acid distribution in the electrode is modified by the varied current density during the recording of the polarization curves, there is no obvious reduction of the voltage obtained for the spiral cell from Fig. 9.17.

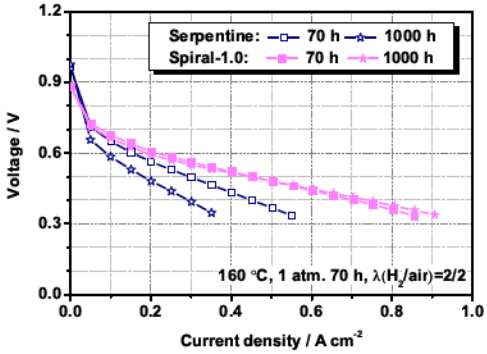

Figure 9.17: Polarization curves of the spiral-1.0 and the serpentine cell after operation of 70 h and 1000 h [114, Fig.2;100, Fig.3;99, Fig.6]. The curves were recorded with $\lambda_{H_2/air}$ = 2/2 at ambient pressure and 160 °C.

The EIS measurements were carried out after operation of 1000 h. The Nyquist plots (Fig. 9.18) were analyzed by equivalent circuit as shown in Fig. 9.8. The fitted results are plotted in Fig. 9.19. As 200 mA cm^{-2}, there is no clear increase in resistances of spiral-1.0 cell and serpentine cell.

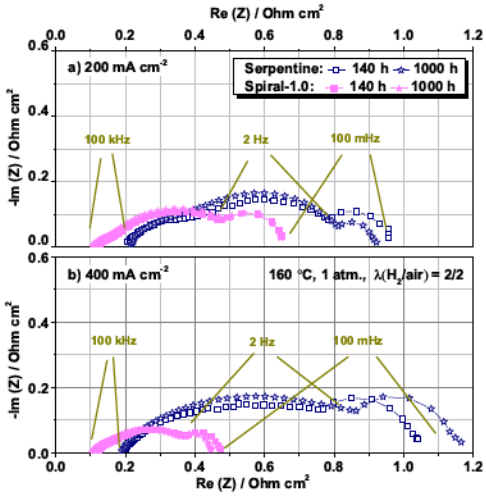

Figure 9.18: Nyquist plots of the spiral-1.0 and the serpentine cell after operation of 140 h and 1000 h [114, Fig.4;100, Fig.5;99, Fig.8]. Frequency range: 100 mHz – 100 kHz; AC amplitude: 5 mV; (a) at 200 mA cm^{-2} and (b) at 400 mA cm^{-2}.

The resistances at 400 mA cm^{-2} of both cells varied in the same tendency. After operation of 1000 h, the stable R_o is consistent with the negligible loss of phosphoric acid during the durability test [72; 73]. R_p rose by 500 m cm^2 for the serpentine cell and 130 m cm^2 for the spiral cell. This indicates that more water is retained in the cathode, especially for the spiral-1.0 cell. This also leads to 100 % increase of $R_{ct,ch}$ and a 50 % decrease of $R_{ct,r}$ at 400 mA cm^{-2} for both cells. The R_m of the serpentine cells is increased by 40 m cm^2.

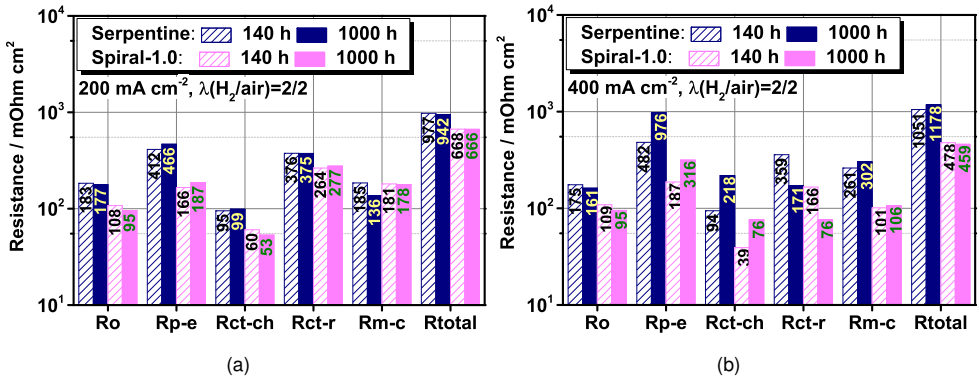

Figure 9.19: Fitted resistances of Nyquist plots in Fig. 9.18 by the equivalent circuit as shown in Fig. 9.8, (a) at 200 mA cm^{-2} and (b) at 400 mA cm^{-2}.

The result indicates that the combination of the acid distribution in the catalyst layer [148] and the catalyst degradation dominates the degradation of HT-PEFC [76; 79] especially at the higher current density. The further determination is expected in means of local characterization. Nevertheless, the durability of the spiral-1.0 cell is associated with the homogeneous distribution of the gas flow [87; 88] and the acid in the cathode.

9.4 Summary

The present chapter investigates the effect of gas distribution on the performance and durability of the HT-PEFC with a customized spiral flow field. Experimental studies indicate that the geometry of the flow field has a great impact on the gas distribution in both in-plane and through-plane directions, along the flow channel and from the flow channel to the electrode. Both oxygen and water vapor distribution are influenced.

With the optimized spiral flow field, the gas transport through the electrode was enhanced under the rib by the force of the pressure difference between two adjacent channels. The flow crossover not only promotes the oxygen supply in the catalyst layer but also compensates the oxygen depletion along the channel. In addition, such a flow distribution also improves the water retention and homogenizes the acid distribution in the MEA. It benefits both the proton conductivity and the cathode kinetics. The degradation of the catalyst starts at the beginning of the operation. During the long-term test, the acid distribution in the catalyst layer has a more dominant effect on the degradation of HT-PEFC.

10 Discussion

10.1 Interaction of phosphoric acid with ABPBI membrane

The proton conductivity of the present HT-PEFC is provided by the ABPBI membrane adsorbed with phosphoric acid. The interaction between ABPBI membrane and phosphoric acid was investigated with the *ex-situ* and *in-situ* experiments.

In the ex-situ experiments (Chapter 4 and Chapter 5), it was found that the content of the phosphoric acid in the ABPBI membrane increases with temperature and concentration of the surrounding acid solution. The complexes of ABPBI-H_3PO_4 can be categorized into two types depending on their affinity. At room temperature the one with lower affinity contributes more to the proton conductivity than the ones with high affinity. In addition, the acid concentration inside the membrane was found to be higher than the surrounding solution especially for the diluted acid solution. The same effect also occurs in the *in-situ* measurements. For an operated HT-PEFC, the acid concentration in the membrane will be higher than that in the electrode.

When the cells were operated under currentless condition, the acid concentration (c_{PA}) in the membrane was estimated as 70 wt.(P_2O_5)% (Tab. 10.1). The proton conductivity (σ_{PA}) decreased significantly with increasing acid concentration. When the cells were operated under constant load, the water product caused a hydration of the phosphoric acid. The acid concentration of the membrane was calculated as 60 – 68 wt.(P_2O_5)% (Tab. 10.1) which is located at the plateau of proton conductivity against acid composition plot. The proton conductivity of the membrane maintained stable within a small variation of the acid concentration.

Table 10.1: Acid concentration and the proton conductivity in the MEA (Chapter 8 and Chapter 9).

	Acid in membrane	Acid in cathode
OCV	$\sim c_{PA} > 70$ wt.(P_2O_5)%, $c_{PA} \downarrow \Rightarrow \sigma_{PA}$	
with current	$\sim c_{PA} = 60 - 68$ wt.(P_2O_5)% $\sim \sigma_{PA}$ independent of c_{PA}	$\sim c_{PA} < 60$ wt.(P_2O_5)% $\sim c_{PA} \downarrow \Rightarrow \sigma_{PA} \downarrow$

10.2 Interaction of phosphoric acid with cathode

In the assembled MEA, the content of phosphoric acid in the membrane ranged up to around 60 wt.-% of total acid uptake in the MEA (Chapter 8). The rest of acid was absorbed by the catalyst layer of the anode and the cathode. This estimation assumes that the MPL acts as boundary of phosphoric acid. All phosphoric acid remains between the MPLs.

The acid solution is preferably transported into the macro-cracks of the catalyst layer compared to the micro-pores of the catalyst layer due to the hydrophobic nature of the material. In the case of low phosphoric acid content in the MEA, mainly the cracks in the electrodes will be filled with acid. When a high level of acid is present, micro- and meso-pores will be filled in addition to the cracks. Only in the case of very thin electrodes no cracks are present in the electrode layer. A contact between the catalyst and phosphoric acid is necessary to form a three-phase boundary where the electrochemical reaction occurs. Both liquid and solid phases need to be part of a percolating network between membrane and electronic conducting bipolar plate, respectively.

In addition to the acid distribution, the proton conductivity of the cathode was also determined by the concentration of phosphoric acid. The acid concentration was decreased by the higher water retention in the cathode. If the water vapor partial pressure in the gas channels was given, the acid concentrations at the electrochemical active site were obtained based on a simple diffusion model. As listed in Tab. 10.1, the acid concentration of the cathode was located at the right side of proton conductivity against acid composition plot under OCV, and at the left side at 200 mA cm^{-2}. As long as the acid concentration was decreased, the proton conductivity increased under the currentless operation and decreased under constant load.

10.3 Interaction of phosphoric acid with gases

The acid distribution in the cathode also influenced the gas distribution. The water removal involves the evaporation and vapor diffusion processes. The rate-limiting step is varied by the distribution of acid and gas in the cathode. The water retention in the MEA influenced the concentration (c_{PA}) and proton conductivity (σ_{PA}) of phosphoric acid, which has been listed in Tab. 10.1. The decreased acid concentration improved the O_2 transport through the acid solution.

In addition, the gas distribution over the active area of MEA is dominated by the flow field geometry. In Chapter 9, a flow crossover between two adjacent channels was obtained with the spiral flow field. The strength of the flow crossover can be modified by the flow channel depth. In addition, the gas permeability of GDE is determined by the MPL. The optimized gas distribution is achieved by the interaction between geometric parameters of flow field and the structure of GDE beyond the effect of a single parameter. With an optimized gas distribution, the O_2 supply was improved not only along the flow channel but also in the GDE in through-plane and in-plane directions.

All these effects significantly enhanced the performance and durability of HT-PEFC. The improved durability was attributed to the acid distribution in the catalyst layer rather than to the degradation of the catalyst.

11 Conclusion

The present work investigated the components in HT-PEFCs including ABPBI membrane, phosphoric acid, catalyst layer, the MPL in the GDE, as well as flow field designs. The effects of each single factor and their interactions on the performance of the HT-PEFC were evaluated. The interactions of different components were connected via the acid and gas distribution. According to the experimental results and previous discussions, the following conclusions are observed:

I : The process of doping ABPBI membrane in phosphoric acid is promoted by the temperature and acid concentration, for both doping level and reaction rate. At room temperature, two types of coordinating sites were identified depending on the affinity of the reaction bond. The complexes of ABPBI-H_3PO_4 with lower affinity contributed more in proton conductivity. The introduction of phosphoric acid into the MEA was chosen as the process of doping ABPBI in the bath of the concentrated phosphoric acid at 160 °C for 15 h. During the cell operation, the content of phosphoric acid in the membrane differs around 60 % of the total acid uptake in the MEA.

II : The acid distribution in the assembled catalyst layer is associated with the content and concentration of phosphoric acid. The acid content in the catalyst layer is modified by the total acid uptake, the presence of MPL, the thickness and porous structure of the catalyst layer. The acid concentration is another critical issue, which varies with the water retention in the MEA. Depending on the operation condition and the water transport, the acid concentration varied in a wide range and differs in the membrane and in the cathode. This affected the proton conductivity and ORR kinetics significantly. The optimum performance of HT-PEFC was obtained with the highest level of the acid uptake, the highest catalyst loading and the thickness of the cathode, a medium level of the anodic catalyst layer thickness, with the presence of MPL at the both sides.

III : The water retention in the MEA was reduced by the expanded area of gas-liquid interface and the promoted gas flow. The promoted gas flow can be obtained by the absence of MPL or an optimized spiral flow field with a channel depth of 1.0 mm. The optimized spiral flow field served a suitable flow crossover between two adjacent channels. It compensated the oxygen depletion along the flow channel and improved the local distribution of oxygen and water vapor in the GDE, both in through-plane and in-plane direction. The performance of the optimized spiral cells with the standard MEA was estimated as 599 mV at 200 mA cm^{-2}, with a degradation rate of -14 µV h^{-1}.

Appendix

A1 Concentration and density of phosphoric acid

Table A1: Concentration and density of phosphoric acid at 25 °C.

		1	2	3	4	5	6	7
Concentration	mol L^{-1}	0	0.1	1	5	10	12	14.8
	wt.-%	0	1.0	9.5	39.7	66.5	74.75	85.0
Acid density [136; 149]	g cm^{-3}	0	1.00	1.05	1.25	1.49	1.57	1.69

A2 Doped membrane

A2.1 Membrane dimension and doping level

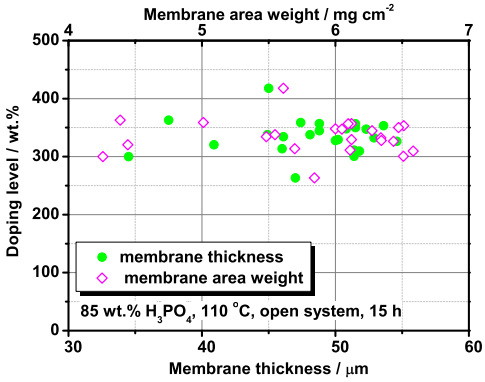

Figure A1: Dependence of acid doping level on the appearance of initial ABPBI membranes. The ABPBI samples were doped in 85 wt.-% phosphoric acid bath at 115 °C for 15 h.

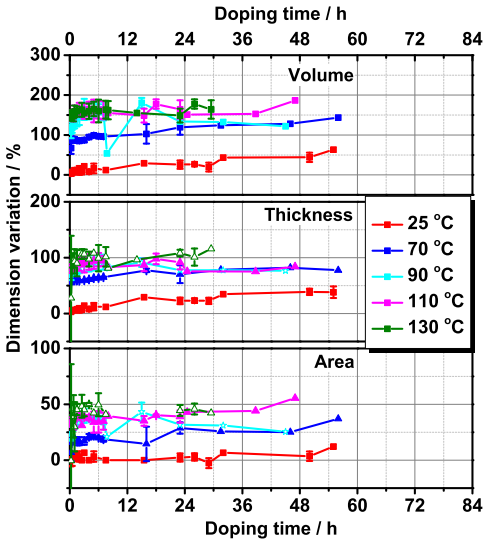

Figure A2: Dimension variations of the ABPBI samples as functions of the doping time. The error bars are standard deviations in absolute. The samples are the same as those in Fig. 4.1.

A2.2 Component content in doped membrane

The following is a short introduction of the elemental characterization by combustion elemental analyzer with CHN Modus and ion chromatography (IC).

The combustion elemental analysis [110, pp.355-357] is useful for organic compounds (compounds containing carbon-carbon bonds) and many inorganic samples. The most common type of elemental analysis is for carbon, hydrogen, and nitrogen (CHN modulus). The sample is transferred into a combustion tube and then burned in an atmosphere enriched in oxygen. A carrier gas flow transfers the combustion products, like CO_2, H_2O and NO_x, into a reduction tube for the reduction of NO_x to N_2. Subsequently, the gas mixture is separated in its components via three adsorption columns. N_2 is not adsorbed and is the first component which enters the thermal conductivity detector, while CO_2 and H_2O are adsorbed at specific adsorption columns. CO_2 and H_2O are then sequentially thermally desorbed and detected. The absolute element content is computed from the integrals of the individual measured peaks and the calibration factors.

Ion chromatography (IC) is an analytical method for ionic species [110, pp.159-160]. It uses the property of ions to be differently strongly bound to polar solid adsorbents, depending on species and size. The test solution is passed across the chromatographic column at pressure. Depending on the exchanger, anions, cations or ion pairs can thus be adsorbed. For the elution of the ions different electrolytes are used and the retention times of the individual ions are determined by their affinity for the stationary phase. A suppressor reduces the high background conductivity of the eluent. Ion detection takes place via conductivity, light absorption or amperometry.

The element contents of the doped ABPBI membranes were characterized by different techniques. The results were compared as shown in Fig. A3 and Fig. A4. The repeat unit of ABPBI is considered as Fig. 2.2b.

I : The weight difference of the samples between before and after doping is used to calculate the weight ratio of a) ABPBI and b) phosphoric acid in doped membrane;

II : The content of carbon (C) were characterized by combustion elemental analyzer (CHN modus).

III : The content of phosphate (PO_4^{3-}) were characterized by IC

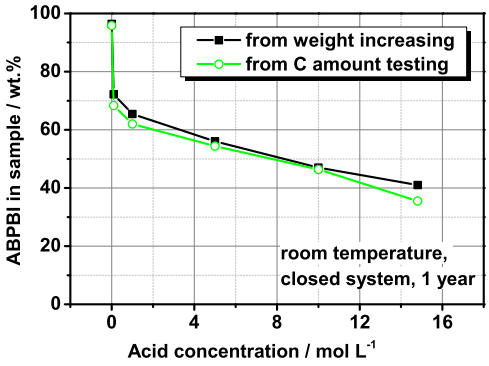

Figure A3: Content of ABPBI in doped membranes characterized by different techniques. The ABPBI samples were the same as that in Fig. 5.1.

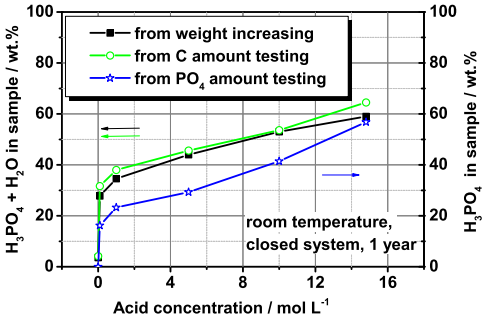

Figure A4: Content of phosphoric acid in doped membranes characterized by different techniques. The ABPBI samples were the same as that in Fig. 5.1.

A2.3 Specific conductivity of doped membrane (ex-situ)

Supposing an isotropic proton conductivity of membranes, the value of the in-plane conductivity would be the same as the through-plane conductivity. The specific conductivity of doped membranes can be calculated by Eqn. A2, and Eqn. A3 for through-plane ohmic resistance.

$$\sigma = \frac{1}{\rho} \tag{A1}$$

$$\sigma = \frac{l}{R_{\parallel} \times d \times w} \tag{A2}$$

$$R_{\perp} = \rho \times d = \frac{d}{\sigma} \tag{A3}$$

σ	S cm^{-1}	specific conductivity
ρ	cm	resistivity
$R_{\parallel}$		in-plane ohmic resistance
$R_{\perp}$	cm^2	through-plane ohmic resistance
l	cm	distance between electrodes, 1 cm here.
w	cm	width of doped membrane
d	cm	thickness of doped membrane

The in-plane proton resistance of doped membranes was examined by means of four-point technique [22]. The doped membranes were threaded between four platinum electrodes as visualized in Fig. A6. The test cell was situated inside a glass container kept in the oven. N_2 was blown constantly with a moderate flow rate through the glass container during the experiment. The water vapor pressure around the membrane was adjusted by varying the dew point of N_2. The temperature and relative humidity in the glass container were measured with a dew point sensor.

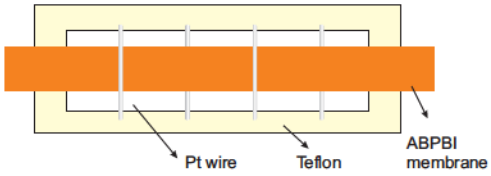

Figure A5: Schematic images of the four-point measurement.

The temperature was raised from room temperature up to 160 °C without the water vapor fed in. The water vapor inside the oven was removed out of with the flow of N_2, which caused an decrease of the water vapor partial pressure. The value decreased sharply first and then slowly. In 30 min the water vapor partial pressure appoached to 20 mbar. In the following, the water vapor was fed with the N_2 flow to increase the water vapor pressure step by step. Each step was held for 30 min. The in-plane resistance was measured for each step.

Fig. A6 and Fig. A7 show the specific conductivities and ohmic resistances (through-plane) of the membrane at 160 °C. The conductivities and resistances were dominated by the acid uptake as well as the water partial pressure around the membrane. There was no direct relationship between the temperature of the acid bath and the conductivity.

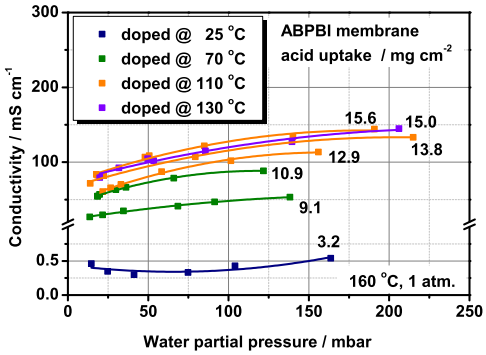

Figure A6: Specific conductivity of doped membranes. The measurements were carried out at 160 °C under 1 atm..

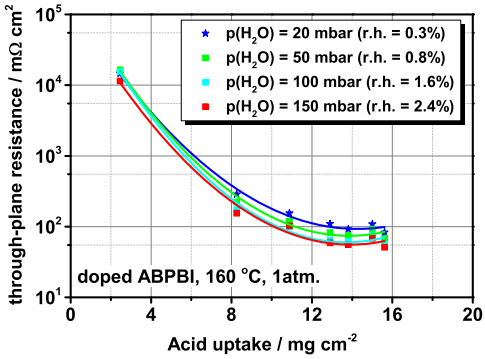

Figure A7: Through-plane resistance of doped membranes. The measurements were carried out at 160 °C under 1 atm..

A3 Catalyst layer

A3.1 Catalyst grain and particle

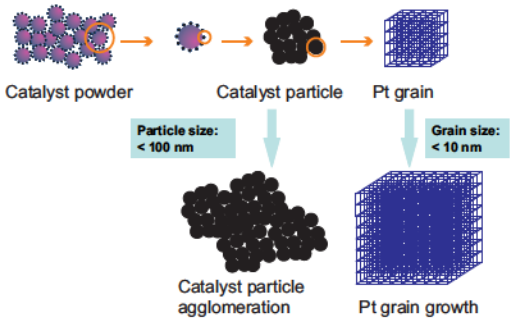

Figure A8: Schematic representation of catalyst powder, particle and grain.

A3.2 Grain size of operated catalyst

Table A2: Crystallite size of platinum in the cathode catalyst after operation.

Cathode catalyst loading	mg cm^{-2}	0.15	0.4	1.0
Grain size after operation	nm	3.1 ⊗ 0.1	4.9 ⊗ 0.1	5.4 ⊗ 0.1

- *The samples were scratched from the HT-PEFC electrodes after operation at 200 mA cm^{-2} and 160 °C for 140 h (Chapter 7).*
- *The grain size of the catalyst in the dry GDE is 2.5 nm ± 0.1 nm.*

A3.3 Specific surface area and utilization of Platinum

To calculate the specific surface area, there are three assumptions: (1) the grain of platinum in the catalyst is supposed as sphere; (2) the density of each grain is supposed as the same as the bulk; (3) the mass of platinum remains constant during operation. The specific surface area of platinum in the catalyst is calculated as Eqn. A7.

$$m = \rho V \tag{A4}$$

$$V = nV_0 = \frac{4}{3}n\pi\left(\frac{d}{2}\right)^3 \tag{A5}$$

$$S = nS_0 = 4n\pi\left(\frac{d}{2}\right)^2 \tag{A6}$$

$$(S/m)_{Pt} = \frac{6}{\rho}\frac{1}{d} \tag{A7}$$

m	g	mass of total grains of Pt
ρ	g cm^{-3}	density of grain of Pt, 21.45 g cm^{-3}
V	cm^3	volume of total grains of Pt
n		amount of grains of Pt
V_0	cm^3	volume of a single grain of Pt
d	cm	mean diameter of Pt grain, 2.7 nm (= 2.7 $\pm$ 10^{-7} cm) was taken, which is suggested by the manufacture
S	cm^2	surface area of total grains of Pt
S_0	cm^2	surface area of a single grain of Pt
$(S/m)_{Pt}$	cm^2 g^{-1}	specific surface area of Pt

Afterwards, the catalyst utilization is obtained with Eqn. A8.

$$\eta = \frac{ECSA}{(S/m)_{Pt}} \pm 100\,\% = \frac{A_{act.}}{(S/m)_{Pt} \times L \times A} \pm 100\,\% \tag{A8}$$

η	%	Pt utilization
$ECSA$	cm^2 g^{-1}	electrochemical surface area
$A_{act.}$	cm^2	active surface area of cathode catalyst
A	cm^2	active area of MEA
L	g cm^{-2}	platinum loading of cathode catalyst

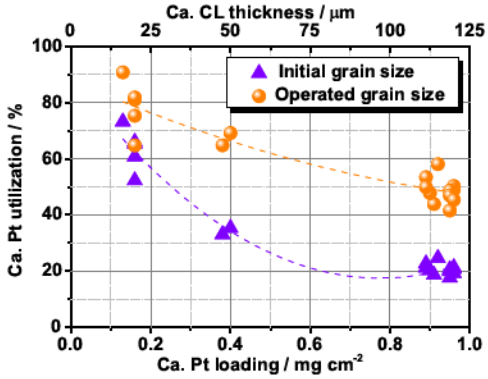

Figure A9: Cathode utilization as a function of cathode loading. The values of cathode active area are the same as the original data in Fig. 8.8. The catalyst utilizations are calculated based on the grain sizes of catalyst as listed in Tab. A2.

A3.4 Intercept of Nyquist curves

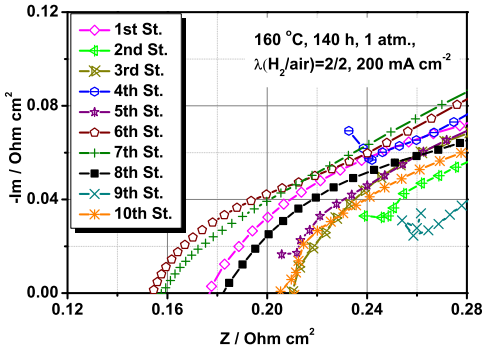

Figure A10: Nyquist curves in the high frequency range for the standard MEAs. The cells were operated at ambient pressure and 160 °C for 140 h, under a current density of 200 mA cm^{-2} and $\lambda_{H_2/air}$ = 2/2. The Nyquist curves were recorded with amplitude of 5 mV in a frequency range of 100 kHz – 100 mHz.

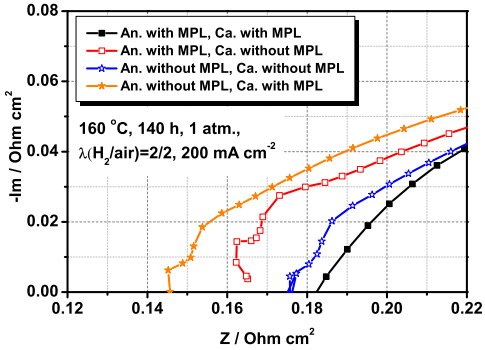

Figure A11: Nyquist curves in the high frequency range for the modified MEAs in Chapter 6. The cell operation and the Nyquist curves recordidng are the same as that in Fig. A10.

A3.5 Anodic catalyst loading and kinetic

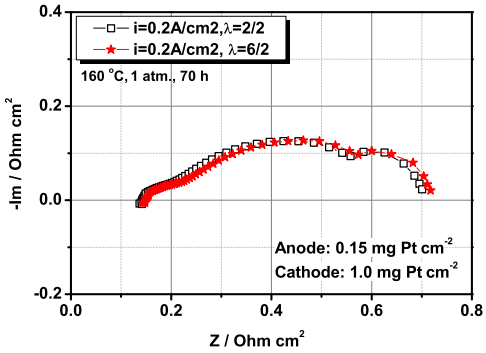

Figure A12: Nyquist plots of the cell operated with different anodic stoichiometries. The anode catalyst loading is 0.15 mg cm^{-2}. The cell was operated at ambient pressure and 160 °C for 140 h, under a current density of 200 mA cm^{-2}. The Nyquist curves were recorded with amplitude of 5 mV in a frequency range of 100 kHz – 100 mHz.

A3.6 Catalyst loading and thickness

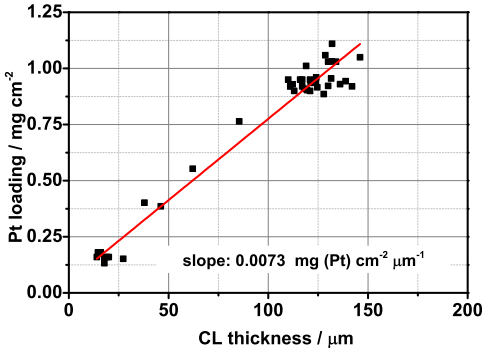

Figure A13: Catalyst loading as a function of the catalyst layer thickness.

A3.7 Details of investigated cells in Chapter 8

Table A3: Catalyst loading and acid uptake of studied cells as designed in Fig. 8.1.

Cell No.	Anode		Cathode		MEA acid uptake
	CL thickness µm	Pt loading mg cm^{-2}	CL thickness µm	Pt loading mg cm^{-2}	mg cm^{-2}
1	16	0.18	16	0.18	11.5
2	132	0.91	132	0.91	11.3
3	132	0.96	132	0.96	18.2
4	118	0.91	19	0.16	11.8
5	19	0.16	118	0.91	11.9
6	122	0.94	121	0.90	18.9
7	117	0.92	19	0.16	18.1
8	14	0.16	117	0.92	18.1
9	14	0.16	14	0.16	18.9
10	124	0.95	124	0.95	15.0
11	57	0.43	132	0.96	15.7
12	15	0.18	128	0.89	17.5
13	128	0.89	38	0.40	15.8
14	128	0.89	18	0.13	16.6
15	60	0.38	60	0.38	16.0
16	18	0.16	18	0.16	16.2
17	128	0.89	18	0.13	16.3
18	20	0.16	117	0.95	14.8
19	20	0.16	117	0.95	15.4
20	118	0.89	118	0.89	16.2
21	124	0.96	124	0.96	15.1

A4 Design of flow field

A4.1 Performance of cells with different active area

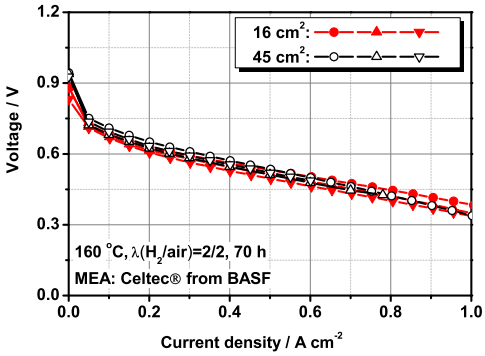

Figure A14: Polarization curves of HT-PEFCs with different active areas. The cells were assembled with serpentine flow fields and a commercial MEA purchased from BASF Fuel Cell GmbH (Frankfurt, Germany). The curves were recorded at ambient pressure and 160 °C with $\lambda_{H_2/air}$ = 2/2.

A4.2 Water anode ratio of spiral cells

Table A4: Water anode ratio (/ %) of the serpentine and the spiral-1.0 cell.

	Serpentine	Spiral-1.0
Sample 1 operated for 140 h	6.0	3.6
Sample 2 operated for 140 h	6.2	1.6
Sample 3 operated for 1000 h	6.6	2.5
Mean	6.3	2.7

- *The cells were the same as described in Chapter 9*
- *The standard MEAs were assembled for all cells, with active area of 9 cm^2 for the spiral-1.0 cell and 14.44 cm^2 for the serpentine cell.*
- *The cells were operated at 200 mA cm^{-2} with $\lambda_{H_2/air}$ = 2/2, at ambient pressure and 160 °C.*

A4.3 Modified flow fields designs

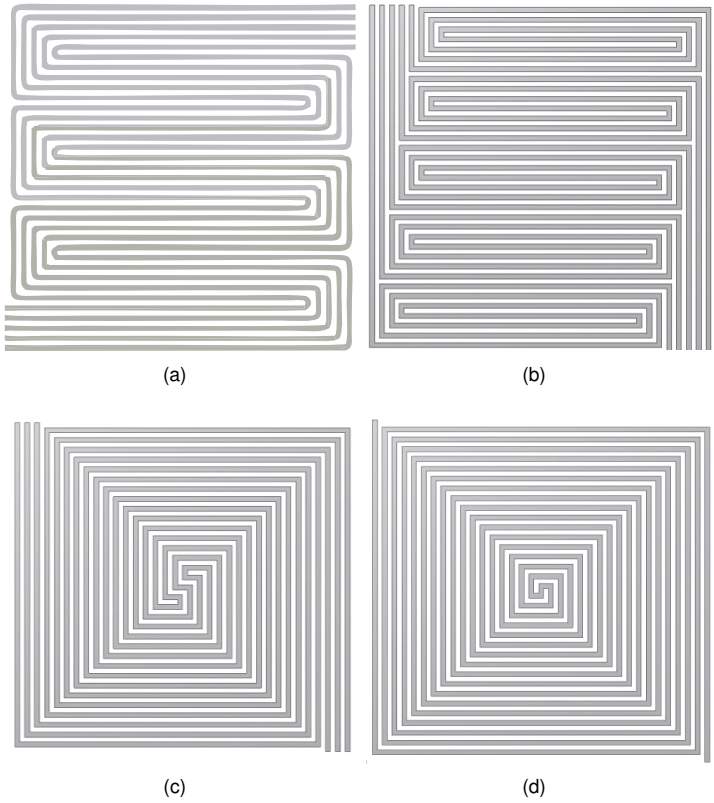

Figure A15: Sketch of flow field design: (a) 5-channel serpentine, (b) 5-cycle spiral, (c) 3-channel spiral and (d) 1-channel spiral. The active areas are all 50 cm^2.

A4.4 Pressure test with different flow field designs and electrode substrates

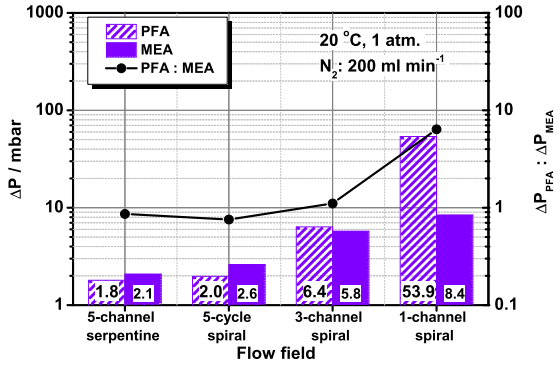

Figure A16: Pressure drop between inlet and outlet of the cells assembled with different flow fields as shown in Fig. A15. The cells were assembled with a commercial MEA purchased from BASF Fuel Cell GmbH (Frankfurt, Germany), with an active area of 45 cm^2. During the test, the cells were fed with N_2 at room temperature under atmospheric pressure

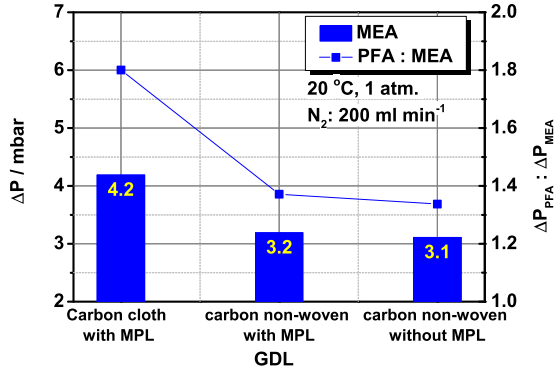

Figure A17: Pressure tests of cells with different GDLs. The cells were assembled with the serpentine flow field, and fed with N_2 at room temperature under atmospheric pressure.

Nomenclature

Abbreviation

ABPBI	poly[2,5-benzimidazole]
CFD	computational fluid dynamics
CV	cyclic voltammetry
DMFC	direct methanol fuel cell
ECSA	electrochemical surface area
EIS	electrochemical impedance spectroscopy
GDE	gas diffusion electrode
GDL	gas diffusion layer
HOR	hydrogen oxidation reaction
HT-PEFC	high-temperature polymer electrolyte fuel cell
IC	ion chromatography
MEA	membrane electrode assembly
MPL	micro-porous layer
OCV	open circuit voltage
ORR	oxygen reduction reaction
PBI	poly[2,2'-(m-phenylene)-2,5'-bibenzimidazole]
PEFC	polymer electrolyte fuel cell
PFA	perfluoroalkoxy
PTFE	polytetrafluoroethylene
XRD	X-ray diffraction

Latin symbols

A	$g\ mol^{-1}$	molar mass of phosphoric acid
A	cm^2	active area of MEA
$A_{act.}$	cm^2 m^2	active surface area of cathode catalyst
c	$mol\ L^{-1}$	constant in Arrhenius equation
C_0	wt.(P_2O_5)% wt.(H_3PO_4)%	concentration of phosphoric acid
Ωc	$mol\ L^{-1}$	concentration difference
CPE_{ct}	Farad cm^{-2}	constant phase element of ORR kinetic
CPE_m	Farad cm^{-2}	constant phase element of mass diffusion
d	cm	thickness of doped membrane

d	nm cm	mean diameter of Pt grain
D	$cm^2\ s^{-1}$	diffusion coefficient
E_a	$kJ\ mol^{-1}$	activation energy
$ECSA$	$cm^2\ g^{-1}$ $m^2\ g^{-1}$	electrochemical surface area
F	$C\ mol^{-1}$	Faraday constant
ΩG_i^0	$kJ\ mol^{-1}$	change of Gibbs free energy
k_1	$wt.\text{-}\%^{-2}\ h^{-1}$	first-order reaction rate constant
j	$mA\ cm^{-2}$	current density
k_1'	h^{-1}	pseudo-first-order rate constant
k_2	$wt.\text{-}\%^{-3}\ h^{-1}$	second-order rate constant
k_2'	$wt.\text{-}\%^{-1}\ h^{-1}$	pseudo-second-order rate constant
k_{id}	$wt.\text{-}\%\ s^{-0.5}$	intraparticle diffusion coefficient
K_i	$L\ mol^{-1}$	thermodynamic equilibrium constant
l	cm	distance between electrodes in four-point measurement
L	$g\ cm^{-2}$ $mg\ cm^{-2}$	platinum loading of cathode catalyst
$[L_i]_F$	$mol\ mol^{-1}$	concentration of free *i*th site
$[L_i]_T$	$mol\ mol^{-1}$	total concentration of *i*th site
$[L_i]_B$	$mol\ mol^{-1}$	concentration of occupied *i*th site
$[L]_{H_3PO_4}$	wt.-%	doping level of H_3PO_4
$[L]_{H_2O}$	wt.-%	doping level of H_2O
m	g	mass
$m_{An.}$	g	mass of water collected at anode outlet
$m_{Ca.}$	g	mass of water collected at cathode outlet
m_{Total}	g	mass of total water collection
M	$g\ mol^{-1}$	molar mass of repeat unit of ABPBI
n		quantity of collected samples
n	mol	number of mole polymer repeat unit in membrane
n		amount of grains of Pt
n	$mol\ s^{-1}cm^{-2}$	number of mole molecules
Ωp	mbar	pressure difference
P	$\mu m\ (Pa\ s)^{-1}$	air permeability of the sample
Q_A	wt.-%	doping level of phosphoric acid of the doped membrane
r	$wt.\text{-}\%\ h^{-1}$	reaction rate
r_{ABPBI}	$ml\ ml^{-1}$	acid volume fraction in ABPBI membrane
$r_{An.}$	$ml\ ml^{-1}$	acid volume fraction in anodic catalyst layer
$r_{Ca.}$	$ml\ ml^{-1}$	acid volume fraction in cathode catalyst layer
R	$kJ\ mol^{-1}\ K^{-1}$	gas constant
R_{ct}	$m\ \ cm^2$	charge transfer resistance
R_m	$m\ \ cm^2$	mass transport resistance
R_o	$m\ \ cm^2$	ohmic resistance
R_p	$m\ \ cm^2$	proton resistance
R_{total}	$m\ \ cm^2$	total resistance
$R_{\parallel}$		in-plane ohmic resistance
$R_{\perp}$	cm^2	through-plane ohmic resistance
$(S/m)_{Pt}$	$cm^2\ g^{-1}$	specific surface area of Pt
S	cm^2	surface area of total Pt grains

t_{Gurley}	(Pa s) µm	Gurley number
t_{mess}	s	recorded time in Gurley experiment
T	K	absolute temperature
V	ml	volume of air used in Gurley experiment
V	cm^3	volume of total Pt grains
w	cm	width of doped membrane in four-point measurement
w	%	water anode ratio
W_{PA}	g	weight of phosphoric acid in doped membrane
W_M	g	weight of membrane before doping
W_{Md}	g	weight of membrane after doping
x	cm	diffusion distance
x_A	mol	number of mole phosphoric acid in doped membrane
x_i		*i*th random sample
$\bar{x}$		average of random sample

Greek symbols

	$\mu C\ cm^{-2}$	charge needed to desorb a monolayer of protons on Pt surface
ε		porosity of GDE
η	%	Pt utilization
$\bar{\theta}_i$		probability of occupation of the *i*th type coordinating site
$\bar{\theta_T}$		total degree of occupation of the coordinating sites
θ_{CL}	µm	thickness of catalyst layer
$\theta_{CL,An.}$	µm	thickness of anode catalyst layer
$\theta_{CL,Ca.}$	µm	thickness of cathode catalyst layer
ρ	$g\ cm^{-3}$	density
ρ	cm	resistivity
σ		standard deviation
σ	$S\ cm^{-1}$	specific conductivity
υ	$mV\ s^{-1}$	scan rate of CV cycle

Bibliography

[1] F. Barbir, *PEM Fuel Cells: Theory and Practice*. Academic Press, 2005. 3, 9, 24, 73, 85

[2] J. Zhang, Y. Tang, C. Song, and J. Zhang, "Polybenzimidazole-membrane-based PEM fuel cell in the temperature range of 120-200 °C," *Journal of Power Sources*, vol. 172, no. 1, pp. 163–171, 2007. 3

[3] J. Zhang, Z. Xie, J. Zhang, Y. Tang, C. Song, T. Navessin, Z. Shi, D. Song, H. Wang, D. Wilkinson, *et al.*, "High temperature PEM fuel cells," *Journal of power sources*, vol. 160, no. 2, pp. 872–891, 2006. 3, 8, 58

[4] I. EG&G Technical Services, "Fuel cell handbook (seventh edition)," tech. rep., 2004. 3, 8

[5] Q. Li, R. He, J. Jensen, and N. Bjerrum, "Approaches and recent development of polymer electrolyte membranes for fuel cells operating above 100 °C," *Chemistry of materials*, vol. 15, no. 26, pp. 4896–4915, 2003. 3

[6] A. Chandan, M. Hattenberger, A. El-kharouf, S. Du, A. Dhir, V. Self, B. G. Pollet, A. Ingram, and W. Bujalski, "High temperature (HT) polymer electrolyte membrane fuel cells (PEMFC) – A review," *Journal of Power Sources*, vol. 231, pp. 264–278, 2013. 3, 8, 11

[7] Y. Shao, G. Yin, Z. Wang, and Y. Gao, "Proton exchange membrane fuel cell from low temperature to high temperature: material challenges," *Journal of Power Sources*, vol. 167, no. 2, pp. 235–242, 2007. 3

[8] M. Mathias, J. Roth, J. Fleming, and W. Lehnert, "Diffusion media materials and characterisation handbook of fuel cells: Fundamentals, technology and applications," in *Fuel Cell Technology and Applications* (W. Vielstich, H. A. Gasteiger, and A. Lamm, eds.), vol. 3, ch. 46, John Wiley & Sons, Ltd, 2003. 3, 8, 20, 55, 60

[9] A. Manso, F. Marzo, J. Barranco, X. Garikano, and M. Garmendia Mujika, "Influence of geometric parameters of the flow fields on the performance of a PEM fuel cell. a review," *International Journal of Hydrogen Energy*, vol. 37, no. 20, pp. 15256–15287, 2012. 4, 12

[10] J. Lobato, P. Cañizares, M. Rodrigo, J. Linares, and F. Pinar, "Study of the influence of the amount of PBI-H_3PO_4 in the catalytic layer of a high temperature PEMFC," *International Journal of Hydrogen Energy*, vol. 35, no. 3, pp. 1347–1355, 2010. 4, 11, 68

[11] Q. Li, H. Hjuler, and N. Bjerrum, "Phosphoric acid doped polybenzimidazole membranes: physiochemical characterization and fuel cell applications," *Journal of applied electrochemistry*, vol. 31, no. 7, pp. 773–779, 2001. 4, 5

[12] A. Ong, G. Jung, C. Wu, and W. Yan, "Single-step fabrication of ABPBI-based GDE and study of its MEA characteristics for high-temperature PEM fuel cells," *International Journal of Hydrogen Energy*, vol. 35, no. 15, pp. 7866–7873, 2010. 4, 12, 91

[13] H. Zheng, L. Petrik, and M. Mathe, "Preparation and characterisation of porous poly (2, 5benzimidazole)(ABPBI) membranes using surfactants as templates for polymer electrolyte membrane fuel cells," *International Journal of Hydrogen Energy*, vol. 35, no. 8, pp. 3745–3750, 2010.

[14] W. Lehnert, K. Wippermann, C. Wannek, D. Stolten, and T. Grube, "Cell resistances of ABPBI-based HT-PEFC-MEAs: Time dependence and influence of operating parameters," in *18th World Hydrogen Energy Conference 2010 - WHEC 2010* (D. Stolten and T. Grube, eds.), vol. 1, pp. 108–114, 2010. 4

[15] F. Conti, A. Majerus, V. Di Noto, C. Korte, W. Lehnert, and D. Stolten, "Raman study of the polybenzimidazole–phosphoric acid interactions in membranes for fuel cells," *Physical Chemistry Chemical Physics*, vol. 14, no. 28, pp. 10022–10026, 2012. 4, 42, 78

[16] Y. Ma, *The fundamental studies of polybenzimidazole/phosphoric acid polymer electrolyte for fuel cells*. PhD thesis, 2004. 42, 45

[17] J. Asensio and P. Gómez-Romero, "Recent developments on proton conduc-ting poly (2, 5-benzimidazole)(ABPBI) membranes for high temperature poly-mer electrolyte membrane fuel cells," *Fuel Cells*, vol. 5, no. 3, pp. 336–343, 2005. 4, 78

[18] K. Kwon, J. Park, D. Yoo, and J. Yi, "Phosphoric acid distribution in the membrane electrode assembly of high temperature proton exchange membrane fuel cells," *Electrochimica Acta*, vol. 54, no. 26, pp. 6570–6575, 2009. 4, 23, 93, 94, 100

[19] C. Wannek, I. Konradi, J. Mergel, and W. Lehnert, "Redistribution of phosphoric acid in membrane electrode assemblies for high-temperature polymer electrolyte fuel cells," *International Journal of Hydrogen Energy*, vol. 34, no. 23, pp. 9479–9485, 2009. 4

[20] K. Kwon, T. Kim, D. Yoo, S. Hong, and J. Park, "Maximization of high-temperature proton exchange membrane fuel cell performance with the optimum distribution of phosphoric acid," *Journal of Power Sources*, vol. 188, no. 2, pp. 463–467, 2009. 4, 9, 11, 68, 75, 85

[21] Y.-H. Cho, S.-K. Kim, T.-H. Kim, Y.-H. Cho, J. W. Lim, N. Jung, W.-S. Yoon, J.-C. Lee, and Y.-E. Sung, "Preparation of MEA with the polybenzimidazole membrane for high temperature PEM fuel cell," *Electrochemical and Solid-State Letters*, vol. 14, no. 3, pp. B38–B40, 2011. 4, 5

[22] C. Wannek, W. Lehnert, and J. Mergel, "Membrane electrode assemblies for high-temperature polymer electrolyte fuel cells based on poly (2, 5-benzimidazole) membranes with phosphoric acid impregnation via the catalyst layers," *Journal of Power Sources*, vol. 192, no. 2, pp. 258–266, 2009. 5, 9, 12, 16, 18, 19, 52, 116

[23] J. Lobato, P. Cañizares, M. Rodrigo, J. Linares, and G. Manjavacas, "Synthesis and characterisation of poly [2, 2-(m-phenylene)-5, 5-bibenzimidazole] as polymer electrolyte membrane for high temperature PEMFCs," *Journal of membrane science*, vol. 280, no. 1-2, pp. 351–362, 2006. 5, 6, 34, 37

[24] O. Edwards and E. Huffman, "Viscosity of aqueous solutions of phosphoric acid at 25 °C," *Industrial & Engineering Chemistry Chemical and Engineering Data Series*, vol. 3, no. 1, pp. 145–146, 1958. 5, 34

[25] P. Atkins and J. De Paula, *Atkins physical chemistry*. 2006. 5, 6, 7, 30, 36, 38, 87

[26] M. H. Kalavathy, T. Karthikeyan, S. Rajgopal, and L. R. Miranda, "Kinetic and isotherm studies of Cu(II) adsorption onto H_3PO_4-activated rubber wood sawdust.," *Journal of colloid and interface science*, vol. 292, no. 2, pp. 354–362, 2005. 5, 33, 35, 39

[27] R. He, Q. Li, J. Jensen, and N. Bjerrum, "Doping phosphoric acid in polybenzimidazole membranes for high temperature proton exchange membrane fuel cells," *Journal of Polymer Science Part A: Polymer Chemistry*, vol. 45, no. 14, pp. 2989–2997, 2007. 5, 6, 7, 16, 17, 31, 41, 42, 43, 44, 45, 46

[28] W. Weber and J. Morris, "Kinetics of adsorption on carbon from solution," *J. Sanit. Eng. Div. Am. Soc. Civ. Eng*, vol. 89, no. 17, pp. 31–60, 1963. 5, 38

[29] M. Sarkar, P. K. Acharya, and B. Bhattacharya, "Modeling the adsorption kinetics of some priority organic pollutants in water from diffusion and activation energy parameters," *Journal of colloid and Interface Science*, vol. 266, no. 1, pp. 28–32, 2003. 5, 38

[30] C. Chakrapani, C. Babu, K. Vani, K. S. Rao, *et al.*, "Adsorption kinetics for the removal of fluoride from aqueous solution by activated carbon adsorbents derived from the peels of selected citrus fruits," *Journal of Chemistry*, vol. 7, no. S1, pp. S419–S427, 2010. 5

[31] Q. Sun and L. Yang, "The adsorption of basic dyes from aqueous solution on modified peat-resin particle," *Water Research*, vol. 37, no. 7, pp. 1535–1544, 2003. 5

[32] J. Wen, X. Han, H. Lin, Y. Zheng, and W. Chu, "A critical study on the adsorption of heterocyclic sulfur and nitrogen compounds by activated carbon: Equilibrium, kinetics and thermodynamics," *Chemical Engineering Journal*, vol. 164, no. 1, pp. 29–36, 2010. 5

[33] F. J. Edeskuty and N. R. Amundson, "Effect of intraparticle diffusion: agitated nonflow adsorption systems," *Industrial & Engineering Chemistry*, vol. 44, no. 7, pp. 1698–1703, 1952. 5

[34] J. Crank, *The mathematics of diffusion*. Oxford university press, 1979. 5

[35] F.-C. Wu, R.-L. Tseng, and R.-S. Juang, "Initial behavior of intraparticle diffusion model used in the description of adsorption kinetics," *Chemical Engineering Journal*, vol. 153, no. 1, pp. 1–8, 2009. 5

[36] S. Allen, G. McKay, and K. Khader, "Intraparticle diffusion of a basic dye during adsorption onto sphagnum peat," *Environmental Pollution*, vol. 56, no. 1, pp. 39–50, 1989. 5

[37] K. K. Choy, J. F. Porter, and G. Mckay, "Intraparticle diffusion in single and multicomponent acid dye adsorption from wastewater onto carbon," *Chemical Engineering Journal*, vol. 103, no. 1, pp. 133–145, 2004. 5

[38] Q. Li, R. He, R. W. Berg, H. A. Hjuler, and N. J. Bjerrum, "Water uptake and acid doping of polybenzimidazoles as electrolyte membranes for fuel cells," *Solid State Ionics*, vol. 168, no. 1, pp. 177–185, 2004. 6, 17, 37, 42, 44, 47, 98

[39] L. Diaz, G. Abuin, and H. Corti, "Water and phosphoric acid uptake of poly [2, 5-benzimidazole](ABPBI) membranes prepared by low and high temperature casting," *Journal of Power Sources*, vol. 188, no. 1, pp. 45–50, 2009. 6, 32

[40] S. Brunauer, L. S. Deming, W. E. Deming, and E. Teller, "On a theory of the van der waals adsorption of gases," *Journal of the American Chemical Society*, vol. 62, no. 7, pp. 1723–1732, 1940. 6, 7

[41] H. E. Rosenthal, "A graphic method for the determination and presentation of binding parameters in a complex system," *Analytical biochemistry*, vol. 20, no. 3, pp. 525–532, 1967. 6, 41, 43

[42] H. A. Feldman, "Mathematical theory of complex ligand-binding systems at equilibrium: some methods for parameter fitting," *Analytical biochemistry*, vol. 48, no. 2, pp. 317–338, 1972. 6, 41, 43, 48

[43] J. Delforge, S. Pappata, P. Millet, Y. Samson, B. Bendriem, A. Jobert, C. Crouzel, and A. Syrota, "Quantification of benzodiazepine receptors in human brain using PET, [^{11}C] flumazenil, and a single-experiment protocol," *Journal of Cerebral Blood Flow & Metabolism*, vol. 15, no. 2, pp. 284–300, 1995. 6

[44] D. Ž. Popović, J. Miladinović, Z. P. Miladinović, S. R. Grujić, M. D. Todorović, and J. A. Rard, "Isopiestic determination of the osmotic and activity coefficients of the yKBr + (1-y) K_2HPO_4 (aq) system at K = 298.15 K," *The Journal of Chemical Thermodynamics*, vol. 62, no. 2, pp. 151–161, 2013. 6

[45] J. Lobato, P. Cañizares, M. A. Rodrigo, D. Ubeda, F. J. Pinar, and J. J. Linares, "Optimisation of the microporous layer for a polybenzimidazole-based high temperature PEMFC – effect of carbon content," *Fuel Cells*, vol. 10, no. 5, pp. 770–777, 2010. 8, 53, 87

[46] J. Lobato, M. Rodrigo, J. Linares, and K. Scott, "Effect of the catalytic ink preparation method on the performance of high temperature polymer electrolyte membrane fuel cells," *Journal of power sources*, vol. 157, no. 1, pp. 284–292, 2006. 8, 23, 75

[47] J. Lobato, P. Cañizares, M. Rodrigo, J. Linares, D. Ubeda, and F. Pinar, "Study of the catalytic layer in polybenzimidazole-based high temperature PEMFC: Effect of platinum content on the carbon support," *Fuel Cells*, vol. 10, no. 2, pp. 312–319, 2010. 8, 9, 12, 82

[48] G. Velayutham, J. Kaushik, N. Rajalakshmi, and K. Dhathathreyan, "Effect of PTFE content in gas diffusion media and microlayer on the performance of PEMFC tested under ambient pressure," *Fuel cells*, vol. 7, no. 4, pp. 314–318, 2007. 8

[49] S. Zils, M. Timpel, T. Arlt, A. Wolz, I. Manke, and C. Roth, "3D visualisation of PEMFC electrode structures using FIB nanotomography," *Fuel Cells*, vol. 10, no. 6, pp. 966–972, 2010.

[50] P. Stuckey, J. Lin, A. Kannan, and M. Ghasemi-Nejhad, "Gas diffusion layers for proton exchange membrane fuel cells using in situ modified carbon papers with multi-walled carbon nanotubes nanoforest," *Fuel Cells*, vol. 10, no. 3, pp. 369–374, 2010.

[51] R. Schweiss, M. Steeb, and P. M. Wilde, "Mitigation of water management in PEM fuel cell cathodes by hydrophilic wicking microporous layers," *Fuel Cells*, vol. 10, no. 6, pp. 1176–1180, 2010. 8

[52] Z. Shao, W. Lin, F. Zhu, P. Christensen, and H. Zhang, "Tubular cathode prepared by a dip-coating method for low temperature DMFC," *Fuel Cells*, vol. 6, no. 5, pp. 326–330, 2006. 8

[53] T. Wang, C. Lin, Y. Fang, F. Ye, R. Miao, and X. Wang, "A study on the dissymmetrical microporous layer structure of a direct methanol fuel cell," *Electrochimica Acta*, vol. 54, no. 2, pp. 781–785, 2008. 8

[54] C. Pan, Q. Li, J. Jensen, R. He, L. Cleemann, M. Nilsson, N. Bjerrum, and Q. Zeng, "Preparation and operation of gas diffusion electrodes for high-temperature proton exchange membrane fuel cells," *Journal of Power Sources*, vol. 172, no. 1, pp. 278–286, 2007. 8, 12, 87

[55] O. Kongstein, T. Berning, B. Borresen, F. Seland, and R. Tunold, "Polymer electrolyte fuel cells based on phosphoric acid doped polybenzimidazole (PBI) membranes," *Energy*, vol. 32, no. 4, pp. 418–422, 2007. 8

[56] J. Lobato, P. Cañizares, M. Rodrigo, C. Ruiz-López, and J. Linares, "Influence of the teflon loading in the gas diffusion layer of PBI-based PEM fuel cells," *Journal of Applied Electrochemistry*, vol. 38, no. 6, pp. 793–802,

2008. 8

[57] T. Kitahara, T. Konomi, and H. Nakajima, "Microporous layer coated gas diffusion layers for enhanced performance of polymer electrolyte fuel cells," *Journal of Power Sources*, vol. 195, no. 8, pp. 2202–2211, 2010. 8

[58] J. Lobato, P. Cañizares, M. A. Rodrigo, and J. J. Linares, *Heat and Mass Transfer: Modeling and Simulation*. InTech, 2011. 8, 53, 55, 57, 60, 64

[59] F. Hizir, S. Ural, E. Kumbur, and M. Mench, "Characterization of interfacial morphology in polymer electrolyte fuel cells: Micro-porous layer and catalyst layer surfaces," *Journal of Power Sources*, vol. 195, no. 11, pp. 3463–3471, 2010. 8, 9, 52, 53

[60] J. Zhang, *PEM Fuel Cell Electrocatalysts and Catalyst Layers: Fundamentals and Applications*. Springer Verlag, 2008. 9, 23, 24, 68, 73, 80, 82

[61] C. Chen and W. Lai, "Effects of temperature and humidity on the cell performance and resistance of a phosphoric acid doped polybenzimidazole fuel cell," *Journal of Power Sources*, vol. 195, no. 21, pp. 7152–7159, 2010. 9, 11, 12, 58, 68, 91

[62] C. G. Zoski, *Handbook of electrochemistry*. Elsevier Science, 2007. 9

[63] T. Suzuki, H. Murata, T. Hatanaka, and Y. Morimoto, "Analysis of the catalyst layer of polymer electrolyte fuel cells," Tech. Rep. 3, 2004. 9

[64] R. P. Ramasamy, E. C. Kumbur, M. M. Mench, W. Liu, D. Moore, and M. Murthy, "Investigation of macro-and micro-porous layer interaction in polymer electrolyte fuel cells," *International Journal of Hydrogen Energy*, vol. 33, no. 13, pp. 3351–3367, 2008. 9, 60, 82

[65] C. Korte, *Fuel Cell Science and Engineering*. Wiley, 2012. 9, 10, 11, 58, 68, 72, 78, 82, 88, 139

[66] D. Chin and H. Chang, "On the conductivity of phosphoric acid electrolyte," *Journal of Applied Electrochemistry*, vol. 19, no. 1, pp. 95–99, 1989. 9, 36, 58, 68, 98, 103

[67] J. Kim, J. Yi, and T. Song, "Investigation of degradation mechanisms of a high-temperature polymer-electrolyte-membrane fuel cell stack by electrochemical impedance spectroscopy," *Journal of Power Sources*, vol. 220, pp. 54–64, 2012. 11, 12, 22, 57, 68, 97

[68] T. Sousa, *Modelling and Simulation of a Laboratory Intermediate Temperature Polymer Electrolyte Fuel Cell*. PhD thesis, 2010. 11, 78

[69] K. Klinedinst, J. Bett, J. Macdonald, and P. Stonehart, "Oxygen solubility and diffusivity in hot concentrated H_3PO_4," *Journal of Electroanalytical Chemistry and Interfacial Electrochemistry*, vol. 57, no. 3, pp. 281–289, 1974. 11, 68, 73, 84, 99

[70] W. Maier, T. Arlt, K. Wippermann, C. Wannek, I. Manke, W. Lehnert, and D. Stolten, "Correlation of synchrotron X-ray radiography and electrochemical impedance spectroscopy for the investigation of HT-PEFCs," *Journal of The Electrochemical Society*, vol. 159, no. 8, pp. F398–F404, 2012. 11, 22, 58, 60, 68, 72, 73, 78, 82, 83, 87, 88

[71] T. Sousa, M. Mamlouk, and K. Scott, "An isothermal model of a laboratory intermediate temperature fuel cell using PBI doped phosphoric acid membranes," *Chemical Engineering Science*, vol. 65, no. 8, pp. 2513–2530, 2010. 11, 68, 88

[72] C. Wannek, B. Kohnen, H.-F. Oetjen, H. Lippert, and J. Mergel, "Durability of ABPBI-based MEAs for high temperature PEMFCs at different operating conditions," *Fuel Cells*, vol. 8, no. 2, pp. 87–95, 2008. 11, 25, 91, 104, 107

[73] F. N. Büchi, M. Inaba, and T. J. Schmidt, eds., *Polymer electrolyte fuel cell durability*. Springer Verlag, 2009. 11, 25, 104, 105, 107

[74] Y. Zhai, H. Zhang, G. Liu, J. Hu, and B. Yi, "Degradation study on MEA in H_3PO_4/PBI high-temperature PEMFC life test," *Journal of the Electrochemical Society*, vol. 154, no. 1, pp. B72–B76, 2007. 11

[75] G. Liu, H. Zhang, J. Hu, Y. Zhai, D. Xu, and Z.-g. Shao, "Studies of performance degradation of a high temperature PEMFC based on H_3PO_4-doped PBI," *Journal of Power Sources*, vol. 162, no. 1, pp. 547–552, 2006. 11

[76] A. Suzuki, Y. Oono, M. C. Williams, R. Miura, K. Inaba, N. Hatakeyama, H. Takaba, M. Hori, and A. Miyamoto, "Evaluation for sintering of electrocatalysts and its effect on voltage drops in high-temperature proton exchange membrane fuel cells (HT-PEMFC)," *International Journal of Hydrogen Energy*, vol. 37, no. 23, pp. 18272 – 18289, 2012. 11, 12, 108

[77] T. J. Schmidt, "Durability and degradation in high-temperature polymer electrolyte fuel cells," *ECS transactions*,

vol. 1, no. 8, pp. 19–31, 2006. 11, 12, 25, 104, 105

[78] S. Yu, L. Xiao, and B. Benicewicz, "Durability studies of PBI-based high temperature PEMFCs," *Fuel Cells*, vol. 8, no. 3-4, pp. 165–174, 2008. 11, 104

[79] J. Lobato, P. Cañizares, M. Rodrigo, and J. Linares, "PBI-based polymer electrolyte membranes fuel cells: Temperature effects on cell performance and catalyst stability," *Electrochimica acta*, vol. 52, no. 12, pp. 3910–3920, 2007. 12, 108

[80] T. Sousa, M. Mamlouk, and K. Scott, "A non-isothermal model of a laboratory intermediate temperature fuel cell using PBI doped phosphoric acid membranes," *Fuel Cells*, vol. 10, no. 6, pp. 993–1012, 2010. 12, 97, 99

[81] T. Sousa, M. Mamlouk, K. Scott, and C. Rangel, "Three dimensional model of a high temperature PEMFC. Study of the flow field effect on performance," *Fuel Cells*, vol. 12, no. 4, pp. 566–576, 2012. 12, 13, 93

[82] R. Taccani and N. Zuliani, "Effect of flow field design on performances of high temperature PEM fuel cells: Experimental analysis," *International Journal of Hydrogen Energy*, vol. 36, no. 16, pp. 10282–10287, 2011. 12, 13, 91, 93, 100

[83] K. Scott, S. Pilditch, and M. Mamlouk, "Modelling and experimental validation of a high temperature polymer electrolyte fuel cell," *Journal of Applied Electrochemistry*, vol. 37, no. 11, pp. 1245–1259, 2007. 12

[84] J. L. Jespersen, E. Schaltz, and S. K. Kær, "Electrochemical characterization of a polybenzimidazole-based high temperature proton exchange membrane unit cell," *Journal of Power Sources*, vol. 191, no. 2, pp. 289–296, 2009. 12

[85] S. Cha, R. O'Hayre, Y. Saito, and F. Prinz, "The scaling behavior of flow patterns: a model investigation," *Journal of power sources*, vol. 134, no. 1, pp. 57–71, 2004. 12, 100

[86] S. Amiruddin, B. Li, and J. Prakash, "A novel flow field design for the effective water transport in polymer electrolyte fuel cells," *ECS Transactions*, vol. 11, no. 1, pp. 703–713, 2007. 12, 91, 99

[87] D. Juarez-Robles, A. Hernandez-Guerrero, B. Ramos-Alvarado, F. Elizalde-Blancas, and C. Damian-Ascencio, "Multiple concentric spirals for the flow field of a proton exchange membrane fuel cell," *Journal of Power Sources*, vol. 196, no. 19, pp. 8019–8030, 2011. 12, 100, 108

[88] V. Rangel-Hernandez, C. Damian-Ascencio, D. Juarez-Robles, A. Gallegos-Muñoz, A. Zaleta-Aguilar, and H. Plascencia-Mora, "Entropy generation analysis of a proton exchange membrane fuel cell (PEMFC) with a fermat spiral as a flow distributor," *Energy*, vol. 36, no. 8, pp. 4864–4870, 2011. 108

[89] J.-Y. Jang, C.-H. Cheng, W.-T. Liao, Y.-X. Huang, and Y.-C. Tsai, "Experimental and numerical study of proton exchange membrane fuel cell with spiral flow channels," *Applied Energy*, vol. 99, pp. 67–79, 2012. 12, 93, 100

[90] J. Yi and T. Van Nguyen, "Multicomponent transport in porous electrodes of proton exchange membrane fuel cells using the interdigitated gas distributors," *Journal of the electrochemical society*, vol. 146, no. 1, pp. 38–45, 1999. 12, 93

[91] A. Kazim, H. Liu, and P. Forges, "Modelling of performance ofPEMfuel cells with conventional and interdigitated flow fields," *Journal of Applied Electrochemistry*, vol. 29, no. 12, pp. 1409–1416, 1999. 12, 93

[92] T. Kanezaki, X. Li, and J. Baschuk, "Cross-leakage flow between adjacent flow channels in PEM fuel cells," *Journal of power sources*, vol. 162, no. 1, pp. 415–425, 2006. 12, 93

[93] Z. Shi and X. Wang, "A numerical study of flow crossover between adjacent flow channels in a proton exchange membrane fuel cell with serpentine flow field," *Journal of power sources*, vol. 185, no. 2, pp. 985–992, 2008. 12, 93, 99

[94] P. K. Sinha, C.-Y. Wang, and U. Beuscher, "Effect of flow field design on the performance of elevated-temperature polymer electrolyte fuel cells," *International journal of energy research*, vol. 31, no. 4, pp. 390–411, 2007. 12, 93

[95] P. Oosthuizen, L. Sun, and K. McAuley, "The effect of channel-to-channel gas crossover on the pressure and temperature distribution in PEM fuel cell flow plates," *Applied Thermal Engineering*, vol. 25, no. 7, pp. 1083–1096, 2005. 12

[96] S. Dutta, S. Shimpalee, and J. Van Zee, "Numerical prediction of mass-exchange between cathode and anode channels in a PEM fuel cell," *International Journal of Heat and Mass Transfer*, vol. 44, no. 11, pp. 2029–2042, 2001. 12

[97] J. Park and X. Li, "An experimental and numerical investigation on the cross flow through gas diffusion layer in a PEM fuel cell with a serpentine flow channel," *Journal of Power Sources*, vol. 163, no. 2, pp. 853–863, 2007. 12

[98] C. Hartnig, I. Manke, R. Kuhn, N. Kardjilov, J. Banhart, and W. Lehnert, "Cross-sectional insight in the water evolution and transport in polymer electrolyte fuel cells," *Applied Physics Letters*, vol. 92, no. 13, pp. 134106–134106, 2008. 12, 60, 97

[99] F. Liu, M. Kvesić, K. Wippermann, U. Reimer, and W. Lehnert, "Effect of spiral flow field design on performance and durability of HT-PEFCs," *Journal of the Electrochemical Society*, vol. 160, no. 8, pp. F892–F897, 2013. 13, 19, 91, 92, 99, 101, 103, 104, 105, 107, 142, 143

[100] F. Liu, M. Kvesić, K. Wippermann, U. Reimer, and W. Lehnert, "Performance and durability of HT-PEFCs with customized flow field," *ECS Transactions*, vol. 50, no. 2, pp. 681–689, 2012. 13, 19, 73, 91, 92, 105, 107, 142, 143

[101] P. K. Janert, *Data analysis with open source tools*. O'Reilly Media, Inc., 2010. 13, 26

[102] M. Kenner, *Skript zur Vorlesung, Einführung in die Statistik*. Universität Stuttgart, Institut für Erziehungswissenschaft und Psychologie, 2006. 13

[103] A. Hense, T. Burkhardt, and P. Friederichs, *Skript zur Vorlesung, Einführung in die Statistik*. Meteorologisches Institut der Universität Bonn, 2005. 13

[104] G. Peichl, *Skript zur Vorlesung, Einführung in die Wahrscheinlichkeitsrechnung und Statistik*. Institut für Mathematik Karl–Franzens–Universität Graz, 1999. 13

[105] W. Kleppmann, *Taschenbuch Versuchsplanung: Produkte und Prozesse optimieren*. Hanser Verlag, 2008. 14

[106] R. Mason, R. Gunst, and J. Hess, *Statistical design and analysis of experiments: with applications to engineering and science*. Wiley-Interscience, 2003. 14

[107] K. Siebertz, D. Van Bebber, and T. Hochkirchen, *Statistische Versuchsplanung: Design of Experiments (DoE)*. Springer, 2010. 14

[108] A. Majerus, F. Conti, C. Korte, W. Lehnert, and D. Stolten, "Thermogravimetric and spectroscopic investigation of the interaction between polybenzimidazole and phosphoric acid," *ECS Transactions*, vol. 50, no. 2, pp. 1155–1165, 2013. 17, 30, 60

[109] R. Jameson, "The composition of the "strong" phosphoric acids," *J. Chem. Soc.*, pp. 752–759, 1959. 17, 32

[110] R. Kellner, J. Mermet, M. Otto, and H. Widmer, "Analytical chemistry. the appoved text to the FECS curriculum analytical chemistry," 2001. 17, 114

[111] W. Maier, T. Arlt, K. Wippermann, C. Wannek, I. Manke, W. Lehnert, and D. Stolten, "Investigation of HT-PEFCs by means of synchrotron X-ray radiography and electrochemical impedance spectroscopy," *ECS Transactions*, vol. 41, no. 1, pp. 1413–1422, 2011. 19, 57, 60

[112] F. Liu, S. Mohajeri, Y. Di, and W. Lehnert, "Effect of catalyst and acid amount on water transport for HT-PEFC," *EFCF 2013 - 4th European PEFC and H_2 Forum*, vol. Chapter 09 - Session A11, pp. 9–17, 2013. 69, 76, 99, 141

[113] F. Liu, S. Mohajeri, Y. Di, K. Wippermann, and W. Lehnert, "Influence of the interaction between phosphoric acid and catalyst layers on the properties of ht-pefcs," *Fuel Cells*, 2014. 19, 69, 71, 72, 73, 74, 75, 99, 141

[114] F. Liu, M. Kvesić, K. Wippermann, U. Reimer, and W. Lehnert, "Performance and durability of HT-PEFCs with customized flow field plates," in *Meeting Abstracts*, no. 13, pp. 1341–1341, The Electrochemical Society, 2012. 19, 91, 92, 105, 106, 107, 142, 143

[115] "International standard iso 5636-5, paper and board - determination of air permeance and air resistance (medium range) - part 5: Gurley method," 20

[116] T. Vismor, *Transmission Line Model*. Timothy Vismor, 2012. 22, 57

[117] K. Wippermann, C. Wannek, H.-F. Oetjen, J. Mergel, and W. Lehnert, "Cell resistances of poly (2, 5-benzimidazole)-based high temperature polymer membrane fuel cell membrane electrode assemblies: Time dependence and influence of operating parameters," *Journal of Power Sources*, vol. 195, no. 9, pp. 2806–2809, 2010. 22, 57, 58, 71, 72, 73, 95, 97

[118] T. A. Osswald and G. Menges, *Materials science of polymers for engineers*. Hanser Verlag, 2003. 30, 36, 38, 39

[119] R. He, Q. Li, A. Bach, J. Jensen, and N. Bjerrum, "Physicochemical properties of phosphoric acid doped polybenzimidazole membranes for fuel cells," *Journal of membrane science*, vol. 277, no. 1-2, pp. 38–45, 2006. 30

[120] R. N. Goldberg, N. Kishore, and R. M. Lennen, "Thermodynamic quantities for the ionization reactions of buffers," *Journal of Physical and Chemical Reference Data*, vol. 31, no. 2, pp. 231–370, 2002. 32, 48

[121] Y. Ho and G. McKay, “Pseudo-second order model for sorption processes,” *Process Biochemistry*, vol. 34, no. 5, pp. 451–465, 1999. 33, 35

[122] V. Lembrikov, V. Volkova, L. Konyakhina, Z. Korneva, and O. Pokidova, “A study of viscosity in the extraction system constituted by tributyl phosphate and phosphoric acid,” *Russian journal of applied chemistry*, vol. 78, no. 8, pp. 1209–1212, 2005. 36

[123] W. P. Ball and P. V. Roberts, “Long-term sorption of halogenated organic chemicals by aquifer material. 2. intraparticle diffusion,” *Environmental Science & Technology*, vol. 25, no. 7, pp. 1237–1249, 1991. 39

[124] V. M. Lobo and J. Quaresma, *Handbook of electrolyte solutions*, vol. 41. Elsevier, 1989. 39

[125] R. N. Goldberg, N. Kishore, and R. M. Lennen, “Thermodynamic quantities for the ionization reactions of buffers,” *Journal of Physical and Chemical Reference Data*, vol. 31, no. 2, pp. 231–370, 2002. 45

[126] S. Mohajeri, “Investigation of asymmetric MEA structure of the HT-PEFC,” Master’s thesis, 2013. 51, 53, 56, 59, 63, 64, 66, 69, 140, 141

[127] W. Maier, T. Arlt, C. Wannek, I. Manke, H. Riesemeier, P. Krüger, J. Scholta, W. Lehnert, J. Banhart, and D. Stolten, “In-situ synchrotron X-ray radiography on high temperature polymer electrolyte fuel cells,” *Electrochemistry Communications*, vol. 12, no. 10, pp. 1436–1438, 2010. 58, 60, 68, 82

[128] J. Nam, K. Lee, G. Hwang, C. Kim, and M. Kaviany, “Microporous layer for water morphology control in PEMFC,” *International Journal of Heat and Mass Transfer*, vol. 52, no. 11-12, pp. 2779–2791, 2009. 60

[129] F. Xie, C. Chen, H. Meng, and P. Shen, “Effect of the anodic diffusion layer on the performance of liquid fuel cells,” *Fuel Cells*, vol. 7, no. 4, pp. 319–322, 2007.

[130] J. Benziger, J. Nehlsen, D. Blackwell, T. Brennan, and J. Itescu, “Water flow in the gas diffusion layer of PEM fuel cells,” *Journal of membrane science*, vol. 261, no. 1-2, pp. 98–106, 2005. 60

[131] C. Tötzke, G. Gaiselmann, M. Osenberg, J. Bohner, T. Arlt, H. Markötter, A. Hilger, F. Wieder, A. Kupsch, B. Müller, M. Hentschel, J. Banhart, V. Schmidt, W. Lehnert, and I. Manke, “Three-dimensional study of compressed gas diffusion layers using synchrotron X-ray imaging.” submitted. 60, 94

[132] R. De Levie, “On porous electrodes in electrolyte solutions - IV,” *Electrochimica Acta*, vol. 9, no. 9, pp. 1231–1245, 1964. 72

[133] T. Springer, T. Zawodzinski, M. Wilson, and S. Gootesfeld, “Diagnostic information from AC impedance measurements on polymer electrolyte fuel cells,” *Electrochemical Society Proceedings*, vol. 23, pp. 137–151, 1995. 73

[134] A. Kulikovsky, “A model for local impedance of the cathode side of PEM fuel cell with segmented electrodes,” *Journal of The Electrochemical Society*, vol. 159, no. 7, pp. F294–F300, 2012. 74, 97, 99

[135] S. Galbiati, A. Baricci, A. Casalegno, and R. Marchesi, “Gas crossover leakage in high temperature polymer electrolyte fuel cells: In situ quantification and effect on performance,” *Journal of Power Sources*, vol. 205, pp. 350–353, 2012. 78

[136] D. MacDonald and J. Boyack, “Density, electrical conductivity, and vapor pressure of concentrated phosphoric acid,” *Journal of Chemical and Engineering Data*, vol. 14, no. 3, pp. 380–384, 1969. 78, 88, 98, 103, 113

[137] A. Majerus, *Eigenschaften des Phosphorsäure-Polybenzimidazol-Systems in Hochtemperatur-Polymerelektrolyt-Brennstoffzellen*. PhD thesis, 2014. 86

[138] E. Földes, E. Fekete, F. Karasz, and B. Pukánszky, “Interaction, miscibility and phase inversion in PBI/PI blends,” *Polymer*, vol. 41, no. 3, pp. 975–983, 2000. 86

[139] S. Chung, S. Bajue, and S. Greenbaum, “Mass transport of phosphoric acid in water: AH and P pulsed gradient spin-echo nuclear magnetic resonance study,” *The Journal of Chemical Physics*, vol. 112, p. 8515, 2000. 86

[140] E. L. Cussler, *Diffusion: mass transfer in fluid systems*. Cambridge university press, 2009. 87

[141] C. Chan, N. Zamel, X. Li, and J. Shen, “Experimental measurement of effective diffusion coefficient of gas diffusion layer/microporous layer in PEM fuel cells,” *Electrochimica Acta*, vol. 65, pp. 13–21, 2012. 87

[142] J. Lobato, P. Cañizares, M. Rodrigo, J. Linares, and J. Aguilar, “Improved polybenzimidazole films for H_3PO_4-doped PBI-based high temperature PEMFC,” *Journal of Membrane Science*, vol. 306, no. 1-2, pp. 47–55, 2007. 91

[143] A. Kulikovsky, H. Scharmann, and K. Wippermann, “Dynamics of fuel cell performance degradation,” *Electrochemistry communications*, vol. 6, no. 1, pp. 75–82, 2004. 94, 101, 105

[144] T. Springer, T. Zawodzinski, M. Wilson, and S. Gottesfeld, “Characterization of polymer electrolyte fuel cells using AC impedance spectroscopy,” *Journal of The Electrochemical Society*, vol. 143, no. 2, pp. 587–599, 1996. 95

[145] A. Kulikovsky, “A model for DMFC cathode impedance: The effect of methanol crossover,” *Electrochemistry Communications*, vol. 24, pp. 65–68, 2012. 97

[146] I. Schneider, M. Bayer, and S. von Dahlen, “Locally resolved electrochemical impedance spectroscopy in channel and land areas of a differential polymer electrolyte fuel cell,” *Journal of The Electrochemical Society*, vol. 158, no. 3, pp. B343–B348, 2011. 97, 142

[147] M. S. Kondratenko, M. O. Gallyamov, and A. R. Khokhlov, “Performance of high temperature fuel cells with different types of PBI membranes as analyzed by impedance spectroscopy,” *International Journal of Hydrogen Energy*, vol. 37, no. 3, pp. 2596–2602, 2012. 97

[148] T. Schmidt and J. Baurmeister, “Properties of high-temperature PEFC Celtec®-P1000 MEAs in start/stop operation mode,” *Journal of Power Sources*, vol. 176, no. 2, pp. 428–434, 2008. 104, 108

[149] J. Christensen and R. Reed, “Design and analysis data — density of aqueous solutions of phosphoric acid measurements at 25 °C.,” *Industrial & Engineering Chemistry*, vol. 47, no. 6, pp. 1277–1280, 1955. 113

List of Figures

List of Tables

Acknowledgments

The four and half year study in Germany is going to be finished. A series of surprise, intention, disappointment and satisfaction happened and repeated all time during my PhD study. When I look back, I appreciate everything I have ever experienced. I would like to take this opportunity to thank and acknowledge everybody who during these three years has helped me to overcome all problems with their friendship, support, and advice.

First of all, I would like to thank my professors, Prof. Werner Lehnert and Prof. Detlef Stolten for the opportunity to work in Forschungszentrum Jülich. Over the last four and half years Prof. Werner Lehnert has been a truly source of inspiration for me, his support, guidance and encouragement were essential to achieve my objectives. I also appreciate the work of the defense committee.

I would like to say thank you to my colleagues in IEK-3. It has been a pleasure working with you. I had a series of successful discussions with Klaus Wippermann, Mirko kvesic, Uwe Reime, Wiebke Maier, Martina Nullmeier and Andrei Kulikovsky. Klaus Wippermann, thanks a lot for all your patience and guidance, without your advice everything would be much harder. In addition, this work was also helped by other colleagues: technical support from Birgit Schumacher, Matthias Prawitz, Jens Bohner and Nils Schneider; experimental work from master students, Sajedeh Mohajeri, Yidu Di and Yuan Yuan.

Anne and Vitali, I will never forget all those hours that we spent together in the same office. There is another important group during my study, twelve-thirty lunch group, which made my lunch breaks a very enjoyable time. Thanks Jen, Jan, Tabea, Qing, Huijie, Li, Tim, Johanes, Klaus, Sohyeon.

In addition, I am grateful to the China Scholarship Council (CSC) who funding my study in Germany. This undoubtedly opened a door for me, and changed my life completely. I also have to thank my home university, Lanzhou University. I got great improvements on my professional and personal ability after nine years study and work. These are the basis to complete my PhD work abroad. Prof. Boxue Feng gave me a lot of encourage and support. Without his help, I might not go to Germany for PhD study.

I appreciate my family to support all my decisions and be always there for me. This work is dedicated to you.

Band / Volume 206
Pulvermetallurgische Funktionsbauteile aus NiTi- und NiTi-X Legierungspulvern
M. Bitzer (2014), III, 144 pp
ISBN: 978-3-89336-937-9

Band / Volume 207
Zinkoxid: Einfluss von Dotierung und Legierungen auf elektro-optische Eigenschaften, auf das Ätzverhalten und auf die Tempernachbehandlung
M. Warzecha (2014), 8, vii, 170 pp
ISBN: 978-3-89336-938-6

Band / Volume 208
SGSreco - Radiologische Charakterisierung von Abfallfässern durch Segmentierte γ-Scan Messungen
T. H. Krings (2014), ix, 181, XI
ISBN: 978-3-89336-945-4

Band / Volume 209
Kühlkonzepte für Hochtemperatur-Polymerelektrolyt-Brennstoffzellen-Stacks
J. Supra (2014), III, 191 pp
ISBN: 978-3-89336-946-1

Band / Volume 210
Eigenschaften des Phosphorsäure-Polybenzimidazol-Systems in Hochtemperatur-Polymerelektrolyt-Brennstoffzellen
A. Majerus (2014), viii, 141 pp
ISBN: 978-3-89336-947-8

Band / Volume 211
Study on the Complex Li-N-H Hydrogen Storage System
L. Du (2014), I, 132 pp
ISBN: 978-3-89336-952-2

Band / Volume 212
Transport and Retention of Stabilized Silver Nanoparticles in Porous Media
Y. Liang (2014), IV, 109 pp
ISBN: 978-3-89336-957-7

Band / Volume 213
Effizienzoptimierte CO_2-Abtrennung in IGCC-Kraftwerken mittels Wassergas-Shift-Membranreaktoren
S. T. Schiebahn (2014), XXII, 203 pp
ISBN: 978-3-89336-958-4

Band / Volume 214
Lebensdauer und Schädigungsentwicklung martensitischer Stähle für Niederdruck-Dampfturbinenschaufeln bei Ermüdungsbeanspruchung im VHCF-Bereich
S. Kovacs (2014), IV, 140 pp
ISBN: 978-3-89336-959-1

Band / Volume 215
Micro- and Macro- Mechanical Testing of Transparent $MgAl_2O_4$ Spinel
O. Tokariev (2014), X, 99 pp
ISBN: 978-3-89336-960-7

Band / Volume 216
Potentiale des Strommanagements zur Reduzierung des spezifischen Energiebedarfs von Pkw
T. Grube (2014), IX, 255 pp
ISBN: 978-3-89336-961-4

Band / Volume 217
Transmutation von Transuranen in einem gasgekühlten beschleunigergetriebenen System
K. H. Biß (2014), IV, 157 pp
ISBN: 978-3-89336-964-5

Band / Volume 218
Untersuchung des photochemischen Terpenoidabbaus in der Atmosphärensimulationskammer SAPHIR
M. Kaminski (2014), 148, VI pp
ISBN: 978-3-89336-967-6

Band / Volume 219
Interaction of Phosphoric Acid with Cell Components in High Temperature Polymer Electrolyte Fuel Cells
F. Liu (2014), i, 147 pp
ISBN: 978-3-89336-972-0

Weitere ***Schriften des Verlags im Forschungszentrum Jülich*** unter
http://wwwzb1.fz-juelich.de/verlagextern1/index.asp

Energie & Umwelt / Energy & Environment
Band / Volume 219
ISBN 978-3-89336-972-0

JÜLICH
FORSCHUNGSZENTRUM